

# STAR FORMATION IN THE MILKY WAY AND NEARBY GALAXIES

ROBERT C. KENNICUTT, JR.

Institute of Astronomy, University of Cambridge, Madingley Road, Cambridge, CB3 0HA, United Kingdom

NEAL J. EVANS II

The University of Texas at Austin, Department of Astronomy, 2515 Speedway, Stop C1400 Austin, TX 78712-1205, USA  
 and

European Southern Observatory, Casilla 19001, Santiago 19, Chile

*To Appear in ARAA, vol. 50*

## ABSTRACT

We review progress over the past decade in observations of large-scale star formation, with a focus on the interface between extragalactic and Galactic studies. Methods of measuring gas contents and star formation rates are discussed, and updated prescriptions for calculating star formation rates are provided. We review relations between star formation and gas on scales ranging from entire galaxies to individual molecular clouds.

*Subject headings:* star formation, galaxies, Milky Way

## 1. OVERVIEW

### 1.1. Introduction

Star formation encompasses the origins of stars and planetary systems, but it is also a principal agent of galaxy formation and evolution, and hence a subject at the roots of astrophysics on its largest scales.

The past decade has witnessed an unprecedented stream of new observational information on star formation on all scales, thanks in no small part to new facilities such as the Galaxy Evolution Explorer (GALEX), the Spitzer Space Telescope, the Herschel Space Observatory, the introduction of powerful new instruments on the Hubble Space Telescope (HST), and a host of ground-based optical, infrared, submillimeter, and radio telescopes. These new observations are providing a detailed reconstruction of the key evolutionary phases and physical processes that lead to the formation of individual stars in interstellar clouds, while at the same time extending the reach of integrated measurements of star formation rates (SFRs) to the most distant galaxies known. The new data have also stimulated a parallel renaissance in theoretical investigation and numerical modelling of the star formation process, on scales ranging from individual protostellar and protoplanetary systems to the scales of molecular clouds and star clusters, entire galaxies and ensembles of galaxies, even to the first objects, which are thought to have reionized the Universe and seeded today's stellar populations and Hubble sequence of galaxies.

This immense expansion of the subject, both in terms of the volume of results and the range of physical scales explored, may help to explain one of its idiosyncracies, namely the relative isolation between the community studying individual star-forming regions and stars in the Milky Way (usually abbreviated hereafter as MW, but sometimes referred to as “the Galaxy”), and the largely extragalactic community that attempts to characterise the star formation process on galactic and cosmologi-

cal scales. Some aspects of this separation have been understandable. The key physical processes that determine how molecular clouds contract and fragment into clumps and cores and finally clusters and individual stars can be probed up close only in the Galaxy, and much of the progress in this subject has come from in-depth case studies of individual star-forming regions. Such detailed observations have been impossible to obtain for even relatively nearby galaxies. Instead the extragalactic branch of the subject has focused on the collective effects of star formation, integrated over entire star-forming regions, or often over entire galaxies. It is this collective conversion of baryons from interstellar gas to stars and the emergent radiation and mechanical energy from the stellar populations that is most relevant to the formation and evolution of galaxies. As a result, much of our empirical knowledge of star formation on these scales consists of scaling laws and other parametric descriptions, in place of a rigorous, physically-based characterization. Improving our knowledge of large-scale star formation and its attendant feedback processes is essential to understanding the birth and evolution of galaxies.

Over the past several years, it has become increasingly clear that many of the key processes influencing star formation on all of these scales lie at the interface between the scales within individual molecular clouds and those of galactic disks. It is now clear that the large scale SFR is determined by a hierarchy of physical processes spanning a vast range of physical scales: the accretion of gas onto disks from satellite objects and the intergalactic medium (Mpc); the cooling of this gas to form a cool neutral phase (kpc); the formation of molecular clouds ( $\sim 10 - 100$  pc); the fragmentation and accretion of this molecular gas to form progressively denser structures such as clumps ( $\sim 1$  pc) and cores ( $\sim 0.1$  pc); and the subsequent contraction of the cores to form stars ( $R_{\odot}$ ) and planets ( $\sim$  AU). The first and last of these processes operate on galactic (or extragalactic) and local cloud scales, respectively, but the others occur at the boundaries between these scales, and the coupling between processes is not yet well understood. Indeed it is possible that different physical pro-

cesses provide the “critical path” to star formation in different interstellar and galactic environments. Whatever the answer to these challenging questions, however, Nature is strongly signalling that we need a unified approach to understanding star formation, one which incorporates observational and astrophysical constraints on star formation efficiencies, mass functions, etc. from small-scale studies along with a much deeper understanding of the processes that trigger and regulate the formation of star-forming clouds on galactic scales, which, in turn, set the boundary conditions for star formation within clouds.

This review makes a modest attempt to present a consolidated view of large-scale star formation, one which incorporates our new understanding of the star formation within clouds and the ensemble properties of star formation in our own MW into our more limited but broader understanding of star formation in external galaxies. As will become clear, the subject itself is growing and transforming rapidly, so our goal is to present a progress report in what remains an exciting but relatively immature field. Nevertheless a number of factors make this a timely occasion for such a review. The advent of powerful multi-wavelength observations has transformed this subject in fundamental ways since the last large observational review of the galaxy-scale aspects (Kennicutt 1998a), hereafter denoted K98. Reviews have covered various observational aspects of star formation within the MW (Evans 1999; Bergin & Tafalla 2007; Zinnecker & Yorke 2007), but the most comprehensive reviews have been theoretically based (Shu et al. 1987; McKee & Ostriker 2007). We will take an observational perspective, with emphasis on the interface between local and galactic scales. We focus on nearby galaxies and the MW, bringing in results from more distant galaxies only as they bear on the issues under discussion.

The remainder of this article is organized as follows. In the next subsection, we list some definitions and conventions that will be used throughout the paper. All observations in this subject rest on quantitative diagnostics of gas properties and star formation rates on various physical scales, and we review the current state of these diagnostics (§2, §3). In §4, we review those properties of Galactic star-forming regions which are most relevant for comparison to other galaxy-wide studies. In §5, we review the star-forming properties of galaxies on the large scale, including the MW; much of this section is effectively an update of the more extended review presented in K98. Section 6 updates our knowledge of relations between star formation and gas (e.g., the Schmidt law) and local tests of these relations. The review concludes in §7 with our attempted synthesis of what has been learned from the confluence of local and global studies and a look ahead to future prospects.

We list in §1.3 some key questions in the field. Some have been or will be addressed by other reviews. Some are best answered by observations of other galaxies; some can only be addressed by observations of local star-forming regions in the MW. For each question we list sections in this review where we review the progress to date in answering them, but many remain largely unanswered and are referred to the last section of this review on future prospects.

Space limitations prevent us from citing even a fair fraction of the important papers in this subject, so we

instead cite useful examples and refer the reader to the richer lists of papers that are cited there.

## 1.2. Definitions and Conventions

Here we define some terms and symbols that will be used throughout the review.

The term “cloud” refers to a structure in the interstellar medium (ISM) separated from its surroundings by the rapid change of some property, such as pressure, surface density, or chemical state. Clouds have complex structure, but theorists have identified two relevant structures: clumps are the birthplaces of clusters; cores are the birthplaces of individual or binary stars (e.g., McKee & Ostriker 2007). The observational equivalents have been discussed (e.g., Table 1 in Bergin & Tafalla 2007), and cores reviewed (di Francesco et al. 2007; Ward-Thompson et al. 2007a), and we discuss them further in §2.2.

We will generally explicitly use “surface density” or “volume density”, but symbols with  $\Sigma$  will refer to surface density,  $N$  will refer to column density, and symbols with  $n$  or  $\rho$  will refer to number or mass volume density, respectively. The surface density of H I gas is represented by  $\Sigma_{\text{HI}}$  if He is not included and by  $\Sigma(\text{atomic})$  if He is included. The surface density of molecular gas is symbolized by  $\Sigma_{\text{H}_2}$ , which generally does not include He, or  $\Sigma_{\text{mol}}$ , which generally does include He. For MW observations, He is almost always included in mass and density estimates, and  $\Sigma_{\text{mol}}$  may be determined by extinction or emission by dust (§2.3) or by observations of CO isotopologues (§2.4). When applied to an individual cloud or clump, we refer to it as  $\Sigma(\text{cloud})$  or  $\Sigma(\text{clump})$ . For extragalactic work,  $\Sigma_{\text{H}_2}$  or  $\Sigma_{\text{mol}}$  are almost always derived from CO observations, and inclusion of He is less universal. In the extragalactic context,  $\Sigma_{\text{mol}}$  is best interpreted as related to a filling factor of molecular clouds until  $\Sigma_{\text{mol}} \sim 100 \text{ M}_\odot \text{ pc}^{-2}$ , where the area filling factor of molecular gas may become unity (§2.4). Above this point, the meaning may change substantially. The total gas surface density, with He, is  $\Sigma_{\text{gas}} = \Sigma_{\text{mol}} + \mu \Sigma_{\text{HI}}$ , where  $\mu$  is the mean molecular weight per H atom;  $\mu = 1.41$  for MW abundances (Kauffmann et al. 2008), though a value of 1.36 is commonly used.

The conversion from CO intensity (usually in the  $J = 1 \rightarrow 0$  rotational transition) to column density of  $\text{H}_2$ , not including He, is denoted  $X(\text{CO})$ , and the conversion from CO luminosity to mass, which usually includes the mass of He, is denoted  $\alpha_{\text{CO}}$ .

The term “dense gas” refers generally to gas above some threshold of surface density, as determined by extinction or dust continuum emission, or of volume density, as indicated by emission from molecular lines that trace densities higher than does CO. While not precisely defined, suggestions include criteria of a threshold surface density, such as  $\Sigma_{\text{mol}} > 125 \text{ M}_\odot \text{ pc}^{-2}$  (Goldsmith et al. 2008; Lada et al. 2010; Heiderman et al. 2010), a volume density criterion (typically  $n > 10^4 \text{ cm}^{-3}$ ) (e.g., Lada 1992), and detection of a line from certain molecules, such as HCN. The surface and volume density criteria roughly agree in nearby clouds (Lada et al. 2012) but may not in other environments.

The star formation rate is symbolized by SFR or  $\dot{M}_*$ , often with units of  $\text{M}_\odot \text{ yr}^{-1}$  or  $\text{M}_\odot \text{ Myr}^{-1}$ , and its

meaning depends on how much averaging over time and space is involved. The surface density of star formation rate,  $\Sigma(\text{SFR})$ , has the same averaging issues. The efficiency of star formation is symbolized by  $\epsilon$  when it means  $\dot{M}_*/(\dot{M}_* + \dot{M}_{\text{cloud}})$ , as it usually does in Galactic studies. For extragalactic studies, one usually means  $\dot{M}_*/\dot{M}_{\text{gas}}$ , which we symbolize by  $\epsilon'$ . The depletion time,  $t_{\text{dep}} = 1/\epsilon'$ . Another time often used is the “dynamical” time,  $t_{\text{dyn}}$ , which can refer to the free-fall time ( $t_{\text{ff}}$ ), the crossing time ( $t_{\text{cross}}$ ), or the galaxy orbital time ( $t_{\text{orb}}$ ). In recent years, it also has become common to compare galaxies in terms of their SFR per unit galaxy mass, or “specific star formation rate” (SSFR). The SSFR scales directly with the stellar birthrate parameter  $b$ , the ratio of the SFR today to the average past SFR over the age of the galaxy, and thus provides a useful means for characterizing the star formation history of a galaxy.

The far-infrared luminosity has a number of definitions, and consistency is important in converting them to  $\dot{M}_*$ . A commonly used definition integrates the dust emission over the wavelength range 3–1100  $\mu\text{m}$  (Dale & Helou 2002), and following those authors we refer to this as the total-infrared or TIR luminosity. Note however that other definitions based on a narrower wavelength band or even single-band infrared measurements are often used in the literature.

We refer to mass functions with the following conventions. Mass functions are often approximated by power laws in  $\log M$ :

$$dN/d\log M \propto M^{-\gamma}, \quad (1)$$

In particular, the initial mass function (IMF) of stars is often expressed by equation 1 with a subscript to indicate stars (e.g.,  $M_*$ ).

Structures in gas are usually characterized by distributions versus mass, rather than logarithmic mass:

$$dN/dM \propto M^{-\alpha}, \quad (2)$$

for which  $\alpha = \gamma + 1$ . Terminology in this area is wildly inconsistent. To add to the confusion, some references use cumulative distributions, which decrease the index in a power law by 1.

The luminosities and masses of galaxies are well represented by an exponentially truncated power-law function (Schechter 1976):

$$\Phi(L) = (\Phi^*/L^*)(L/L^*)^\alpha e^{(-L/L^*)} \quad (3)$$

The parameter  $\alpha$  denotes the slope of the power-law function at low luminosities, and  $L^*$  represents the luminosity above which the number of galaxies declines sharply. For the relatively shallow slopes ( $\alpha$ ) which are typical of present-day galaxies,  $L^*$  also coincides roughly with the peak contribution to the total light of the galaxy population. As discussed in §5.2, the Schechter function also provides a good fit to the distribution function of total SFRs of galaxies, with the characteristic SFR in the exponential designated as  $\text{SFR}^*$ , in analogy to  $L^*$  above.

The term “starburst galaxy” was introduced by Weedman et al. (1981), but nowadays the term is applied to a diverse array of galaxy populations. The common property of the present-day populations of starbursts is a SFR

out of equilibrium, much higher than the long-term average SFR of the system. No universally accepted quantitative definition exists, however. Some of the more commonly applied criteria are SFRs that cannot be sustained for longer than a small fraction (e.g.,  $\leq 10\%$ ) of the Hubble time, i.e., with gas consumption timescales of less than  $\ll 1$  Gyr, or galaxies with disk-averaged SFR surface densities  $\Sigma(\text{SFR}) \geq 0.1 \text{ M}_\odot \text{ yr}^{-1} \text{ kpc}^{-2}$  (§5.2). Throughout this review we will use the term “quiescent star-forming galaxies” merely to characterize the non-starbursting galaxy population. Note that these local criteria for identifying starbursts are not particularly useful for high-redshift galaxies; a young galaxy forming stars at a constant SFR might more resemble a present-day starburst galaxy than a normal galaxy today.

### 1.3. Questions

1. How should we interpret observations of the main molecular diagnostic lines (e.g., CO, HCN) and millimeter-wave dust emission? How does this interpretation change as a function of metallicity, surface density, location within a galaxy, and star formation environment? (§2.4, §5.1, §7.3)
2. How does the structure of the ISM, the structure of star-forming clouds, and the star formation itself change as a function of metallicity, surface density, location within a galaxy, and star formation environment? (§2.4, §5, §7.3).
3. How do the mass spectra of molecular clouds and dense clumps in clouds vary between galaxies and within a galaxy? (§2.5, §5.1, §7.3)
4. How constant is the IMF, and how are star formation rate measurements affected by possible changes in the IMF or by incomplete sampling of the IMF? (§2.5, §3.3, §4.2, §6.4)
5. What are the limits of applicability of current star formation rate tracers? How are current measurements biased by dust attenuation or the absence of dust, and how accurately can the effects of dust be removed? How do different tracers depend on metallicity, and what stellar mass ranges and timescales do they probe? (§3)
6. How long do molecular clouds live and how can we best measure lifetimes? Do these lifetimes change systematically as functions of cloud mass, location in a galaxy, or some other parameter? (§4.3, §7.3)
7. Do local observations provide any evidence for bimodality in modes of star formation, for example distributed versus clustered, low-mass versus high-mass star formation? (§4, §7.3)
8. On the scale of molecular clouds, what are the star formation efficiencies [ $\epsilon = \dot{M}_*/(\dot{M}_* + \dot{M}_{\text{cloud}})$ ], and star formation rates per unit mass ( $\epsilon' = \dot{M}_*/\dot{M}_{\text{cloud}}$ ), and do these efficiencies vary systematically as functions of cloud mass or other parameters? (§4, §7.3)

9. How do spatial sampling and averaging affect the observed form of the star formation relations expressed in terms of total, molecular, or dense gas surface densities? How well do  $\dot{M}_*$  diagnostics used in extragalactic studies work on finer scales within a galaxy? (§3.9, §6, §6.4, §7.3)
10. Are there breakpoints or thresholds where either tracers or star formation change their character? (§2, §3, §7)

## 2. ISM DIAGNOSTICS: GAS AND DUST

### 2.1. *ISM Basics*

The interstellar medium (ISM) is a complex environment encompassing a very wide range of properties (e.g., McKee & Ostriker 1977; Cox 2005). In the Milky Way, about half the volume is filled by a hot ionized medium (HIM) with  $n < 0.01 \text{ cm}^{-3}$  and  $T_K > 10^5 \text{ K}$ , and half is filled by some combination of warm ionized medium (WIM) and warm neutral medium (WNM), with  $n \sim 0.1 - 1 \text{ cm}^{-3}$  and  $T_K$  of several thousand K (Cox 2005). The neutral gas is subject to a thermal instability that predicts segregation into the warm neutral and cold neutral media (CNM), the latter with  $n > 10 \text{ cm}^{-3}$  and  $T_K < 100 \text{ K}$  (Field et al. 1969). The existence of the CNM is clearly revealed by emission in the hyperfine transition of H I, with median temperature about 70 K, determined by comparison of emission to absorption spectra (Heiles & Troland 2003). However, the strict segregation into cold and warm stable phases is not supported by observations suggesting that about 48% of the WNM may lie in the thermally unstable phase (Heiles & Troland 2003). Finally, the molecular clouds represent the coldest ( $T_K \sim 10 \text{ K}$  in the absence of star formation), densest ( $n > 30 \text{ cm}^{-3}$ ) part of the ISM. We focus on the cold ( $T_K < 100 \text{ K}$ ) phases here, as they are the only plausible sites of star formation. The warmer phases provide the raw material for the cold phases, perhaps through “cold” flows from the intergalactic medium (Dekel & Birnboim 2006). In the language of this review, such flows would be “warm.”

In the next section, we introduce some terminology used for the molecular gas as a precursor to the following discussion of the methods for tracing it. We then discuss the use of dust as a tracer (§2.3) before discussing the gas tracers themselves (§2.4).

### 2.2. *Clouds and Their Structures*

The CNM defined in the preceding section presents a wide array of structures, with a rich nomenclature, but we focus here on the objects referred to as clouds, invoking a kind of condensation process. This name is perhaps even more appropriate to the molecular gas, which corresponds to a change in chemical state.

The molecular cloud boundary is usually defined by the detection, above some threshold, of emission from the lower rotational transitions of CO. Alternatively, a certain level of extinction of background stars is often used. In confused regions, velocity coherence can be used to separate clouds at different distances along the line of sight. However, molecular clouds are surrounded by atomic envelopes and a transition region in which the hydrogen is primarily molecular, but the carbon is

mostly atomic (van Dishoeck & Black 1988). These regions are known as PDRs, which stands either for Photo-Dissociation Regions, or Photon-Dominated Regions (Hollenbach & Tielens 1997). More recently, they have been referred to as “dark gas.”

The structure of molecular clouds is complex, leading to considerable nomenclatural chaos. Cloud projected boundaries, defined by either dust or CO emission or extinction, can be characterized by a fractal dimension around 1.5 (Falgarone et al. 1991; Scalo 1990; Stutzki et al. 1998), suggesting an intrinsic 3-D dimension of 2.4. When mapped with sufficient sensitivity and dynamic range, clouds are highly structured, with filaments the dominant morphological theme; denser, rounder cores are often found within the filaments (e.g., André et al. 2010; Men’shchikov et al. 2010; Molinari et al. 2010).

The probability distribution function of surface densities, as mapped by extinction, can be fitted to a log-normal function for low extinctions,  $A_V \leq 2 - 5 \text{ mag}$  (Lombardi et al. 2010), with a power law tail to higher extinctions, at least in some clouds. In fact, it is the clouds with the power-law tails that have active star formation (Kainulainen et al. 2009). Further studies indicate that the power-law tail begins at  $\Sigma_{mol} \sim 40 - 80 \text{ M}_\odot \text{ pc}^{-2}$ , and that the material in the power-law tail lies in unbound clumps with mean density about  $10^3 \text{ cm}^{-3}$  (Kainulainen et al. 2011).

Within large clouds, and especially within the filaments, there may be small cores, which are much less massive but much denser. Theoretically, these are the sites of formation of individual stars, either single or binary (Williams et al. 2000). Their properties have been reviewed by di Francesco et al. (2007) and Ward-Thompson et al. (2007a). Those cores without evidence of ongoing star formation are called starless cores, and the subset of those that are gravitationally bound are called prestellar cores. Distinguishing these two requires a good mass estimate, independent of the virial theorem, and observations of lines that trace the kinematics. A sharp decrease in turbulence may provide an alternative way to distinguish a prestellar core from its surroundings (Pineda et al. 2010a).

While clouds and cores are reasonably well defined, intermediate structures are more problematic. Theoretically, one needs to name the entity that forms a cluster. Since large clouds can form multiple (or no) clusters, another name is needed. Williams et al. (2000) established the name “clump” for this structure. The premise was that this region should also be gravitationally bound, at least until the stars dissipate the remaining gas. Finding an observable correlative has been a problem (§2.5).

Finally, one must note that this hierarchy of structure is based on relatively large clouds. There are also many small clouds (Clemens & Barvainis 1988), some of which are their own clumps and/or cores. The suggestion by Bok & Reilly (1947) that these could be the sites of star formation was seminal.

### 2.3. *Dust as an ISM Tracer*

In the Milky Way, roughly 1% of the ISM is found in solid form, primarily silicates and carbonaceous material (Draine 2003) (see also a very useful website<sup>1</sup>). Dust

<sup>1</sup> <http://www.astro.princeton.edu/~draine/dust/dust.html>

grain sizes range from 0.35 nm to around 1  $\mu\text{m}$ , with evidence for grain growth in molecular clouds. The column density of dust can be measured by studying either the reddening (using colors) or the extinction of starlight, using star counts referenced to an unobscured field. The relation between extinction (e.g.,  $A_V$ ) and reddening [e.g.,  $E(B - V)$ ] is generally parameterized by  $R_V = A_V/E(B - V)$ . In the diffuse medium, the reddening has been calibrated against atomic and molecular gas to obtain  $N(\text{H I}) + 2N(\text{H}_2) = 5.8 \times 10^{21} \text{ cm}^{-2} E(B - V)(\text{mag})$ , not including helium (Bohlin et al. 1978). For  $R_V = 3.1$ , this relation translates to  $N(\text{H I}) + 2N(\text{H}_2) = 1.87 \times 10^{21} \text{ cm}^{-2} A_V(\text{mag})$ . This relation depends on metallicity, with coefficients larger by factors of about 4 for the LMC and 9 for the SMC (Weingartner & Draine 2001).

The relation derived for diffuse gas is often applied in molecular clouds, but grain growth flattens the extinction curve, leading to larger values of  $R_V$ , and a much flatter curve in the infrared (Flaherty et al. 2007; Chapman et al. 2009). More appropriate conversions can be found in the curves for  $R_V = 5.5$  in the website referenced above. There is evidence of continued grain growth in denser regions, which particularly affects the opacity at longer wavelengths, such as the mm/submm regions (Shirley et al. 2011).

Reddening and extinction of starlight provided early evidence of the existence of interstellar clouds (Barnard 1908). Lynds (1962) provided the mostly widely used catalog of “dark clouds” based on star counts, up to  $A_V \sim 6$  mag, at which point the clouds were effectively opaque at visible wavelengths. The availability of infrared photometry for large numbers of background stars from *2MASS*, *ISO*, and *Spitzer* toward nearby clouds has allowed extinction measurements up to  $A_V \sim 40$  mag. These have proved very useful in characterizing cloud structure and in checking the gas tracers discussed in §2.4. Extinction mapping with sufficiently high spatial resolution can identify cores (e.g., Alves et al. 2007), but many are not gravitationally bound (Lada et al. 2008), and they are likely to dissipate.

At wavelengths with strong, diffuse Galactic background emission, such as the mid-infrared, dust absorption against the continuum can be used in a way parallel to extinction maps (e.g., Bacmann et al. 2000; Stutz et al. 2007). The main uncertainties in deriving the gas column density are the dust opacity in the mid-infrared and the fraction of foreground emission.

The energy absorbed by dust at short wavelengths is emitted at longer wavelengths, from infrared to millimeter, with a spectrum determined by the grain temperature and the opacity as a function of wavelength. At wavelengths around 1 mm, the emission is almost always optically thin and close to the Rayleigh-Jeans limit for modest temperatures. (For  $T_d = 20\text{K}$ , masses, densities, etc. derived in the Rayleigh-Jeans limit at  $\lambda = 1$  mm must be multiplied by 1.5). Thus, the millimeter-wave continuum emission provides a good tracer of dust (and gas, with knowledge of the dust opacity) column density and mass.

As a by-product of studies of the CMB, *COBE*, *WMAP*, and *Planck* produce large-scale maps of mm/submm emission from the Milky Way. With *Planck*, the angular resolution reaches  $\theta = 4.7'$  at 1.4 mm in

an all-sky map of dust temperature and optical depth (Planck Collaboration et al. 2011b). Mean dust temperature increases from  $T_d = 14 - 15$  K in the outer Galaxy to 19 K around the Galactic center. A catalog of cold clumps with  $T_d = 7 - 17$  K, mostly within 2 kpc of the Sun, many with surprisingly low column densities, also resulted from analysis of *Planck* data (Planck Collaboration et al. 2011c). Herschel surveys will be providing higher resolution [ $25''$  at 350  $\mu\text{m}$  (Griffin et al. 2010) and  $6''$  at 70  $\mu\text{m}$  (Poglitsch et al. 2010)] images of the nearby clouds (André et al. 2010), the Galactic Plane (Molinari et al. 2010), and many other galaxies (e.g., Skibba et al. 2011; Wuyts et al. 2011). Still higher resolution is available at  $\lambda \geq 350$   $\mu\text{m}$  from ground-based telescopes at dry sites. Galactic plane surveys at wavelengths near 1 mm have been carried out in both hemispheres (Aguirre et al. 2011; Schuller et al. 2009). Once these are put on a common footing, we should have maps of the Galactic plane with resolution of  $20''$  to  $30''$ . Deeper surveys of nearby clouds (Ward-Thompson et al. 2007b), the Galactic Plane, and extragalactic fields are planned with SCUBA-2.

While studies from ground-based telescopes offer higher resolution, the need to remove atmospheric fluctuations leads to loss of sensitivity to structures larger than typically about half the array footprint on the sky (Aguirre et al. 2011). While the large-scale emission is lost, the combination of sensitivity to a minimum column density and a maximum size makes these surveys effectively select structures of a certain mean volume density. In nearby clouds, these correspond to dense cores (Enoch et al. 2009). For Galactic plane surveys, sources mainly correspond to clumps but can be whole clouds at the largest distances (Dunham et al. 2011b).

## 2.4. Gas Tracers

One troublesome aspect of extragalactic studies has been the determination of the amount and properties of the gas. We discuss first the atomic phase, then the molecular phase, and finally tracers of dense gas.

### 2.4.1. The Cold Atomic Phase

The cold, neutral atomic phase is traced by the hyperfine transition of hydrogen, occurring at 21 cm in the rest frame. This transition reaches optical depth of unity at

$$N(\text{H I}) = 4.57 \times 10^{20} \text{ cm}^{-2} (T_{\text{spin}}/100\text{K}) (\sigma_v/1\text{km s}^{-1}), \quad (4)$$

where  $T_{\text{spin}}$  is the excitation temperature, usually equal to the kinetic temperature,  $T_K$ , and  $\sigma_v$  is the velocity dispersion (eq. 8.11 in Draine 2011). For dust in the diffuse ISM of the Milky Way, this column density corresponds to  $A_V = 0.24$  mag, and optical depth effects can be quite important. The warm, neutral phase is difficult to study, as lines become broad and weak, but it has been detected (Kulkarni & Heiles 1988). A detailed analysis of both CNM and WNM can be found in Heiles & Troland (2003).

$$\text{With } I(\text{H I}) = \int S_\nu dv \text{ (Jy km s}^{-1}\text{),}$$

$$M(\text{H I})/M_\odot = 2.343 \times 10^5 (1+z)^{-1} (D_L/\text{Mpc})^2 I(\text{H I}), \quad (5)$$

not including helium (eq. 8.21 in Draine 2011, but note errata regarding  $(1+z)$  factor, which was in the numer-

ator in the 2011 edition). A coefficient of  $2.356 \times 10^5$  is in common use among H I observers (e.g., Walter et al. 2008; Catinella et al. 2010; Giovanelli et al. 2005; Meyer et al. 2004), usually traced to Roberts (1975). The difference is almost certainly caused by a newer value for the Einstein A value in Draine (2011).

#### 2.4.2. Molecular Gas

The most abundant molecule is  $H_2$ , but its spectrum is not a good tracer of the mass in molecular clouds. The primary reason is not, as often stated, the fact that it lacks a dipole moment, but instead the low mass of the molecule. The effect of low mass is that the rotational transitions require quite high temperatures to excite, making the bulk of the  $H_2$  in typical clouds invisible. Continuum optical depth at the mid-infrared wavelengths of these lines is also an impediment. The observed rotational  $H_2$  lines originate in surfaces of clouds, probing 1% to 30% of the gas in a survey of galaxies (e.g., Roussel et al. 2007).

Carbon monoxide (CO) is the most commonly used tracer of molecular gas because its lines are the strongest and therefore easiest to observe. These advantages are accompanied by various drawbacks, which MW observations may help to illuminate. Essentially, CO emission traces column density of molecular gas only over a very limited dynamic range. At the low end, CO requires protection from photodissociation and some minimum density to excite it, so it does not trace all the molecular (in the sense that hydrogen is in  $H_2$ ) gas, especially if metallicity is low. At the high end, emission from CO saturates at modest column densities. A more complete review by A. Bolatto of the use of CO to trace molecular gas is scheduled for a future ARAA, so we briefly highlight the issues here.

CO becomes optically thick at very low total column densities. Using CO intensity to estimate the column density of a cloud is akin to using the presence of a brick wall to estimate the depth of the building behind it. The isotopologues of CO ( $^{13}\text{CO}$  and  $\text{C}^{18}\text{O}$ ) provide lower optical depths, but at the cost of weaker lines. To use these, one needs to know the isotope ratios; these are fairly well known in the Milky Way (Wilson & Rood 1994), but they may differ substantially in other galaxies. In addition, the commonly observed lower transitions of CO are very easily thermalized ( $T_{ex} = T_K$ ) making them insensitive to the presence of dense gas.

The common practice in studies of MW clouds is to use a combination of CO and  $^{13}\text{CO}$  to estimate optical depth and hence CO column density ( $N(\text{CO})$ ). One can then correlate  $N(\text{CO})$  or its isotopes against extinction to determine a conversion factor (Dickman 1978; Frerking et al. 1982). A recent, careful study of CO and  $^{13}\text{CO}$  toward the Taurus molecular cloud shows that  $N(\text{CO})$  traces  $A_V$  up to 10 mag in some regions but only up to 4 mag in other regions, and other issues cause problems below  $A_V = 3$  mag (Pineda et al. 2010b). Freeze-out of CO and conversion to  $\text{CO}_2$  ice causes further complications in cold regions of high column density (Lee et al. 2003; Pontoppidan et al. 2008; Whittet et al. 2007), but other issues likely dominate the interpretational uncertainties for most extragalactic CO observations.

Since studies of other galaxies generally have only CO observations available, the common practice has been to

relate  $H_2$  column density ( $N(H_2)$ ) to the integrated intensity of CO [ $I(\text{CO}) = \int T dv$  ( $\text{K km s}^{-1}$ )] via the infamous “X-factor”:  $N(H_2) = X(\text{CO})I(\text{CO})$ . For example, Kennicutt (1998b) used  $X(\text{CO}) = 2.8 \times 10^{20} \text{ cm}^{-2} (\text{K km s}^{-1})^{-1}$ .

Pineda et al. (2010b) find  $X(\text{CO}) = 2.0 \times 10^{20} \text{ cm}^{-2} (\text{K km s}^{-1})^{-1}$  in the parts of the cloud where both CO and  $^{13}\text{CO}$  are detected along individual sight lines. CO does emit beyond the area where  $^{13}\text{CO}$  is detectable and even, at a low level, beyond the usual detection threshold for CO. Stacking analysis of positions beyond the usual boundary of the Taurus cloud suggest a factor of two additional mass in this transition region (Goldsmith et al. 2008). Such low intensity, but large area, emission could contribute substantially to observations of distant regions in our galaxy and in other galaxies. For the outer parts of clouds, where only CO is detected, and only by stacking analysis,  $X(\text{CO})$  is six times higher (Pineda et al. 2010b). Even though about a quarter of the total mass is in this outer region, they argue that the best single value to use is  $X(\text{CO}) = 2.3 \times 10^{20} \text{ cm}^{-2} (\text{K km s}^{-1})^{-1}$ , similar to values commonly adopted in extragalactic studies. When possible, we will use  $X(\text{CO}) = 2.3 \times 10^{20} \text{ cm}^{-2} (\text{K km s}^{-1})^{-1}$  for this paper. In contrast, Liszt et al. (2010) argue that  $X(\text{CO})$  stays the same even in diffuse gas. If they are right, much of the integrated CO emission from some parts of galaxies could arise in diffuse, unbound gas.

Comparing to extinction measures in two nearby clouds extending up to  $A_V = 40$  mag, Heiderman et al. (2010) found considerable variations from region to region, with  $I(\text{CO})$  totally insensitive to increased extinction in many regions. Nonetheless, when averaged over the whole cloud, the standard  $X(\text{CO})$  would cause errors in mass estimates of  $\pm 50\%$ , systematically overestimating the mass for  $\Sigma_{mol} < 150 \text{ M}_\odot \text{ pc}^{-2}$  and underestimating for  $\Sigma_{mol} > 200 \text{ M}_\odot \text{ pc}^{-2}$ . Simulations of turbulent gas with molecule formation also suggest that  $I(\text{CO})$  can be a very poor tracer of  $A_V$  (Glover et al. 2010). Overall, the picture at this point is that measuring the extent of the brick wall will not tell you anything about particularly deep or dense extensions of the building, but if the buildings are similar, the extent of the wall is a rough guide to the total mass of the building (cf. Shetty et al. 2011b).

Following that thought, the luminosity of CO  $J = 1 \rightarrow 0$  is often used as a measure of cloud mass, with the linewidth reflecting the virial theorem in a crude sense. In most extragalactic studies, individual clouds are not resolved, and the luminosity of CO is essentially a cloud counting technique (Dickman et al. 1986). Again, this idea works only if the objects being counted have rather uniform properties. In this approach,  $M = \alpha_{\text{CO}} L(\text{CO})$ . For the standard value for  $X(\text{CO})$  discussed above ( $X(\text{CO}) = 2.3 \times 10^{20} \text{ cm}^{-2} (\text{K km s}^{-1})^{-1}$ )  $\alpha_{\text{CO}} = 3.6 \text{ M}_\odot (\text{K km s}^{-1} \text{ pc}^2)^{-1}$  without helium, and  $\alpha_{\text{CO}} = 4.6 \text{ M}_\odot (\text{K km s}^{-1} \text{ pc}^2)^{-1}$  with correction for helium.

The effects of cloud temperature, density, metallicity, etc. on mass estimation from CO were discussed by Maloney & Black (1988), who concluded that large variations in the conversion factor are likely. Ignoring metallicity ef-

fects, they would predict  $X(\text{CO}) \propto n^{0.5} T_K^{-1}$ , where  $n$  is the mean density in the cloud. Shetty et al. (2011b) find a weaker dependence on  $T_K$ ,  $X(\text{CO}) \propto T_K^{-0.5}$ . These scalings rests on some arguments that may not apply in other galaxies. Further modeling with different metallicities (Shetty et al. 2011a; Feldmann et al. 2012) has begun to provide some perspective on the range of behaviors likely in other galaxies.

There is observational evidence for changes in  $\alpha_{\text{CO}}$  in centers of galaxies. In the MW central region, Oka et al. (1998) suggest a value for  $X(\text{CO})$  a factor of 10 lower than in the MW disk. The value of  $\alpha_{\text{CO}}$  appears to decrease by factors of 2-5 in nearby galaxy nuclei (e.g., Meier & Turner 2004; Meier et al. 2008), and by a factor of about 5-6 in local ULIRGs (Downes & Solomon 1998; Downes et al. 1993), and probably by a similar factor in high-redshift, molecule-rich galaxies (Solomon & Vanden Bout 2005).

A compilation of measurements indicates that  $\alpha_{\text{CO}}$  decreases from the usually assumed value with increasing surface density of gas once  $\Sigma_{\text{mol}} > 100 \text{ M}_{\odot} \text{ pc}^{-2}$  (Fig. 1, Tacconi et al. 2008). This  $\Sigma_{\text{mol}}$  corresponds to  $A_V \sim 10$  mag, about the point where CO fails to trace column density in Galactic clouds, and the point where the beam on another galaxy might be filled with CO-emitting gas. Variation in  $\alpha_{\text{CO}}$  has a direct bearing on interpretation of starbursts (§6), and it is highly unlikely that  $\alpha_{\text{CO}}$  is simply bimodal over the full range of star forming environments. Indeed, Narayanan et al. (2012) use a grid of model galaxies to infer a smooth function of  $I(\text{CO})$ :  $\alpha_{\text{CO}} = \min[6.3, 10.7 \times I(\text{CO})^{-0.32}] Z'^{-0.65}$ , where  $Z'$  is the metallicity divided by the solar value.

Other methods have been used to trace gas indirectly, including gamma-ray emission and dust emission. Gamma-rays from decay of pions produced from high-energy cosmic rays interacting with baryons in the ISM directly trace all the matter if one knows the cosmic ray flux (e.g., Bloemen 1989). Recent analysis of gamma-ray data from *Fermi* have inferred a low value for  $X(\text{CO})$  of  $(0.87 \pm 0.05) \times 10^{20} \text{ cm}^{-2} (\text{K km s}^{-1})^{-1}$  in the solar neighborhood (Abdo et al. 2010). This value is a factor of three lower than other estimates and early results from dust emission, using *Planck*, which found  $X(\text{CO}) = (2.54 \pm 0.13) \times 10^{20} \text{ cm}^{-2} (\text{K km s}^{-1})^{-1}$  for the solar neighborhood. (Planck Collaboration et al. 2011b).

Abdo et al. (2010) also inferred the existence of “dark gas”, which is not traced by either H I or CO, surrounding the CO-emitting region in the nearby Gould Belt clouds, with mass of about half of that traced by CO. Planck Collaboration et al. (2011b) have also indicated the existence of “dark gas” with mass 28% of the atomic gas and 118% of the CO-emitting gas in the solar neighborhood. The dark gas appears around  $A_V = 0.4$  mag, and is presumably the CO-poor, but  $\text{H}_2$ -containing, outer parts of clouds (e.g., Wolfire et al. 2010), which can be seen in [CII] emission at  $158 \mu\text{m}$  and in fluorescent  $\text{H}_2$  emission at  $2 \mu\text{m}$  (e.g., Pak et al. 1998). It is dark only if one restricts attention to H I and CO. At low metallicities, the layer of  $\text{C}^+$  grows, and a given CO luminosity implies a larger overall cloud (see Fig. 14 in Pak et al. 1998). However, Planck Collaboration et al. (2011b) also suggest that the dark gas may include some gas that is primarily atomic, but not traced by H I emission, owing

to optical depth effects.

Dust emission is now being used as a tracer of gas for other galaxies. Maps of H I gas are used to break the degeneracy between the gas to dust ratio  $\delta_{\text{gdr}}$  and  $\alpha'_{\text{CO}}$  in the following equation:

$$\delta_{\text{gdr}} \Sigma_{\text{dust}} = \alpha'_{\text{CO}} I(\text{CO}) + \Sigma_{\text{HI}}. \quad (6)$$

Leroy et al. (2011) minimize the variation in  $\delta_{\text{gdr}}$  to find the best fit to  $\alpha'_{\text{CO}}$  in several nearby galaxies. They determine  $\Sigma_{\text{dust}}$  from *Spitzer* images of  $160 \mu\text{m}$  emission, with the dust temperature (or equivalently the external radiation field) constrained by shorter wavelength far-infrared emission. This method should measure everything with substantial dust that is *not* H I, so includes the so-called “dark molecular gas.” They find that  $\alpha'_{\text{CO}} = 3 - 9 \text{ M}_{\odot} \text{ pc}^{-2} (\text{K km s}^{-1})^{-1}$ , similar to values based on MW studies, for galaxies with metallicities down to  $12 + [\text{O}/\text{H}] \sim 8.4$ , below which  $\alpha'_{\text{CO}}$  increases sharply to values like 70. Their method does not address the column density within clouds, but only the average surface density on scales larger than clouds. For galaxies not too different from the MW, the standard  $\alpha'_{\text{CO}}$  will roughly give molecular gas masses, but in galaxies with lower metallicity, the effects can be large. An extreme is the SMC, where  $\alpha'_{\text{CO}} \sim 220 \text{ M}_{\odot} \text{ pc}^{-2} (\text{K km s}^{-1})^{-1}$  (Bolatto et al. 2011). Maps of dust emission at longer wavelengths should decrease the sensitivity to dust temperature.

#### 2.4.3. Dense Gas Tracers

Lines other than CO  $J = 1 \rightarrow 0$  generally trace warmer (e.g., higher  $J$  CO lines) and/or denser (e.g., HCN, CS, ...) gas. Wu et al. (2010a) showed that the line luminosities of commonly used tracers (CS  $J = 2 \rightarrow 1$ ,  $J = 5 \rightarrow 4$ , and  $J = 7 \rightarrow 6$ ; HCN  $J = 1 \rightarrow 0$ ,  $J = 3 \rightarrow 2$ ) correlate well with the virial mass of dense gas; indeed most follow relations that are close to linear. Since these lines are optically thick, the linear correlation is somewhat surprising, but it presumably has an explanation similar to the cloud-counting argument offered above for CO. Collectively, we refer to these lines as “dense gas tracers”, but the effective densities increase with  $J$  and vary among species (see Evans 1999; Reiter et al. 2011b for definitions and tables of effective and critical densities). As an example for HCN  $J = 1 \rightarrow 0$ ,

$$\log(L'_{\text{HCN}1-0}) = 1.04 \times \log(M_{\text{Vir}}(R_{\text{HCN}1-0})) - 1.35 \quad (7)$$

from a robust estimation fit to data on dense clumps in the MW (Wu et al. 2010a). The line luminosities of other dense gas tracers also show strong correlations with both virial mass (Wu et al. 2010a) and the mass derived from dust continuum observations (Reiter et al. 2011b).

These tracers of dense gas are of course subject to the same caveats about sensitivity to physical conditions, such as metallicity, volume density, turbulence, etc., as discussed above for CO. In fact, the other molecules are more sensitive to photodissociation than is CO, so they will be even more dependent on metallicity (e.g., Rosolowsky et al. 2011). Dense gas tracers should become much more widely used in the ALMA era, but caution is needed to avoid the kind of over-simplification that has tarnished the reputation of CO. Observations of multiple transitions and rare isotopes, along with realistic models, will help (e.g., García-Burillo et al. 2012).

#### 2.4.4. Summary

What do extragalactic observations of molecular tracers actually measure? None are actually tracing the surface density of a smooth medium, with the possible exception of the most extreme starbursts. The luminosity of CO is a measure of the number of emitting structures times the mean luminosity per structure. Dense gas tracers work in a similar way, but select gas above a higher density threshold than does CO. For CO  $J = 1 \rightarrow 0$ , the structure is the CO emitting part of a cloud, which shrinks as metallicity decreases. For dense gas tracers, the structure is the part of a cloud dense enough to produce significant emission, something like a clump if conditions are like the MW, but even more sensitive to metallicity. Using a conversion factor, one gets a “mass” in those structures.

Estimates of the conversion factors for CO vary by factors of 3 for the solar neighborhood and at least an order of magnitude at low metallicity and by at least half an order of magnitude for our own Galactic Center and for extreme systems like ULIRGs. Dividing by the area of the galaxy or the beam, one gets “ $\Sigma_{mol}$ ”, which really should be thought of as an area filling factor of the structures being probed times some crude estimate of the mass per structure. That estimate depends on conditions in the structures, such as density, temperature, and abundance and on the external radiation field and the metallicity. Once the  $L(\text{CO})$  translates to surface densities above that of individual clouds ( $\Sigma_{mol} > \sim 100 \text{ M}_{\odot} \text{ pc}^{-2}$ ), the interpretation may change as the area filling factor can now exceed unity. Large ranges of velocity in other galaxies (if not exactly face-on) allow  $I(\text{CO})$  to still count clouds above this threshold, but the clouds may no longer be identical. The full range of inferred molecular surface densities in other galaxies inferred from CO, assuming a constant conversion factor, is a factor of  $10^3$  (§6); given that CO traces  $\Sigma_{mol}$  only over a factor of 10 at best in well-studied clouds in the MW (Pineda et al. 2010b; Heiderman et al. 2010), this seems a dangerous extrapolation.

#### 2.5. Mass Functions of Stars, Clusters, and Gas Structures

The mass functions of the structures in molecular clouds (§2.2) are of considerable interest in relation to the origin of the mass functions of clusters (clumps) and stars (cores). Salpeter (1955) fit the initial mass function (IMF) of stars to a power law in  $\log M_*$  with exponent  $\gamma_* = 1.35$ , or  $\alpha_* = 2.35$  (see §1.2 for definitions). More recent determinations over a wider range of masses, including brown dwarfs, indicate a clear flattening at lower masses, either as broken power laws (Kroupa et al. 1993) or a log-normal distribution (Miller & Scalo 1979; Chabrier 2003). A detailed study of the IMF in the nearest massive young cluster, Orion, with stars from 0.1 to 50  $\text{M}_{\odot}$  with a mean age of 2 Myr, shows a peak between 0.1 and 0.3  $\text{M}_{\odot}$ , depending on evolutionary models, and a deficit of brown dwarfs relative to the field IMF (Da Rio et al. 2012). Steeper IMFs in massive elliptical galaxies have been suggested by van Dokkum & Conroy (2011). Zinnecker & Yorke (2007) summarize the evidence for a real (not statistical) cut-off in the IMF around 150  $\text{M}_{\odot}$  for star formation in the MW and Mag-

ellanic Clouds. Variations in the IMF with environment are plausible, but convincing evidence for variation remains elusive (Bastian et al. 2010).

The masses of embedded young clusters (Lada & Lada 2003), OB associations (McKee & Williams 1997), and massive open clusters (Elmegreen & Efremov 1997; Zhang & Fall 1999), follow a similar relation with  $\gamma_{cluster} \sim 1$ . Studies of clusters in nearby galaxies have also found  $\gamma_{cluster} = 1 \pm 0.1$ , with a possible upper mass cutoff or turn-over around  $1 - 2 \times 10^6 \text{ M}_{\odot}$  (Gieles et al. 2006), perhaps dependent on the galaxy (but see Chandar et al. 2011). In contrast, the most massive known open clusters in the MW appear to have a mass of  $(6 - 8) \times 10^4 \text{ M}_{\odot}$  (Portegies Zwart et al. 2010; Davies et al. 2011; Homeier & Alves 2005).

The mass functions of clusters and stars are presumably related to the mass functions of their progenitors, clouds or clumps, and cores. For comparison to structures in clouds, we will use the distributions versus mass, rather than logarithmic mass, so our points of comparison will be  $\alpha_* = 2.3$  and  $\alpha_{cluster} = 2$ . From surveys of emission from CO  $J = 1 \rightarrow 0$  in the outer galaxy, where confusion is less problematic, Heyer et al. (2001) found a size distribution of clouds,  $dN/dr \propto r^{-3.2 \pm 0.1}$ , with no sign of a break from the power-law form from 3 to 60 pc. The mass function, using the definition in equation 2, was fitted by  $\alpha_{cloud} = 1.8 \pm 0.03$  over the range 700 to  $1 \times 10^6 \text{ M}_{\odot}$ . Complementary surveys of the inner Galaxy found  $\alpha_{cloud} = 1.5$  up to  $M_{max} = 10^{6.5} \text{ M}_{\odot}$  (Rosolowsky 2005). The upper cut-off around  $3 - 6 \times 10^6 \text{ M}_{\odot}$  appears to be real, despite issues of blending of clouds (Williams & McKee 1997; Rosolowsky 2005). Using  $^{13}\text{CO } J = 1 \rightarrow 0$ , which selects somewhat denser parts of clouds, Roman-Duval et al. (2010) found  $\alpha_{^{13}\text{CO}} = 1.75 \pm 0.23$  for  $M_{cloud} > 10^5 \text{ M}_{\odot}$ . Clumps within clouds, identified by mapping  $^{13}\text{CO}$  or  $\text{C}^{18}\text{O}$ , have a similar value for  $\alpha_{clump} = 1.4 - 1.8$  (Kramer et al. 1998). All results agree that most clouds are small, but, unlike stars or clusters, most mass is in the largest clouds ( $\alpha_{cloud} < 2$ ).

Studies of molecular cloud properties in other galaxies have been recently reviewed (Fukui & Kawamura 2010; Blitz et al. 2007). Mass functions of clouds in nearby galaxies appear to show some differences, though systematic effects introduce substantial uncertainty (Wong et al. 2011; Sheth et al. 2008). Evidence for a higher value of  $\alpha_{cloud}$  has been found for the LMC (Fukui et al. 2001; Wong et al. 2011) and M33 (Engargiola et al. 2003; Rosolowsky 2005). Most intriguingly, the mass function appears to be steeper in the interarm regions of M51 than in the spiral arms (E. Schinnerer and A. Hughes, personal communication), possibly caused by the aggregation of clouds into larger structures within arms and disaggregation as they leave the arms (Koda et al. 2009).

Much work has been done recently on the mass function of cores, and Herschel surveys of nearby clouds will illuminate this topic (e.g., André et al. 2010). At this point, it seems that the mass function of cores is clearly steeper than that of clouds, much closer to that of stars (Motte et al. 1998; Enoch et al. 2008; Sadavoy et al. 2010). A turnover in the mass function appears at a mass about 3-4 times that seen in the stellar IMF (Alves et al. 2007; Enoch et al. 2008). The similarity of  $\alpha_{core}$  to  $\alpha_*$  supports the idea that the cores are the immediate



precursors of stars and that the mass function of stars is set by the mass function of cores. In this picture, the offset of the turnover implies that about 0.2 to 0.3 of the core mass winds up in the star, consistent with simulations that include envelope clearing by outflows (e.g., Dunham et al. 2010). Various objections and caveats to this appealing picture have been registered (e.g., Swift & Williams 2008; Reid et al. 2010; Clark et al. 2007; Hatchell & Fuller 2008).

Note that no such tempting similarity exists between the mass function of clusters and the mass function of clumps defined by  $^{13}\text{CO}$  maps, questioning whether that observational definition properly fits the theoretical concept of a clump as a cluster-forming entity. Structures marked by stronger emission in  $^{13}\text{CO}$  or  $\text{C}^{18}\text{O}$  (Rathborne et al. 2009) are not always clearly bound gravitationally. Ground and space-based imaging of submillimeter emission by dust (e.g., Men'shchikov et al. 2010) offer promise in this area, but information on velocity structure will also be needed. The data so far suggest that the structure is primarily filamentary, more like that of clouds than that of cores. CS, HCN and other tracers of much denser gas (§2.4), along with dust continuum emission (§2.3) have identified what might be called “dense clumps”, which do appear to have a mass function similar to that of clusters (Shirley et al. 2003; Beltrán et al. 2006; Reid & Wilson 2005),

The comparison of mass functions supports the idea (McKee & Ostriker 2007) that cores are the progenitors of stars and dense clumps are the progenitors of clusters, with clouds less directly related. Upper limits to the mass function of clumps would then predict upper limits to the mass function of clusters, unless nearby clumps result in merging of clusters. Because most clouds and many clumps are more massive than the most massive stars, it is less obvious that an upper limit to stellar masses results from a limit on cloud or clump masses. If clump masses are limited *and* if the mass of the most massive star to form depends causally (not just statistically) on the mass of the clump or cloud, the integrated galactic IMF (IGIMF) can be steepened (Kroupa & Weidner 2003; Weidner & Kroupa 2006). We discuss the second requirement in §4.2 and consequences of this controversial idea in §3.3 and §6.4.

### 3. SFR DIAGNOSTICS: THE IMPACT OF MULTI-WAVELENGTH OBSERVATIONS

The influx of new observations over the past decade has led to major improvements in the calibration and validation of diagnostic methods for measuring SFRs in galaxies. Whereas measuring uncertainties of factors of two or larger in SFRs were commonplace ten years ago, new diagnostics based on multi-wavelength data are reducing these internal uncertainties by up to an order of magnitude in many instances. These techniques have also reduced the impact of many systematic errors, in particular uncertainties due to dust attenuation, though others such as the IMF (§2.5) remain important limiting factors.

A detailed discussion of SFR diagnostics and their calibrations was given in K98, and here we highlight progress made since that review was published. In §3.8, we compile updated calibrations for the most commonly used indices, based on updated evolutionary synthesis models

and IMF compared to K98. The new challenges which come with spatially-resolved measurements of galaxies are discussed in §3.9.

#### 3.1. Star Counting and CMD Analysis

The most direct way to measure star formation rates is to count the number of identifiable stars of a certain age. Ideally, one would have reliable masses and ages for each star and the mean star formation rate would be given by

$$\langle \dot{M}_* \rangle = \sum_{M_* = M_l}^{M_u} N(M_*, t_*) M_* / t_* \quad (8)$$

where  $N(M_*, t_*)$  is the number of stars in a mass bin characterized by mass  $M_*$  and a lifetime bin (the time since formation) characterized by  $t_*$ , and the star formation rate would be averaged over the longest value of  $t_*$  in the sum. In practice, complete information is not available, and one needs to limit the allowed lifetimes to find the star formation rate over a certain period. In particular, for nearby clouds in the MW, nearly complete lists of young stellar objects (YSOs) with infrared excesses are available. If one assumes that the YSOs sample the IMF in a typical way, one can derive the mean mass of stars ( $\langle M_* \rangle$ ), and the equation becomes

$$\langle \dot{M}_* \rangle = N(\text{YSOs}) \langle M_* \rangle / t_{\text{excess}}. \quad (9)$$

With currently favored IMFs,  $\langle M_* \rangle = 0.5 M_\odot$ . The main source of uncertainty is in  $t_{\text{excess}}$ , the duration of an infrared excess (§4.1).

For young clusters one can determine mean ages from fitting isochrones to a color-magnitude diagram, and measure  $\dot{M}_*$  assuming coeval formation as long as some stars have not yet reached the main sequence. Some clusters have measurements of stars down to very low masses (e.g., the Orion Nebula Cluster, Hillenbrand 1997), but most need corrections for unseen low-mass stars. For older clusters one can derive the total mass, but not (directly) the duration of star formation, which has to be assumed.

In principle similar techniques can be applied on a galaxy-wide basis. Beyond the Magellanic Clouds, current instruments cannot resolve individual YSOs in most regions, and as a result most studies of SFRs in galaxies are based either on measurements of massive O-type and/or Wolf-Rayet stars (see K98) or on measurements of the entire color-magnitude diagram (CMD). Considerable progress has been made recently in using spatially-resolved mapping of CMDs to reconstruct spatially and age-resolved maps of star formation in nearby galaxies. Many of these use the distribution of blue helium-burning stars in the CMD (e.g., Dohm-Palmer et al. 2002), but more recent analyses fit the entire upper CMDs to synthetic stellar populations to derive estimates of spatially resolved stellar age distributions with formal uncertainties (e.g., Dolphin 2002; Weisz et al. 2008). This technique does not have sufficient age resolution to determine accurate SFRs for ages less than  $\sim 10$  Myr, but when applied to high quality datasets such as those which can be obtained with HST, they can provide sufficient age resolution to constrain the temporal behaviors and changes in the spatial distributions of formation over the past 100

Myr or longer (e.g., Weisz et al. 2008; Williams et al. 2011).

### 3.2. *Ultraviolet Continuum Measurements: The Impact of GALEX*

The near-ultraviolet emission of galaxies longward of the Lyman-continuum break directly traces the photospheric emission of young stars and hence is one of the most direct tracers of the recent SFR. For a conventional IMF, the peak contribution to the integrated UV luminosity of a young star cluster arises from stars with masses of several solar masses. Consequently this emission traces stars formed over the past 10–200 Myr, with shorter timescales at the shortest wavelengths (see Table 1).

For extragalactic studies, this subject has been revolutionised by the launch of the Galaxy Evolution Explorer (GALEX) mission (Martin et al. 2005a). It imaged approximately two thirds of the sky in far-ultraviolet (FUV; 155 nm) and near-ultraviolet (NUV; 230 nm) channels to limiting source fluxes  $m_{AB} \sim 20.5$ , and obtained deeper full-orbit or multi-orbit imaging ( $m_{AB} \geq 23$ ) for selected galaxies and fields such as those in the Sloan Digital Sky Survey (SDSS). The spatial resolution (4.5'' to 6'' FWHM) of the imager makes it an especially powerful instrument for integrated measurements of distant galaxies and resolved mapping of the nearest external galaxies. Although most scientific applications of GALEX data to date have arisen from its imaging surveys, a series of spectroscopic surveys and pointed observations of varying depths were carried out as well (Martin et al. 2005a).

The main impacts of GALEX for this subject are summarized in §5. Broadly speaking its largest impacts were in providing integrated UV fluxes (and hence SFR estimates) for hundreds of thousands of galaxies, and in exploiting the dark sky from space at these wavelengths to reveal star formation at low surface brightnesses and intensities across a wide range of galactic environments.

Other spaceborne instruments have also provided important datasets in this wavelength region, including the XMM Optical Monitor (Mason et al. 2001) and the Swift UV/Optical Telescope (Roming et al. 2005). Although these instruments were primarily designed for follow-up of X-ray and gamma-ray observations, they also have been used to image nearby and distant galaxies, with the advantage of higher spatial resolution ( $\sim 1''$  FWHM). Several important studies have also been published over the past decade from observations made with the Ultraviolet Imaging Telescope on the ASTRO missions (Stecher et al. 1997; Marcum et al. 2001). The Hubble Space Telescope continues to be a steady source of observations (mainly in the NUV) for targeted regions in nearby galaxies.

The primary disadvantage of the ultraviolet is its severe sensitivity to interstellar dust attenuation. The availability of new data from GALEX and other facilities has stimulated a fresh look at this problem. If the intrinsic color of the emitting stellar population is known *a priori*, the FUV–NUV color or the UV spectral slope (usually denoted  $\beta$ ) can be used to estimate the dust attenuation, and numerous calibrations have been published (e.g., Calzetti et al. 1994; Kong et al. 2004; Seibert et al. 2005; Johnson et al. 2007; Salim et al. 2007; Treyer et al. 2007; Hao et al. 2011). The accuracy of these pre-

scriptions rests heavily on the presumed (but uncertain) intrinsic colors, the shape of the dust extinction curve, and the complicated effects of geometry and scattering when averaging over a large physical region (e.g., Gordon et al. 2001).

The abundance of high quality far-infrared observations of nearby galaxies has made it possible to test how well the UV colors correlate with independent estimates of the dust attenuation from the IR/UV flux ratios. Earlier observations of bright starburst galaxies suggest a tight relation between the logarithmic IR/UV ratio (often termed the “IRX”) and UV color (e.g., Meurer et al. 1999), and indeed this “IRX– $\beta$  relation” provided the primary means for calibrating the color versus attenuation relation. Subsequent observations of a wider range of galaxies, however, has revealed a much larger scatter in the relation (e.g., Boquien et al. 2012). When galaxies of all types are considered, the scatter in actual FUV attenuations for a fixed FUV–NUV color can easily be two orders of magnitude. Even when the comparison is restricted to galaxies with intrinsically high SFRs (as might be observed at high redshift), the uncertainties can easily reach an order of magnitude. As a result, more weight is being applied to alternative estimates of attenuation corrections and SFRs based on combinations of UV with IR measurements (§3.7).

### 3.3. *Emission-Line Tracers*

The remaining SFR indicators to be discussed here rely on measuring starlight that has been reprocessed by interstellar gas or dust, or on tracers related to the death of massive stars. The most widely applied of these are the optical and near-infrared emission lines from ionized gas surrounding massive young stars. For a conventional IMF, these lines trace stars with masses greater than  $\sim 15 M_{\odot}$ , with the peak contribution from stars in the range 30–40  $M_{\odot}$ . As such, the lines (and likewise the free-free radio continuum) represent a nearly instantaneous measure of the SFR, tracing stars with lifetimes of  $\sim 3$ –10 Myr (Table 1).

The application of H $\alpha$  and other emission line SFR tracers has expanded dramatically in the last decade, through very large spectroscopic surveys of samples of local and distant galaxies, narrow-band emission-line imaging surveys, and large imaging surveys of nearby galaxies designed to study spatial variations in the SFR. Advances in near-infrared instrumentation have also led to the first systematic surveys in the Paschen and Brackett series lines, as well as for H $\alpha$  observed at high redshifts. Results from several of these surveys are discussed and referenced in §5.

The H $\alpha$  emission line remains the indicator of choice for observations of local and distant galaxies alike, but for moderate redshifts, the bluer visible lines have been applied, in particular the [O II] forbidden line doublet at 372.7 nm. This feature is subject to severe systematic uncertainties from dust attenuation and excitation variations in galaxies. K98 published a single SFR calibration for the line, but subsequent analyses (e.g., Jansen et al. 2001; Kewley et al. 2004; Moustakas et al. 2006) have shown that the systematic effects must be removed or at least calibrated to first order for reliable measurements. Even then, the uncertainties in the [O II]-based SFRs are much larger than for H $\alpha$ .

Over the past decade, increasing attention has been given to measurements of the redshifted Ly $\alpha$  line ( $\lambda_{rest} = 121.6\text{ nm}$ ) as a tracer of star-forming galaxies, especially at high redshifts where it provides unique sensitivity to both low-mass star-forming galaxies and intergalactic gas clouds or “blobs” (e.g., Ouchi et al. 2009, 2010). The strength of the line (8.7 times stronger than H $\alpha$  for Case B recombination) makes it an attractive tracer in principle, but in realistic ISM environments the line is subject to strong quenching from the combination of resonant trapping and eventual absorption by dust, usually quantified in terms of a Ly $\alpha$  escape fraction. As a result Ly $\alpha$  surveys to date have been mainly used for identifying large samples of distant star-forming galaxies. Applying the line as a quantitative SFR tracer requires an accurate measurement of the escape fraction. Several ongoing studies are quantifying this parameter by comparing Ly $\alpha$  fluxes of galaxies with independent SFR tracers such as H $\alpha$  or the UV continuum (e.g., Atek et al. 2009; Scarlata et al. 2009; Blanc et al. 2011; Hayes et al. 2011). These show that the escape fraction varies wildly between galaxies with a range of more than two orders of magnitude (order 0.01 to 1), but also increases systematically with redshift. It is possible that Ly $\alpha$  will prove to be a powerful SFR tracer for the highest-redshift objects, but in view of the large scatter and systematic uncertainties associated with its use we have chosen not to include a SFR calibration of the line in this review.

Other workers have investigated the efficacy of the infrared fine-structure cooling lines, which arise in H II regions or PDRs, as quantitative SFR tracers. Ho & Keto (2007) compiled data from ISO and Spitzer on the [Ne II]12.8  $\mu\text{m}$  and [Ne III]15.6  $\mu\text{m}$  lines, and found that the sum of the line fluxes correlates well with hydrogen recombination line fluxes, with a scatter of  $\sim 0.3$  dex. In a similar vein, Boselli et al. (2002) and Rodríguez-Fernández et al. (2006) have investigated the applicability of the [C II]158  $\mu\text{m}$  line as a SFR measure. They found good general correspondance between the [C II] luminosity and other measures of the SFR such as ionized gas and dust emission, but the scatter in the relationships is at least a factor of ten. Even larger variations in  $L_{[\text{C II}]} / L_{\text{IR}}$  were found in a more diverse sample of star-forming galaxies by Malhotra et al. (1997). The availability of a rich new set of [C II] observations from Herschel, combined with the detection of redshifted [C II] emission in submillimeter galaxies (SMGs) from ground-based instruments, has sparked a resurgence of interest in this application.

The largest systematic errors affecting H $\alpha$ -based SFRs are dust attenuation and sensitivity to the population of the upper IMF in regions with low absolute SFRs. For regions with modest attenuations the ratios of Balmer recombination lines (Balmer decrement) can be used to correct for dust, and this method has been applied in a number of large spectrophotometric surveys of nearby galaxies (e.g., Kewley et al. 2002; Brinchmann et al. 2004; Moustakas et al. 2006). The Balmer decrements offer only approximate corrections for attenuation because of variations on scales smaller than the resolution. These variations may lead to an underestimate of the extinction because lines of sight with low extinction are more heavily weighted within the beam. This problem can

be addressed partly by adopting a reddening law which compensates in part for these departures from a pure foreground scheme geometry (e.g., Charlot & Fall 2000). The attenuation of the emission lines is found to be systematically higher than that of the continuum starlight at the same wavelengths (e.g., Calzetti et al. 1994), which presumably reflects the higher concentrations of dust in the young star-forming regions.

As is the case with UV-based SFRs, the availability of far-infrared maps and luminosities for nearby galaxies has also made it possible to calibrate *multi-wavelength methods* for applying dust attenuation corrections to these measurements (§3.7). They reveal that the Balmer decrement provides reasonably accurate attenuation corrections in normal galaxies, where attenuations are modest (typically 0–1 mag at H $\alpha$ ), and care is taken to correct the emission-line fluxes for underlying stellar absorption. The Balmer decrement method for estimating dust attenuation breaks down badly, however in circumnuclear starbursts or other dusty galaxies (e.g., Moustakas et al. 2006). With the advent of large-format integral-field spectrographs there is promise of applying Balmer decrement measurements on a spatially-resolved basis in galaxies (e.g., Blanc 2010; Sánchez et al. 2012).

The accuracy of SFRs derived from emission lines will also degrade in regions where the SFR is so low that one enters the regime of small number statistics in the population of massive ionizing stars. If the IMF itself were completely blind to the SFR, we would expect such effects to become apparent below H $\alpha$  luminosities of order  $10^{38} \text{ erg s}^{-1}$ , or SFRs of order  $0.001 M_{\odot} \text{ yr}^{-1}$  (e.g., Cerviño et al. 2003). At the very least, this effect will produce a much larger scatter in ionizing flux per unit SFR in this regime. In low-SFR regions, this sampling noise can be exacerbated by the short lifetimes of the ionizing stars, producing large temporal fluctuations in H $\alpha$  emission even for a fixed longer-term SFR. As a result, other tracers (e.g., FUV emission) tend to provide more accurate and sensitive measurements of the SFR at low star formation levels.

Can these effects cause systematic errors in the SFRs? Pflamm-Altenburg et al. (2007, 2009) have investigated the effect of an IGIMF (§2.5) on SFR tracers, and shown that the systematic depletion of massive stars in low-SFR environments could cause H $\alpha$  to substantially underestimate the actual SFR. Interestingly a systematic deficit of H $\alpha$  emission in dwarf galaxies with low SFRs and in low SFR density regions is observed (Sullivan et al. 2000; Bell & Kennicutt 2001; Lee et al. 2009a; Meurer et al. 2009). Recent work suggests however that the systematic dependence of the H $\alpha$ /UV ratio may be produced instead by temporal variations in SFRs, without having to resort to modifying the IMF itself (Fumagalli et al. 2011; Weisz et al. 2012).

### 3.4. Infrared Emission: The Impact of Spitzer and Herschel

Interstellar dust absorbs approximately half the starlight in the universe and re-emits it in the infrared, so measurements in the IR are essential for deriving a complete inventory of star formation. This section focusses on the transformational results which have come from the Spitzer Space Telescope (Werner et al. 2004) and the Herschel Space Observatory (Pilbratt et al. 2010). A re-

view in this journal of extragalactic science from Spitzer can be found in Soifer et al. (2008).

Three other space missions are beginning to influence this subject: the *AKARI* mission (Murakami et al. 2007), the *Wide-field Infrared Survey Explorer* (WISE) mission (Wright et al. 2010), and the *Planck* mission (Planck Collaboration et al. 2011a). These observatories conducted all-sky surveys, with *AKARI* imaging in the  $2.4 - 160 \mu\text{m}$  region, WISE in the range of  $3.4 - 22 \mu\text{m}$ , and *Planck* at  $350 - 850 \mu\text{m}$  (with several bands extending to longer wavelengths). Much of the science from these missions is just beginning to emerge, but they will provide very important results in this subject in the coming decade.

While early applications of dust-based SFR measurements effectively (and necessarily) assumed a one-component dust model, subsequent observations show that the dust emission is comprised of distinct components, each with different spatial distributions and couplings to the young stars. At wavelengths of  $\sim 5 - 20 \mu\text{m}$ , the emission is dominated by molecular bands arising from polycyclic aromatic hydrocarbons (PAHs). Longward of  $\lambda \sim 20 \mu\text{m}$ , the emission is dominated by thermal continuum emission from the main dust grain population. Emission from small grains transiently heated by intense radiation fields (usually in or near star-forming regions) is important out to about  $60 \mu\text{m}$ , whereas at longer wavelengths, emission from larger grains with steady state temperatures dominates (Draine 2003).

The distribution of these different emission components is illustrated in Figure 2, which shows Spitzer and Herschel images of the nearby star-forming galaxy, NGC 6946, at wavelengths ranging from  $3.6 - 500 \mu\text{m}$ . At  $24 \mu\text{m}$ , the emission peaks around the youngest star-forming regions and H II regions, with a more diffuse component extending between these regions. As one progresses to longer wavelengths, the prominence of the diffuse component increases. Recent measurements with Herschel show that this is mainly a physical change, and not an artifact of lower spatial resolution at longer wavelengths (Boquien et al. 2011). This diffuse emission is analogous to the “infrared cirrus” emission observed in our own Galaxy. Interestingly PAH emission appears to correlate the most strongly with the longer-wavelength component of the thermal dust emission (e.g., Bendo et al. 2008), though it often also appears as resolved shells around the young star-forming regions (Helou et al. 2004).

These variations in the morphologies in the different dust emission components translate into considerable variations in the dust SEDs within and between galaxies (e.g., Dale & Helou 2002; Dale et al. 2005; Smith et al. 2007), and as a consequence the conversion of infrared luminosities into SFRs must change for different IR wavelengths. Most early applications of the dust emission as a SFR tracer were based on the integrated total-infrared (TIR) emission. This parameter has the physical advantage of effectively representing the bolometric luminosity of a completely dust-enshrouded stellar population. The TIR-based SFR calibration derived in K98, applicable in the limits of complete dust obscuration and dust heating fully dominated by young stars, is still in widespread use today. For most galaxies however this complete wavelength coverage will not be available, so many workers have calibrated monochromatic SFR in-

dices, usually tuned to one of the Spitzer or Herschel bands, including  $24 \mu\text{m}$  (e.g., Wu et al. 2005a; Alonso-Herrero et al. 2006; Calzetti et al. 2007; Relaño et al. 2007; Rieke et al. 2009, and references therein), and  $70$  and  $160 \mu\text{m}$  (Calzetti et al. 2010a). The latter paper contains an excellent discussion comparing the various calibrations in the literature at the time.

As with all of the SFR indicators, the dust emission is subject to important systematic effects. Just as the UV and visible tracers miss radiation that has been attenuated by dust, the infrared emission misses the starlight that is *not* absorbed by dust (e.g., Hirashita et al. 2001). As discussed earlier, dust attenuates only about half of the integrated starlight of galaxies on average, so the infrared emission will systematically underestimate the SFR if the missing fraction of star formation is not incorporated into the calibrations. This “missing” unattenuated component varies from essentially zero in dusty starburst galaxies to nearly 100% in dust-poor dwarf galaxies and metal-poor regions of more massive galaxies. Another major systematic error works in the opposite direction; in most galaxies, evolved stars (e.g., ages above  $\sim 100 - 200$  Myr) contribute significantly to the dust heating, which tends to cause the IR luminosity to overestimate the SFR. The fraction of dust heating from young stars varies by a large factor among galaxies; in extreme circumnuclear starburst galaxies or individual star-forming regions, nearly all of the dust heating arises from young stars, whereas in evolved galaxies with low specific SFRs, the fraction can be as low as  $\sim 10\%$  (e.g., Sauvage & Thuan 1992; Walterbos & Greenawalt 1996; Cortese et al. 2008). In practical terms this means that the conversion factor from dust luminosity to SFR—even in the limit of complete dust obscuration—is not fixed, but rather changes as a function of the stellar population mix in galaxies. The difference in conversion factor between starbursts and quiescent galaxies with constant SFR, for example, is about a factor of 1.3–2 (e.g., Sauvage & Thuan 1992; Kennicutt et al. 2009; Hao et al. 2011).

The calibration of the mid-IR PAH emission as a quantitative SFR tracer deserves special mention. This index is of particular interest for studies of galaxies at high redshift, because the observed-frame  $24 \mu\text{m}$  fluxes of galaxies at  $z = 1 - 3$  tend to be dominated by redshifted PAH emission. A number of studies have shown that the PAH luminosity scales relatively well with the SFR in metal-rich luminous star-forming galaxies (e.g., Roussel et al. 2001; Peeters et al. 2004; Förster Schreiber et al. 2004; Wu et al. 2005a; Farrah et al. 2007; Calzetti et al. 2007), but the PAH bands weaken dramatically below metal abundances of approximately  $1/4$  to  $1/3 Z_{\odot}$  (e.g., Madden 2000; Engelbracht et al. 2005; Calzetti et al. 2007; Smith et al. 2007), rendering them problematic as quantitative SFR tracers in this regime.

The best way to overcome these systematic biases is to combine the IR measurements with UV or visible-wavelength SFR tracers, to measure the unattenuated starlight directly and to constrain the dust-heating stellar population (§3.7). However, in cases where only IR observations are available one can attempt to incorporate corrections for these effects into the SFR calibrations themselves, and this approach has been taken by most authors (e.g., Calzetti et al. 2010b and references

therein). Fortunately, for most galaxies with moderate to high specific SFRs, the effects of partial dust attenuation and cirrus dust heating by evolved stars appear to roughly compensate for each other. For example, Kewley et al. (2002) showed that for a sample of spiral galaxies with integrated emission-line spectra, the TIR-based calibration of K98 for dusty starburst galaxies was in good agreement with SFRs based on attenuation-corrected H $\alpha$  line fluxes. However, one must avoid applying these IR-based recipes in environments where they are bound to fail, for example, in low-metallicity and other largely dust-free galaxies or in galaxies with low specific SFRs and a strong radiation field from more evolved stars.

### 3.5. Radio Continuum Emission

The centimeter-wavelength radio continuum emission of galaxies consists of a relatively flat-spectrum, free-free component, which scales with the ionizing luminosity (subject to a weak electron temperature dependence) and a steeper spectrum synchrotron component, which overwhelmingly dominates the integrated radio emission at  $\nu \leq 5$  GHz. The free-free component can be separated with multi-frequency radio measurements or high-frequency data (e.g., Israel & van der Hulst 1983; Niklas et al. 1997; Murphy et al. 2011), to provide a photoionization-based measure of the SFR, without the complications of dust attenuation which are encountered with the Balmer lines.

At lower frequencies the integrated emission is dominated by the synchrotron emission from charged particles produced by supernovae. A SFR calibration has not been derived from first principles, but observations have repeatedly confirmed a tight correlation between this non-thermal emission and the far-infrared emission of galaxies, which favors its application as a SFR tracer (e.g., Helou et al. 1985; Condon 1992). Moreover, improvements to receiver technology with the Expanded Very Large Array (EVLA) and other instruments have made the radio continuum a primary means of identifying star-forming galaxies at high redshift and estimating their SFRs. As a result it is appropriate to include it in this discussion of SFR tracers.

Current calibrations of the radio continuum versus SFR relation are bootstrapped from the far-infrared calibrations, using the tight radio-IR correlation. The steep synchrotron spectrum makes this calibration strongly wavelength dependent, and most are referenced to 1.4 GHz (e.g., Yun et al. 2001; Condon 1992; Bell 2003). The calibration adopted here in §3.8 is derived in similar fashion, but adapted to the Kroupa IMFs.

As described above, the IR-based SFR calibrations break down severely in faint galaxies with low dust contents, yet the radio-IR correlation remains tight and nearly linear over the entire luminosity range. How can this arise? The likely explanation can be found in Bell (2003) and references therein, where it is shown that the decrease in dust opacity in low-mass galaxies is accompanied by a decline in synchrotron emission relative to other tracers of the SFR. This is seen most directly as a decline in the ratio of non-thermal radio emission (still dominant in the 1–5 GHz region) to the free-free thermal radio emission. Since the thermal radio emission is directly coupled to the stellar ionization rate and SFR, the relative decline in synchrotron luminosity must re-

flect a physical decline per unit SFR. If correct then the continuity of the radio-IR relation to low luminosities is the result of a “cosmic conspiracy” (Bell 2003), and one should beware of applying the method in galaxies fainter than  $\sim 0.1 L^*$ .

### 3.6. X-ray Emission

Over the past decade, the integrated hard X-ray emission of galaxies has been increasingly applied as a SFR tracer. The component of X-ray emission that does not arise from AGN accretion disks is dominated by massive X-ray binaries, supernovae and supernova remnants, and massive stars, all associated with young stellar populations and recent star formation. Furthermore the observed 2–10 keV fluxes of galaxies are observed to be strongly correlated with their infrared and non-thermal radio continuum fluxes (e.g., Bauer et al. 2002; Ranalli et al. 2003; Symeonidis et al. 2011), strengthening the link to the SFR.

Since there is no way to calibrate the relation between X-ray luminosity and SFR from first principles, the calibration is usually bootstrapped from the infrared or radio. Ranalli et al. (2003) derived such a calibration for integrated 2–10 keV X-ray luminosities, referenced to the K98 calibrations and IMF, and this relation is still widely applied today. Persic et al. (2004) derived an alternate calibration in terms of the hard X-ray binary luminosity alone, which is useful for nearby resolved galaxies. Calibrations of the SFR in terms of X-ray luminosity and stellar mass have been published by Colbert et al. (2004) and Lehmer et al. (2010). For simplicity, we have listed in Table 1 the widely-applied relation of Ranalli et al. (2003), but adjusted to the Kroupa IMF used for the other calibrations.

### 3.7. Composite Multi-Wavelength Tracers

Large multi-wavelength surveys of galaxies allow tests and calibrations of SFR indices that combine information from more than one tracer and exploit the complementary strengths of different wavelengths. Currently this capability is mainly limited to nearby galaxies, but with the expansion of far-infrared to millimeter surveys of high-redshift galaxies, opportunities to apply multi-wavelength diagnostics to distant galaxies should expand in the coming decade (e.g., Overzier et al. 2011; Reddy et al. 2012).

The most widely explored of these methods have combined UV (usually FUV) observations with infrared measurements to construct dust-corrected SFRs, using an approximate energy-balancing approach. In its simplest form one can use a linear combination of UV and IR luminosities to correct the UV fluxes for dust attenuation:

$$L_{\text{UV}}(\text{corr}) = L_{\text{UV}}(\text{observed}) + \eta L_{\text{IR}} \quad (10)$$

where the luminosities are usually calculated from flux densities using the definition  $L = \nu L_\nu$ , and the coefficient  $\eta$  is dependent on the bandpasses chosen for the UV and IR measurements. The most common form of this correction uses GALEX FUV (155 nm) and total-infrared luminosities, hence:

$$L_{\text{FUV}}(\text{corr}) = L_{\text{FUV}}(\text{observed}) + \eta L_{\text{TIR}} \quad (11)$$

Other prescriptions sometimes adopt a higher order polynomial dependence on  $L_{\text{IR}}$  (e.g., Buat et al. 2005), but for brevity we only discuss the linear combinations here. In most cases,  $\eta < 1$ , because only part of the dust-heating radiation is contained in the FUV band, and in many galaxies there is significant dust heating and TIR emission arising from stars other than the UV-emitting population (IR cirrus). The coefficient  $\eta$  can be calibrated theoretically using evolutionary synthesis models, or empirically, using independent measurements of dust-corrected SFRs (e.g., Treyer et al. 2010; Hao et al. 2011).

Early applications of this method were largely restricted to luminous starburst galaxies and star-forming regions, for which UV and IR data could be obtained prior to the advent of GALEX, Spitzer, and Herschel (e.g., Buat et al. 1999; Meurer et al. 1999; Gordon et al. 2000), yielding values of  $\eta \sim 0.6$ . Subsequent analyses extending to normal star-forming galaxies (e.g., Hirashita et al. 2003; Kong et al. 2004; Burgarella et al. 2005; Buat et al. 2005; Treyer et al. 2010; Hao et al. 2011) typically produce values of  $\eta$  which are somewhat lower (e.g., 0.46 for Hao et al. 2011), which almost certainly reflects the larger contribution to dust heating from starlight longward of the FUV. Considering the wide differences in dust heating populations between starburst and normal galaxies, however, this difference of  $\sim 30\%$  is hardly crippling, especially when it reduces dramatically the much larger systematic errors from UV or IR-based SFRs alone.

A similar energy-balancing approach has been applied to derive dust-corrected emission-line luminosities of galaxies (Calzetti et al. 2007; Zhu et al. 2008; Kennicutt et al. 2009; Treyer et al. 2010). Here the equivalent parameter to  $\eta$  above is calibrated using independent estimates of the  $\text{H}\alpha$  attenuation, usually the recombination line decrement as measured from the  $\text{Pa}\alpha/\text{H}\alpha$  or  $\text{H}\alpha/\text{H}\beta$  ratio. Kennicutt et al. (2009) have shown that this approach can be more broadly applied to estimate attenuation corrections for other emission lines (e.g.,  $[\text{O II}]$ ), and it can be calibrated using TIR fluxes, single-band IR fluxes, or even 1.4 GHz radio continuum fluxes. An illustration of the effectiveness of the method is shown in Figure 3, taken from Kennicutt et al. (2009). The top panel shows the consistency between an IR-based tracer ( $24\mu\text{m}$  luminosity) used alone and the dust-corrected  $\text{H}\alpha$  luminosity (via the integrated Balmer decrement). There is a general correlation but considerable scatter and a pronounced non-linearity, which reflects a general correlation of average dust attenuation with the SFR itself. The lower panel plots the best fitting linear combination of  $\text{H}\alpha$  and IR (in this case  $24\mu\text{m}$ ) luminosities against the Balmer-decrement-corrected  $\text{H}\alpha$  luminosities. The scatter between the tracers now is reduced severalfold, and the non-linearity in the comparison with IR luminosities alone is essentially removed.

These composite SFR indicators are not without systematic uncertainties of their own. Questions remain about the systematic reliability of the independent attenuation calibrations (in particular with the effects of dust geometry on the Balmer decrements), and most of the recipes still retain a dependence on stellar population age, via the infrared term; for example the best fitting values of  $\eta$  for H II regions and young starbursts differ from those of normal star forming galaxies by a factor

of  $\sim 1.5$ , consistent with expectations from evolutionary synthesis models, as discussed in §3.8 (Kennicutt et al. 2009). Nevertheless they represent a major improvement over single-wavelength tracers, and provide a valuable testing ground for calibrating and exploring the uncertainties in the monochromatic indicators (e.g., Calzetti et al. 2010b).

Table 2 lists examples of dust attenuation corrections using combinations of FUV and  $\text{H}\alpha$  fluxes with various infrared and radio tracers, taken from Hao et al. (2011) and Kennicutt et al. (2009), respectively. These can be applied in combination with the monochromatic SFR zeropoint calibrations listed in Table 1 (§3.8) to derive dust-corrected SFR measurements.

### 3.8. An Updated Compendium of Integrated SFR Calibrations

K98 presented calibrations for SFRs derived from UV continuum, TIR,  $\text{H}\alpha$  emission-line, and  $[\text{O II}]$  emission-line luminosities, which have come into common usage in the field. The considerable expansion of the subject to other wavelengths and SFR diagnostics since that time motivates a revisit of these calibrations.

Nearly all of these calibrations are based on evolutionary synthesis models, in which the emergent SEDs are derived for synthetic stellar populations with a prescribed age mix, chemical composition, and IMF. The K98 calibrations employed a mix of models from the literature, and assumed a single power-law IMF (Salpeter 1955), with mass limits of 0.1 and  $100 M_{\odot}$ . This IMF gave satisfactory SFR calibrations relative to that of more realistic IMFs for  $\text{H}\alpha$ , but for other wavelengths, the relative calibrations using different tracers are sensitive to the precise form of the IMF. Today most workers calibrate SFR tracers using a modern IMF with a turnover below  $\sim 1 M_{\odot}$ , for example the IMF of Kroupa & Weidner (2003), with a Salpeter slope ( $\alpha_* = -2.35$ ) from  $1\text{--}100 M_{\odot}$  and  $\alpha_* = -1.3$  for  $0.1\text{--}1 M_{\odot}$ . The calibrations presented here use this IMF, but the IMF fit from Chabrier (2003) yields nearly identical results (e.g., Chomiuk & Povich 2011). The past decade has also seen major improvements in the stellar evolution and atmospheric models which are used to generate the synthetic SEDs. The results cited here use the Starburst99 models of Leitherer et al. (1999), which are regularly updated in the on-line version of the package.

Table 1 presents in compact form calibrations for a suite of SFR tracers in the form:

$$\log \dot{M}_* (M_{\odot} \text{ yr}^{-1}) = \log L_x - \log C_x \quad (12)$$

The table lists for each tracer the units of luminosity ( $L_x$ ), the logarithmic SFR calibration constant  $C_x$ , and the primary reference(s) for the calibration. For methods presented in K98, we also list the scaling constant between the new (Kroupa IMF, SB99 model) SFRs and those from K98. As in K98, the recipes for infrared dust emission are in the limit of complete dust attenuation and continuous star formation over a period of 0–100 Myr, which is appropriate for a typical dust-obscured starburst galaxy. *Virtually all of the SFR calibrations presented in Table 1 are taken from the literature, and we strongly encourage users of these calibrations to cite the primary sources, whether or not they choose to cite*

*this paper as well.*

The second column of Table 1 lists the approximate age sensitivity of the different star formation tracers. These were estimated using the Starburst99 models in the approximation of constant star formation. The second number lists the mean stellar age producing the relevant emission, while the third column lists the age below which 90% of the relevant emission is produced. For the dust emission in the infrared these ages can only be estimated, because they depend on the detailed star formation history over periods of up to 100 Myr and longer, and they are also convolved with the level of dust attenuation as a function of stellar age. The numbers are given for the assumed starburst timescales above; for normal galaxies the 90th percentile age can be 500 Myr or longer.

All of the results were calculated for solar metal abundances, and readers should beware that all of the calibrations are sensitive to metallicity. These have been estimated by several authors using evolutionary synthesis models (e.g., Smith et al. 2002; Raiter et al. 2010), but the precise dependences are sensitive to the details of the input stellar models, in particular how effects of stellar rotation are modelled. The models cited above (which do not adopt a dependence of rotation on metallicity) show that a decrease in metal abundance by a factor of ten increases the FUV luminosity of a fixed mass and IMF population by  $\sim 0.07 \pm 0.03$  dex (for the IMFs assumed here), while the ionizing luminosity is more sensitive, increasing by  $\sim 0.4 \pm 0.1$  dex for a tenfold decrease in  $Z/Z_{\odot}$ . The change in infrared luminosities for completely obscured regions should roughly track that for the FUV luminosity, but in most low-metallicity environments, the dust opacity will be severely reduced, producing a sharp fall in infrared emission for a given SFR.

### 3.9. The Challenge of Spatially-Resolved Star Formation Rates in Galaxies

Nearly all of the diagnostic methods described up to now have been designed for measuring integrated SFRs of galaxies or for regions such as starbursts, containing thousands (or more) of massive stars. The resulting SFR prescriptions implicitly assume that local variations in stellar age mix, IMF population, and gas/dust geometry largely average out when the integrated emission of a galaxy is measured.

With the advent of high-resolution maps of galaxies in the UV, IR, emission lines, and radio (and integral-field spectroscopic maps in the visible and near-infrared), one would like of course to extend these diagnostic methods to create fully-sampled spatially-resolved “SFR maps” of galaxies. This extrapolation to much smaller regions within galaxies (or to galaxies with extremely low SFRs), however, is not at all straightforward. At smaller linear scales, nearly all of the statistical approximations cited above begin to break down.

First, when the SFR in the region studied drops below  $\sim 0.001\text{--}0.01 M_{\odot} \text{ yr}^{-1}$  (depending on the SFR tracer used), incomplete sampling of the stellar IMF will lead to large fluctuations in the tracer luminosity for a fixed SFR. These begin to become problematic for luminosities of order  $10^{38} - 10^{39} \text{ erg s}^{-1}$  for emission-line, UV, or IR tracers, and they are especially severe for the ionized gas tracers, which are most sensitive to the uppermost parts of the stellar IMF. For actively star forming normal

disk galaxies, this onset of stochasticity typically occurs on spatial scales of order 0.1–1 kpc, but the region can be considerably larger in galaxies, or parts of galaxies, with lower SFRs. Note that this breakdown on local scales occurs regardless of whether the IMF itself varies systematically.

As a prime example of this stochasticity, consider what astronomers in M51 would observe if they examined the solar neighborhood in the Milky Way from a distance of 10 Mpc. In a pixel of 100 pc radius centered on the Sun they would observe no molecular gas and no star formation. If they degraded their resolution to a radius of 300 pc, they would pick up all the Gould Belt clouds, but no localized H $\alpha$  emission. Within a slightly larger radius of 500 pc, their beam would include Orion, with its O stars and H II region. (For this example, we consider only the stars and emission from the Orion Nebula Cluster (ONC) stars and emission, for which we have good numbers, not the full Orion clouds and OB associations.) This roughly doubles the number of YSOs. Our M51 observers would measure  $\Sigma_{mol} = 0.11 M_{\odot} \text{ pc}^{-2}$ , but if they applied the relation between SFR and H $\alpha$  luminosity from K98, they would derive  $\Sigma(\text{SFR})$  a factor of 10 lower than the actual SFR in Orion, based on the actual stellar content of the ONC and a relatively long timescale of 3 Myr (Chomiuk & Povich 2011), and they would miss the total SFR within 500 pc by a factor of 20 because the other clouds produce no O stars. This severe underestimate for Orion itself from H $\alpha$  emission results because the Orion cluster is too small to fully populate the IMF; its earliest spectral type is O7 V, and so the star cluster produces relatively little ionizing luminosity relative to its total mass and SFR. If the distant observers used the total infrared emission of Orion instead, they would still underestimate its SFR by a factor of 8 (Lada et al. 2012) (a factor of 10 with the newer conversions in Table 1).

Secondly, when the spatial resolution of the SFR measurements encompass single young clusters, such as Orion, the assumption of continuous star formation which is embedded in the global SFR recipes breaks down severely. In such regions that emission at all wavelengths will be dominated by a very young population with ages of typically a few Myr, which will be shorter than the averaging times assumed for all but the emission-line tracers. These changes affect both the relative luminosities of star formation tracers in different bands and of course the interpretation of the “star formation rate” itself. Technically speaking the luminosities of young star-forming clusters only provide information on the masses of the regions studied, and converting these to SFRs requires independent information on the ages and/or age spreads of the stars in the region.

A third measuring bias will set in if the resolution of the measurements becomes smaller than the Strömgren diameters of H II regions or the corresponding dust emission nebulae, which tend to match or exceed those of the H II regions (e.g., Watson et al. 2008; Prescott et al. 2007). This scale varies from  $<100$  pc in the Milky Way to 200–500 pc in actively star-forming galaxies such as NGC 6946 (Figure 2). On these small scales indirect tracers of the SFR (e.g., H $\alpha$ , IR) tend to trace the surfaces and bubbles of clouds rather than the young stars. By

the same token, much of the  $H\alpha$  and dust emission in galaxies, typically 30–60%, is emitted by diffuse ionized gas and dust located hundreds of parsecs or more from any young stars (e.g., Oey et al. 2007; Dale et al. 2007). Such emission produces a false positive signal of star formation, and care is needed to account for its effects when mapping the SFR within galaxies.

Taken together, these factors complicate, but do not prevent, the construction of 2D maps of SFRs, so long as the methodology is adapted to the astrophysical application. For example, radial profiles of SFR distributions in galaxies may still be reliably derived using the integrated SFR calibrations, providing that large enough annuli are used to assure that the IMF is fully populated in aggregate, and the SFR is regarded to be averaged over time scales of order 100 Myr. Likewise a 2D distribution of star formation over the last 5 Myr or so can be derived from a short-lived tracer such as  $H\alpha$  emission, if the spatial coverage is limited to very young regions, and structure on scales smaller than individual H II regions is ignored. Maps of integrated  $H\alpha$  and IR emission can be used to study the population of star-forming regions and the star formation law, when restricted to young regions where the physical association of gas and stars is secure (§6.4). An alternative approach is to apply direct stellar photospheric tracers, such as the ultraviolet continuum emission on large scales (bearing in mind the variable 10–300 Myr time scales traced by the UV), or resolved stellar tracers such as YSOs or deep visible-wavelength color-magnitude diagrams, to map the distributions of young stars directly (§3.1). Likewise it should be possible to use pixel-resolved SEDs of galaxies in the UV–visible to derive dust-corrected UV maps, and possibly apply local corrections for age in the maps. With such a multiplicity of approaches, we anticipate major progress in this area, which will be invaluable for understanding in detail the patterns of star formation in galaxies and connecting to detailed studies within the MW.

#### 4. THE LOCAL PERSPECTIVE: FROM THE INSIDE LOOKING OUT

##### 4.1. Outline of low-mass star formation

The formation of low-mass stars can be studied in greatest detail because it occurs in relatively nearby clouds and sometimes in isolation from other forming stars. The established paradigm provides a point of comparison for more massive, distant, and clustered star formation.

Physically, an individual star forming event, which may produce a single star or a small number multiple system, proceeds from a prestellar core, which is a gravitationally bound starless core (see §2.2, di Francesco et al. 2007 for definitions), a dense region, usually within a larger molecular cloud. Prestellar cores are centrally condensed, and can be modeled as Bonnor-Ebert spheres (Ward-Thompson et al. 1999; Evans et al. 2001; Kirk et al. 2005), which have nearly power-law ( $n(r) \propto r^{-2}$ ) envelopes around a core with nearly constant density.

Collapse leads to the formation of a first hydrostatic core in a small region where the dust continuum emission becomes optically thick; this short-lived core is still molecular and grows in mass by continued infall from the outer layers (Larson 1969; Boss & Yorke 1995; Omukai

2007; Stahler & Palla 2005). When the temperature reaches 2000 K, the molecules in the first hydrostatic core collisionally dissociate, leading to a further collapse to the true protostar, still surrounded by the bulk of the core, often referred to as the envelope. Rotation leads to flattening and a centrifugally supported disk (Terebey et al. 1984). Magnetic fields plus rotation lead to winds and jets (Shang et al. 2007; Pudritz et al. 2007), which drive molecular outflows from young stars of essentially all masses (Arce et al. 2007; Wu et al. 2004).

Stage 0 sources have protostars, disks, jets, and envelopes with more mass in the envelope than in the star plus disk (Andre et al. 1993). Stage I sources are similar to Stage 0, but with less mass in the envelope than in star plus disk. Stage II sources lack an envelope, but have a disk, while Stage III sources have little or no disk left. There are several alternative quantitative definitions of the qualitative terms used here (Robitaille et al. 2006; Crapsi et al. 2008).

Stages I through III are usually associated with SED Classes I through III defined by SED slopes rising, falling slowly, and falling more rapidly from 2 to 25  $\mu\text{m}$  (Lada & Wilking 1984). A class intermediate between I and II, with a slope near zero (Flat SED) was added by Greene et al. (1994). In fact, orientation effects in the earlier stages can confuse the connection between class and stage; without detailed studies of each source, one cannot observationally determine the stage without ambiguity. For this reason, most of the subsequent discussion will use classes despite their questionable correspondence to physical configurations. Evans et al. (2009) give a historical account of the development of the class and stage nomenclature.

For our present purposes, the main point is to establish time scales for the changing observational signatures, so the classes are useful. Using the boundaries between classes from Greene et al. (1994), Evans et al. (2009) found that the combined Class 0/I phases last  $\sim 0.5$  Myr, with a similar duration for Flat SEDs, assuming a continuous flow through the classes for at least the Class II duration of  $2 \pm 1$  Myr (e.g., Mamajek 2009), which is essentially the age when about half the stars in a dated cluster lack infrared excesses; hence all durations can be thought of as half-lives.

To summarize, we would expect a single star-forming core to be dominated by emission at far-infrared and sub-millimeter wavelengths for about 0.5 Myr, near-infrared and mid-infrared radiation for about 1.5 Myr and near-infrared to visible light thereafter. However, the duration of emission at longer wavelengths can be substantially lengthened by material in surrounding clumps or clouds not directly associated with the forming star.

The star formation rates and efficiencies can be calculated for a set of 20 nearby clouds ( $\langle d \rangle = 275$  pc) with uniform data from *Spitzer*. The star formation rate was calculated from equation 9 and the assumptions in §3.1 by Heiderman et al. (2010), who found a wide range of values for  $\dot{M}_*$ , with a mean value for the 20 clouds of  $\dot{M}_* = 39 \pm 18 M_\odot \text{ Myr}^{-1}$ . The star formation efficiency ( $\epsilon = M_*/(M_* + M_{\text{gas}})$ ) can only be calculated over the last 2 Myr because surveys are incomplete at larger ages; averaging over all 20 clouds, only 2.6% of the cloud mass has turned into YSOs in that period and  $\langle \Sigma(\text{SFR}) \rangle = 1.2$



$M_{\odot} \text{ yr}^{-1} \text{ kpc}^{-2}$  (Heiderman et al. 2010). For individual clouds,  $\epsilon$  ranges from 2% to 8% (Evans et al. 2009; Peterson et al. 2011). The final efficiency will depend on how long the cloud continues to form stars before being disrupted; cloud lifetimes are poorly constrained (McKee & Ostriker 2007; Bergin & Tafalla 2007), and they may differ for clouds where massive stars form.

For comparison to extragalactic usage, the mean  $t_{\text{dep}} = 1/\epsilon'$  (§1.2) is about 82 Myr for seven local clouds, longer than most estimates of cloud lifetime, and much longer than either  $\langle t_{\text{ff}} \rangle$  (1.4 Myr) or  $\langle t_{\text{cross}} \rangle$  (5.5 Myr) (Evans et al. 2009). The  $\langle t_{\text{dep}} \rangle$  for local clouds is, on the other hand, about 10% of the  $t_{\text{dep}}$  for the MW molecular gas as a whole (§5.1).

#### 4.2. Formation of Clusters and High-mass Stars

The study of young clusters provides some distinct opportunities. By averaging over many stars, a characteristic age can be assigned, with perhaps more reliability than can be achieved for a single star. As noted (§4.1), the set point for ages of all SED classes is determined by the fraction of mid-infrared excesses in clusters. This approach does implicitly assume that the cluster forms “coevally”, by which one really means that the spread in times of formation is small compared to the age of the cluster. Because objects ranging from prestellar cores to Class III objects often coexist (Rebull et al. 2007), this assumption is of dubious reliability for clusters with ages less than about 5 Myr, exactly the ones used to set the timescales for earlier classes. Note also that assuming coeval formation in this sense directly contradicts the assumption of continuous flow through the classes. We live with these contradictions.

Most nearby clusters do not sample very far up the IMF. The nearest young cluster that has formed O stars is 415–430 pc away in Orion (Menten et al. 2007; Hirota et al. 2007), and most lie at much larger distances, making study of the entire IMF difficult.

Theoretically, the birthplace of a cluster is a clump (Williams et al. 2000). The clumps identified by  $^{13}\text{CO}$  maps in nearby clouds are dubious candidates for the reasons given in §2.5. The structures identified by Kainulainen et al. (2009) in the power-law tail of the probability distribution function are better candidates, but most are still unbound. Objects found in some surveys of dust continuum emission (§2.3) appear to be still better candidates. For example, analysis (Schlingman et al. 2011; Dunham et al. 2011b) of the sources found in millimeter-wave continuum emission surveys of the MW (§2.3) indicates typical volume densities of a few  $\times 10^3 \text{ cm}^{-3}$ , compared to about  $200 \text{ cm}^{-3}$  for  $^{13}\text{CO}$  structures. Mean surface densities are about  $180 M_{\odot} \text{ pc}^{-2}$ , higher than those of gas in the power-law tail ( $\Sigma_{\text{gas}} \sim 40 - 80 M_{\odot} \text{ pc}^{-2}$ ). These structures have a wide range of sizes, with a median of 0.75 to 1 pc.

Studies of regions with signposts of massive star formation, using tracers requiring higher densities (e.g., Plume et al. 1992; Beuther et al. 2002) or millimeter continuum emission from dust (e.g., Beuther et al. 2002; Mueller et al. 2002) have identified slightly smaller structures ( $r \sim 0.5 \text{ pc}$ ) that are much denser, indeed denser on average than cores in nearby clouds. In addition to having a mass distribution consistent with that of clus-

ters (§2.5), many have far-infrared luminosities consistent with the formation of clusters of stars with masses ranging up to those of O stars. The properties of the Plume et al. (1992) sample have been studied in a series of papers (Plume et al. 1997; Mueller et al. 2002; Shirley et al. 2003), with the most recent summary in Wu et al. (2010a). The properties of the clumps depend on the tracer used. Since the HCN  $J = 1 \rightarrow 0$  line is used in many extragalactic studies, we will give the properties as measured in that line. The mean and median FWHM are 1.13 and 0.71 pc; the mean and median infrared luminosities are  $4.7 \times 10^5$  and  $1.06 \times 10^5 L_{\odot}$ ; the mean and median virial mass are 5300 and 2700  $M_{\odot}$ ; the mean and median surface densities are 0.29 and 0.28  $\text{gm cm}^{-2}$ ; and the mean and median of the average volume densities ( $n$ ) are  $3.2 \times 10^4$  and  $1.6 \times 10^4 \text{ cm}^{-3}$ . As lines tracing higher densities are used, the sizes and masses decrease, while the surface densities and volume densities increase, as expected for centrally condensed regions. Very similar results were obtained from studies of millimeter continuum emission from dust (Faúndez et al. 2004) toward a sample of southern hemisphere sources surveyed in CS  $J = 2 \rightarrow 1$  (Bronfman et al. 1996).

Embedded clusters provide important testing grounds for theories of star formation. Using criteria of 35 members with a stellar density of  $1 M_{\odot} \text{ pc}^{-3}$  for a cluster, Lada & Lada (2003) argue that most stars form in clusters, and 90% of those are in rich clusters with more than 100 stars, but that almost all clusters ( $> 93\%$ ) dissipate as the gas is removed, a process they call “infant mortality.” With more complete surveys enabled by Spitzer, the distributions of numbers of stars in clusters and stellar densities are being clarified. Allen et al. (2007) found that about 60% of young stars within 1 kpc of the Sun are in clusters with more than 100 members, but this number is heavily dominated by the Orion Nebula cluster. Drawing on the samples from Spitzer surveys of nearly all clouds within 0.5 kpc, Bressert et al. (2010) found a continuous distribution of surface densities and no evidence for a bimodal distribution, with distinct “clustered” and “distributed” modes. They found that the fraction of stars that form in clusters ranged from 0.4 to 0.9, depending on which definition of “clustered” was used. Even regions of low-mass star formation, often described as distributed star formation, are quite clustered and the youngest objects (Class I and Flat SED sources, see §4.1) are very strongly concentrated to regions of high extinction, especially after the samples have been culled of interlopers (Fig. 4, §6.4). Similarly, studies of three clouds found that 75% of prestellar cores lay above thresholds in  $A_V$  of 8, 15, and 20 mag, while most of the cloud mass was at much lower extinction levels (Enoch et al. 2007).

A Spitzer study (Gutermuth et al. 2009) of 2548 YSOs in 39 nearby ( $d < 1.7 \text{ kpc}$ ), previously known (primarily from the compilation by Porras et al. 2003) young clusters, but excluding Orion and NGC2264, found the following median properties: 26 members, core radius of 0.39 pc, stellar surface density of  $60 \text{ pc}^{-2}$ , and embedded in a clump with  $A_K = 0.8 \text{ mag}$ , which corresponds to  $A_V = 7.1 \text{ mag}$ . Translating to mass surface density using  $\langle M_{\star} \rangle = 0.5 M_{\odot}$ , the median stellar mass surface density would be  $30 M_{\odot} \text{ pc}^{-2}$  and the gas surface den-

sity would be  $107 M_{\odot} \text{ pc}^{-2}$ . The distributions are often elongated, with a median aspect ratio of 1.82. The median spacing between YSOs, averaged over all 39 clusters, is  $0.072 \pm 0.006 \text{ pc}$ , comparable to the size of individual cores, and a plausible scale for Jeans fragmentation. The distributions are all skewed toward low values, with a tail to higher values.

While various definitions of “clustered” have been used, one physically meaningful measure is a surface density of  $\sim 200 \text{ YSOs pc}^{-2}$  (Gutermuth et al. 2005), below which individual cores are likely to evolve in relative isolation (i.e., the timescale for infall is less than the timescale for core collisions). With their sample, Bressert et al. (2010) found that only 26% were likely to interact faster than they collapse. However, that statistic did not include the Orion cluster, which exceeds that criterion.

The fact that the Orion cluster dominates the local star formation warns us that our local sample may be unrepresentative of the Galaxy as a whole. Leaving aside globular clusters, there are young clusters that are much more massive than Orion. Portegies Zwart et al. (2010) have cataloged massive ( $M_{\star} \geq 10^4 M_{\odot}$ ), young (age  $\leq 100 \text{ Myr}$ ) clusters (12) and associations (13), but none of these are more distant than the Galactic Center, so they are clearly undercounted. The mean half-light radius of the 12 clusters is  $1.7 \pm 1.3 \text{ pc}$  compared to  $11.2 \pm 6.4 \text{ pc}$  for the associations. For the clusters,  $\langle \log M_{\star}(M_{\odot}) \rangle = 4.2 \pm 0.3$ . Three of the massive dense clumps from the Wu et al. (2010a) study have masses above  $10^4 M_{\odot}$  and are plausible precursors of this class of clusters. Still more massive clusters can be found in other galaxies, and a possible precursor ( $M_{\text{cloud}} > 1 \times 10^5 M_{\odot}$  within a  $2.8 \text{ pc}$  radius) has recently been identified near the center of the MW (Longmore et al. 2012).

The topic of clusters is connected to the topic of massive stars because 70% of O stars reside in young clusters or associations (Gies 1987). Furthermore, most of the field population can be identified as runaways (de Wit et al. 2005), with no more than 4% with no evidence of having formed in a cluster. While there may be exceptions (see Zinnecker & Yorke 2007 for discussion), the vast majority of massive stars form in clusters. The most massive star with a dynamical mass (NGC 3603-A1) weighs in at  $116 \pm 31 M_{\odot}$  and is a 3.77 day binary with a companion at  $89 \pm 16 M_{\odot}$  (Schnurr et al. 2008). Still higher initial masses (105–170  $M_{\odot}$ ) for the stars in NGC3603 and even higher in R136 (165–320  $M_{\odot}$ ) have been suggested (Crowther et al. 2010). Many of the most massive stars exist in tight (orbital periods of a few days) binaries (Zinnecker & Yorke 2007). For a recent update on massive binary properties, see Sana & Evans (2011).

There is some evidence, summarized by Zinnecker & Yorke (2007), that massive stars form only in the most massive molecular clouds, with  $\max(M_{\star}) \propto M_{\text{cloud}}^{0.43}$  suggested by Larson (1982). Roughly speaking, it takes  $M_{\text{cloud}} = 10^5 M_{\odot}$  to make a  $50 M_{\odot}$  star. Recognizing that clumps are the birthplaces of clusters and that efficiencies are not unity could make the formation of massive stars even less likely. The question (§2.5) is whether the absence of massive stars in clumps or clusters of modest total mass is purely a sampling effect (Fumagalli et al. 2011; Calzetti et al. 2010a and references therein) or a causal relation (Weidner & Kroupa 2006). If causal,

differences in the upper mass limit to clouds or clumps (§2.5) in a galaxy could limit the formation of the most massive stars. Larson (1982) concluded that his correlation could be due to sampling. As a concrete example, is the formation of a  $50 M_{\odot}$  star as likely in an ensemble of 100 clouds, each with  $10^3 M_{\odot}$ , as it is in a single  $10^5 M_{\odot}$  cloud? Unbiased surveys of the MW for clumps and massive stars (§5.1) could allow a fresh look at this question, with due regard for the difficulty of distinguishing “very rarely” from “never.”

#### 4.3. Theoretical Aspects

The fundamental problem presented to modern theorists of star formation has been to explain the low efficiency of star formation on the scale of molecular clouds. Early studies of molecular clouds concluded that they were gravitationally bound and should be collapsing at free fall (e.g., Goldreich & Kwan 1974). Zuckerman & Palmer (1974) pointed out that such a picture would produce stars at 30 times the accepted average recent rate of star formation in the Milky Way (§5.1) if stars formed with high efficiency. Furthermore, Zuckerman & Evans (1974) found no observational evidence for large scale collapse and suggested that turbulence, perhaps aided by magnetic fields, prevented overall collapse. This suggestion led eventually to a picture of magnetically subcritical clouds that formed stars only via a redistribution of magnetic flux, commonly referred to as ambipolar diffusion (Shu et al. 1987; Mouschovias 1991), which resulted in cloud lifetimes about 10 times the free-fall time. If, in addition, only 10% of the cloud became supercritical, a factor of 100 decrease in star formation rate could be achieved.

Studies of the Zeeman effect in OH have now provided enough measurements of the line-of-sight strength of the magnetic field to test that picture. While there are still controversies, the data indicate that most clouds (or, more precisely, the parts of clouds with Zeeman measurements) are supercritical or close to critical, but not strongly subcritical (Crutcher et al. 2010). Pictures of static clouds supported by magnetic fields are currently out of fashion (McKee & Ostriker 2007), but magnetic fields are almost certain to play a role in some way (for a current review, see Crutcher 2012, this volume). Simulations of turbulence indicate a fairly rapid decay, even when magnetic fields are included (Stone et al. 1998). As a result, there is growing support for a more dynamical picture in which clouds evolve on a crossing time (Elmegreen 2000). However, this picture must still deal with the Zuckerman-Palmer problem.

There are two main approaches to solving this problem at the level of clouds, and they are essentially extensions of the two original ideas, magnetic fields and turbulence, into larger scales. One approach, exemplified by Vázquez-Semadeni et al. (2011) argues that clouds are formed in colliding flows of the warm, neutral medium. They simulate the outcome of these flows with magnetic fields, but without feedback from star formation. Much of the mass is magnetically subcritical and star formation happens only in the supercritical parts of the cloud. A continued flow of material balances the mass lost to star formation so that the star formation efficiency approaches a steady value, in rough agreement with the observations.

A second picture, exemplified by Dobbs et al. (2011), is that most clouds and most parts of clouds are not gravitationally bound but are transient objects. Their simulations include feedback from star formation, but not magnetic fields. During cloud collisions, material is redistributed, clouds may be shredded, and feedback removes gas. Except for a few very massive clouds, most clouds lose their identity on the timescales of a few Myr. In this picture, the low efficiency simply reflects the fraction of molecular gas that is in bound structures.

It is not straightforward to determine observationally if clouds are bound, especially when they have complex and filamentary boundaries. Heyer et al. (2001) argued that most clouds in the outer galaxy with  $M > 10^4 M_\odot$  were bound, but clumps and clouds with  $M < 10^3 M_\odot$  were often not bound. Heyer et al. (2009) address the issues associated with determining accurate masses for molecular clouds. In a study on the inner Galaxy, Roman-Duval et al. (2010) concluded that 70% of molecular clouds (both in mass and number) were bound.

If molecular clouds are bound and last longer than a few crossing times, feedback or turbulence resulting from feedback is invoked. For low-mass stars, outflows provide the primary feedback (e.g., Li & Nakamura 2006) while high-mass stars add radiation pressure and expanding H II regions (e.g., Murray 2011). In addition, the efficiency is not much higher in most clumps, so the problem persists to scales smaller than that of clouds.

Another longstanding problem of star formation theory has been to explain the IMF (§2.5). This topic has been covered by many reviews, so we emphasize only two aspects. The basic issue is that the typical conditions in star forming regions suggest a characteristic mass, either the Jeans mass or the Bonnor-Ebert mass, around  $1 M_\odot$  (e.g., Bonnell et al. 2007). Recently, Krumholz (2011) has derived a very general expression for a characteristic mass of  $0.15 M_\odot$ , with only a very weak dependence on pressure. However, we see stars down to the hydrogen-burning limit and a continuous distribution of brown dwarfs below that, extending down even to masses lower than those seen in extrasolar planets (Allers et al. 2006). An extraordinarily high density would be required to make such a low mass region unstable.

On the other end, making a star with mass over 100 times the characteristic mass is challenging. Beuther et al. (2007a) provide a nice review of both observations and theory of massive star formation. While dense clumps with mass much greater than  $100 M_\odot$  are seen, they are likely to fragment into smaller cores. Fragmentation can solve the problem of forming low mass objects, but it makes it hard to form massive objects. Simulations of unstable large clumps in fact tend to fragment so strongly as the mean density increases that they overproduce brown dwarfs, but no massive stars (e.g., Klessen et al. 1998; Martel et al. 2006). This effect is caused by the assumed isothermality of the gas, because the Jeans mass is proportional to  $(T_K^3/n)^{0.5}$ . Simulations including radiative feedback, acting on a global scale, have shown that fragmentation can be suppressed and massive stars formed (e.g., Bate 2009; Urban et al. 2010; Krumholz et al. 2010). Krumholz & McKee (2008) have argued that a threshold clump surface density of  $1 \text{ gm cm}^{-2}$  is needed to suppress fragmentation, allowing the

formation of massive stars.

The radiative feedback, acting locally, can in principle also limit the mass of the massive stars through radiation pressure. This can be a serious issue for the formation of massive stars in spherical geometries, but more realistic, aspherical simulations show that the radiation is channeled out along the rotation axis, allowing continued accretion through a disk (Yorke & Sonnhalter 2002; Krumholz et al. 2009a; Kuiper et al. 2011).

The picture discussed so far is basically a scaled-up version of the formation of low mass stars by accretion of material from a single core (sometimes called Core Accretion). An alternative picture, called Competitive Accretion, developed by Klessen et al. (1998), Bate et al. (2003), and Bonnell et al. (2003), builds massive stars from the initial low-mass fragments. The pros and cons of these two models are discussed in a joint paper by the leading protagonists (Krumholz & Bonnell 2009). They agree that the primary distinction between the two is the original location of the matter that winds up in the star: in Core Accretion models, the star gains the bulk of its mass from the local dense core, continuing the connection of the core mass function to the initial stellar mass function to massive stars; in Competitive Accretion models, the more massive stars collect most of their mass from the larger clump by out-competing other, initially low mass, fragments. A hybrid picture, in which a star forms initially from its parent core, but then continues to accrete from the surrounding clump, has been advanced (Myers 2009, 2011), with some observational support (e.g., Longmore et al. 2011).

Observational tests of these ideas are difficult. The Core Accretion model requires that clumps contain a core mass function extending to massive cores. Some observations of massive dense clumps have found substructure on the scale of cores (Beuther et al. 2007b; Brogan et al. 2009), but the most massive cores identified in these works are  $50\text{--}75 M_\odot$ . Discussions in those references illustrate the difficulties in doing this with current capabilities. ALMA will make this kind of study much more viable, but interpretation will always be tricky. The Competitive Accretion model relies on a continuous flow of material to the densest parts of the clump to feed the growing oligarchs. Evidence for overall inward flow in clumps is difficult; evidence for it is found in some surveys (Wu & Evans 2003; Fuller et al. 2005; Reiter et al. 2011a), but not in others (Purcell et al. 2006). Since special conditions are required to produce an inflow signature, the detection rates may underestimate the fraction with inflow. The dense clumps are generally found to be centrally condensed (Beuther et al. 2002; Mueller et al. 2002; van der Tak et al. 2000), which can also suppress over-fragmentation.

Other possible tests include the coherence of outflows in clusters, as these should be distorted by sufficiently rapid motions. The kinematics of stars in forming clusters, which should show more velocity dispersion in the competitive accretion models, provide another test. Astrometric studies are beginning to be able to constrain these motions (Rochau et al. 2010), along with cleaner separation of cluster members from field objects. Relative motions of cores within clumps appear to be very low ( $< 0.1 \text{ /kms}$ ), challenging the Competitive Accretion model (Walsh et al. 2004).

Theoretical studies include evolutionary tracks of pre-main-sequence stars (e.g., Chabrier & Baraffe 2000 for low mass stars and substellar objects). These evolutionary calculations are critical for determining the ages of stars and clusters. For more massive stars, it is essential to include accretion in the evolutionary calculations (Palla & Stahler 1992) and high accretion rates strongly affect the star’s evolution (Zinnecker & Yorke 2007; Hosokawa & Omukai 2009). Assumptions about accretion and initial conditions may also have substantial consequences for the usual methods of determining ages of young stars (Baraffe et al. 2009; Baraffe & Chabrier 2010; Hosokawa et al. 2011).

#### 4.4. Summary Points from the Local Perspective

The main lessons to retain from local studies of star formation as we move to the scale of galaxies are summarized here.

1. Star formation is not distributed smoothly over molecular clouds but is instead highly concentrated into regions of high extinction or mass surface density, plausibly associated with the theoretical idea of a cluster-forming clump. This is particularly apparent when prestellar cores or the youngest protostars are considered (e.g., Figure 4). In contrast, most of the mass in nearby molecular clouds is in regions of lower extinction.
2. By counting YSOs in nearby clouds, one can obtain reasonably accurate measures of star formation rate and efficiency without the uncertainties of extrapolation from the high-mass tail of the IMF. The main source of uncertainty is the ages of YSOs.
3. There is no obvious bimodality between “distributed” and “clustered” star formation, but dense clusters with massive stars tend to form in regions of higher mean density and turbulence, which are centrally condensed. Plausible precursors of quite massive (up to  $10^4$  or perhaps  $10^5 M_\odot$ ) clusters can be found in the MW.
4. Despite much theoretical progress, the challenge of explaining the low efficiency of star formation, even in regions forming only low-mass stars, remains. Similarly, an understanding of the full IMF, from brown dwarfs to the most massive stars, remains elusive.

### 5. THE GALACTIC PERSPECTIVE: FROM THE OUTSIDE LOOKING IN

#### 5.1. The Milky Way as a Star-forming Galaxy

As our nearest example, the Milky Way (hereafter denoted as MW) has obvious advantages in studies of star formation in galaxies. However, living inside the MW presents serious problems of distance determination and selection effects, compared to studies of other galaxies. We can “look in from the outside” only with the aid of models. After reviewing surveys briefly, we consider properties of gas and star formation within the MW, bearing in mind the issues raised in §2.4 and §3, first as a whole, and then the radial distribution, and finally some notes on non-axisymmetric structure.

#### 5.1.1. Surveys

Recent and ongoing surveys of the Galactic Plane at multiple wavelengths are revitalizing the study of the MW as a galaxy. Surveys of H I from both northern (Taylor et al. 2003) and southern (McClure-Griffiths et al. 2005) hemispheres, along with a finer resolution survey of parts of the Galactic Plane (Stil et al. 2006) have given a much clearer picture of the atomic gas in the MW (for a review of H I surveys, see Kalberla & Kerp 2009). Based on these surveys, properties of the cool atomic clouds have been analyzed by Dickey et al. (2003).

Numerous surveys of the MW have been obtained in CO  $J = 1 \rightarrow 0$  (e.g., Dame et al. 2001; Bronfman et al. 1988; Clemens et al. 1988). A survey of the inner part of the MW in  $^{13}\text{CO}$  (Jackson et al. 2006) has helped with some of problems caused by optical depth in the main isotopologue.

Surveys for tracers of star formation have been made in radio continuum (free-free) emission (Altenhoff et al. 1970) and recombination lines (Anderson et al. 2011; Lockman 1989), in water masers (Cesaroni et al. 1988; Walsh et al. 2011), and methanol masers (Pestalozzi et al. 2005; Green et al. 2009). In addition to being signposts of (mostly massive) star formation, the masers provide targets for astrometric studies using VLBI.

Complementary surveys of clouds have been done using mid-infrared extinction (e.g., Perault et al. 1996; Egan et al. 1998; Peretto & Fuller 2009), which can identify Infrared Dark Clouds (IRDCs) against the Galactic background emission. The MIPSGAL survey (Carey et al. 2009) should also provide a catalog of very opaque objects. At longer wavelengths, the dust is usually in emission, and millimeter continuum emission from dust (e.g., Aguirre et al. 2011; Rosolowsky et al. 2010; Schuller et al. 2009) provides a different sample of objects.

Each method has its own selection effects and efforts are ongoing to bring these into a common framework. A key ingredient is to determine the distances, using spectral lines and methods to break the distance ambiguity in the inner galaxy; initial work is underway (Russeil et al. 2011; Schlingman et al. 2011; Dunham et al. 2011b; Foster et al. 2011). Ultimately, these studies should lead to a better definition of the total amount and distribution of dense gas (§1.2). The Herschel HIGAL survey (Molinari et al. 2010) will add wavelengths into the far-infrared and lead to a far more complete picture. Quantities like  $L_{\text{FIR}}/M_{\text{cloud}}$  and  $L_{\text{FIR}}/M_{\text{dense}}$ , as used in extragalactic studies, can be calculated for large samples.

#### 5.1.2. The Milky Way as a Whole

The Milky Way is a barred spiral galaxy (Burton 1988; Dame et al. 2001; Benjamin et al. 2005). The number and position of spiral arms are still topics for debate, but the best currently available data favor a grand-design, two-armed, barred spiral with several secondary arms. A conception of what the MW would look like from the outside (Churchwell et al. 2009) is shown in Figure 5. We can expect continuing improvements in the model of the MW as VLBI astrometry improves distance determinations of star forming regions across the MW (Reid et al. 2009; Brunthaler et al. 2011). As we will be comparing the MW to NGC 6946, we also show images of that galaxy at H $\alpha$ , 24  $\mu\text{m}$ , H I, and CO  $J = 2 \rightarrow 1$  in Fig. 6.

Based on a model including dark matter (Kalberla & Kerp 2009; Kalberla et al. 2007; Kalberla & Dedes 2008), the MW mass within 60 kpc of the center is  $M(\text{tot}) = 4.6 \times 10^{11} M_\odot$ , with  $M(\text{baryon}) = 9.5 \times 10^{10} M_\odot$ . The total mass of atomic gas (H I plus He) is  $M(\text{atomic}) = 8 \times 10^9 M_\odot$ , and the warm ionized medium contains  $M(\text{WIM}) = 2 \times 10^9 M_\odot$ . The mass fraction of the HIM (§2.1) is negligible. With a (perhaps high) estimate for the molecular mass of  $M(\text{mol}) = 2.5 \times 10^9 M_\odot$ , Kalberla & Kerp (2009) derive a gas to baryon ratio of 0.13. As explained in §5.1.3, for consistent comparison to the radial distribution in NGC 6946, we will use a constant  $X(\text{CO}) = 2.0 \times 10^{20}$ , correct for helium, and assume an outer radius of the star forming disk of 13.5 kpc to define masses, surface densities, etc. Within  $R_{\text{gal}} = 13.5$  kpc,  $M(\text{mol}) = 1.6 \times 10^9 M_\odot$  and  $M(\text{atomic}) = 5.0 \times 10^9 M_\odot$  with these conventions.

The volume filling factor of the CNM is about 1% (Cox 2005) and that of molecular clouds, as traced by the  $^{13}\text{CO}$  survey (Roman-Duval et al. 2010), has been estimated at about 0.5% (M. Heyer, personal communication) in the inner galaxy, but much lower overall. Denser ( $n \sim \text{few} \times 10^3 \text{ cm}^{-3}$ ) structures found in millimeter continuum surveys, roughly corresponding to clumps, appear to have a surface filling factor of  $10^{-4}$  and a volume filling factor of about  $10^{-6}$  (M. K. Dunham, personal communication), but better estimates should be available soon.

The star formation rate of the MW has been estimated from counting H II regions, which can be seen across the MW and extrapolating to lower mass stars (Mezger 1987; McKee & Williams 1997; Murray & Rahman 2010). These methods average over the effective lifetime of massive stars, about 3-10 Myr (Table 1). Estimates of  $\dot{M}_*$  from a model of the total far-infrared emission of the MW (e.g., Misiriotis et al. 2006) are somewhat less sensitive to the high end of the IMF (§3) and average over a longer time. An alternative approach, based on counting likely YSOs in the GLIMPSE survey of the Galactic plane (Robitaille & Whitney 2010) is much less biased toward the most massive stars, but is limited by sensitivity, issues of identification of YSOs, and models of extinction. Chomiuk & Povich (2011) have recently reviewed all methods of computing  $\dot{M}_*$  for the MW and conclude that they are consistent with  $\dot{M}_* = 1.9 \pm 0.4 M_\odot \text{ yr}^{-1}$ . However they conclude that resolved star counts give SFRs that are factors of 2-3 times higher (see §6.4 for further discussion).

With a radius of active star formation of 13.5 kpc (§5.1.3),  $\dot{M}_* = 1.9 M_\odot \text{ yr}^{-1}$  yields  $\langle \Sigma(\text{SFR}) \rangle = 3.3 \times 10^{-3} M_\odot \text{ yr}^{-1} \text{ kpc}^{-2}$ . Taking  $M(\text{mol}, R_{\text{gal}} < 13.5) = 1.6 \times 10^9 M_\odot$ ,  $t_{\text{dep}} = 0.8$  Gyr, 10 times longer than  $\langle t_{\text{dep}} \rangle$  in local clouds (§4.1). For all the gas in the (60 kpc) MW,  $t_{\text{dep}} = 6.6$  Gyr, or 5.5 Gyr if the WIM is excluded. If we attribute all non-gaseous baryons in the Kalberla & Kerp (2009) model ( $8.25 \times 10^{10} M_\odot$ ) to stars and stellar remnants, ignore recycling, and take an age of  $1 \times 10^{10}$  yr, we would derive an average star formation rate of  $8.25 M_\odot \text{ yr}^{-1}$ , about 4 times the current rate.

### 5.1.3. Radial Distributions

The MW also offers a wide range of conditions, from the far outer Galaxy to the vicinity of the Galactic Cen-

ter, for detailed study. The hurdle to overcome, especially in the inner MW, is to assign accurate distances. The radial distributions of atomic and molecular gas, along with the star formation rate surface density (here in units of  $M_\odot \text{ Gyr}^{-1} \text{ pc}^{-2}$ ), are plotted in Figure 7, along with a similar plot for NGC 6946 (Schruba et al. 2011). For consistency, we have used the same  $X(\text{CO})$  and correction for helium (for both molecular and atomic gas) as did Schruba et al. (2011). These distributions for the MW have considerable uncertainties, and should be taken with appropriate cautions, especially in the innermost regions, as discussed below. Misiriotis et al. (2006) presents a collection of estimates of  $\Sigma(\text{SFR})$  and a model. They all show a steady decline outward from a peak at  $R_{\text{gal}} \sim 5$  kpc, but the situation in the innermost galaxy is unclear. The data on H II regions that forms the basis of most estimates are very old, and a fresh determination of  $\Sigma(\text{SFR})(R_{\text{gal}})$  is needed.

In comparison, NGC 6946 has a similar, rather flat, distribution of atomic gas, with  $\Sigma(\text{atomic}) \sim 10 M_\odot \text{ pc}^{-2}$ . The molecular gas distribution is similar to that of the MW, except for a clearer and stronger peak within  $R_{\text{gal}} = 2$  kpc. The distribution of  $\Sigma(\text{SFR})$  follows the molecular gas in both galaxies, more clearly so in NGC 6946.

We discuss the MW distributions from the outside, moving inward. The average surface density of molecular gas drops precipitously beyond 13.5 kpc, after a local peak in the Perseus arm (Heyer et al. 1998), as does the stellar density (Ruphy et al. 1996), thereby defining the far outer Galaxy, and the radius used in our whole Galaxy quantities (§5.1.2). The atomic surface density also begins to drop around 13-17 kpc, following an exponential with scale length 3.74 kpc (Kalberla & Kerp 2009). Molecular clouds in the far outer galaxy are rare, but can be found with large-scale surveys. Star formation does continue in the rare molecular clouds (Wouterloot & Brand 1989), and Figure 7 would suggest a higher ratio of star formation to molecular gas, but there are issues of incompleteness in the outer galaxy. A study of individual regions (Snell et al. 2002) found a value of  $L_{\text{FIR}}/M$  similar to that for the inner Galaxy. They conclude that the star formation process within a cloud is not distinguishable from that in the inner Galaxy; the low global rate of star formation is set by the inefficient conversion of atomic to molecular gas in the far outer Galaxy. This result is consistent with the results of Schruba et al. (2011) for other galaxies, as exemplified by NGC 6946.

Inside about 13 kpc, the atomic surface density is roughly constant at  $10\text{--}15 M_\odot \text{ pc}^{-2}$ , while the average molecular surface density increases sharply, passing  $1 M_\odot \text{ pc}^{-2}$  somewhere near the solar neighborhood (Dame et al. 2001), to a local maximum around  $R_{\text{gal}} = 4\text{--}5$  kpc (Nakanishi & Sofue 2006). After a small decrease inside 4 kpc, the surface density rises sharply within  $R_{\text{gal}} = 1$  kpc. Nakanishi & Sofue (2006) and thus Figure 7 use a constant  $X(\text{CO})$ , which could overestimate the molecular mass near the center (§2.4).

The innermost part of the MW,  $R_{\text{gal}} < 250$  pc, known as the Central Molecular Zone (CMZ), potentially provides an opportunity for a close look at conditions in galactic nuclei without current AGN activity, provided that the issues of non-circular motions, foreground and

background confusion, and possible changes in  $X(\text{CO})$  (Oka et al. 1998) can be overcome. Despite their conclusion that  $X(\text{CO})$  is lower, Oka et al. (1998) argue that the CMZ has a molecular mass of  $2\text{--}6 \times 10^7 M_\odot$ . Analysis of dust emission yields a mass of  $5 \times 10^7 M_\odot$  (Pierce-Price et al. 2000), which leads to  $\Sigma_{\text{gas}} = 250 M_\odot \text{ pc}^{-2}$  for the CMZ. A TIR luminosity of  $4 \times 10^8 L_\odot$  (Sodroski et al. 1997) for the CMZ would imply  $\dot{M}_* \sim 0.06 M_\odot \text{ yr}^{-1}$  using the conversion in Table 1, roughly consistent with other recent estimates (Immer et al. 2012), based on analysis of point infrared sources, but new data from the surveys mentioned above should allow refinement of these numbers. Evidence for variations in star formation rate on short timescales is discussed by Yusef-Zadeh et al. (2009). Using  $\dot{M}_* = 0.06 M_\odot \text{ yr}^{-1}$  and  $R_{\text{gal}} = 0.25 \text{ kpc}$  for the CMZ,  $\Sigma(\text{SFR}) = 300 M_\odot \text{ Gyr}^{-1} \text{ pc}^{-2}$ . These values of  $\Sigma_{\text{mol}}$  and  $\Sigma(\text{SFR})$  for the CMZ are plotted separately in Figure 7 and identified as “CMZ.” If correct, the CMZ of the MW begins to look a bit more like the inner few kpc of NGC 6946. The CMZ provides an excellent place to test scaling relations, including those for dense gas, in detail, if the complicating issues can be understood. Preliminary results suggest that  $\Sigma(\text{SFR})$  is similar to that expected from  $\Sigma_{\text{mol}}$  (see Fig. 7), but lower than expected from dense gas relations (S. Longmore, personal communication).

The properties of clouds and clumps also may vary with  $R_{\text{gal}}$ . Heyer et al. (2009) reanalyzed cloud properties in the inner Galaxy based on CO and  $^{13}\text{CO}$  surveys. For the area of the cloud defined roughly by the 1 K CO detection threshold, he found a median  $\Sigma_{\text{mol}}(\text{cloud}) = 42 M_\odot \text{ pc}^{-2}$  for clouds, substantially less than originally found by Solomon et al. (1987), and only a few clouds have  $\Sigma_{\text{mol}}(\text{cloud}) > 100 M_\odot \text{ pc}^{-2}$ . Analysis based on detection thresholds for  $^{13}\text{CO}$  yield a median  $\Sigma_{\text{mol}}(^{13}\text{CO clump}) = 144 M_\odot \text{ pc}^{-2}$  for “ $^{13}\text{CO}$  clumps” (Roman-Duval et al. 2010, who refer to them, however as clouds). The mean in 0.5 kpc bins of surface density per  $^{13}\text{CO}$  clump is roughly constant at  $180 M_\odot \text{ pc}^{-2}$  from  $R_{\text{gal}} = 3$  to 6.6 kpc, beyond which it drops sharply toward the much lower values in the solar neighborhood. Assuming the region sampled is representative, Roman-Duval et al. (2010) have plotted the azimuthally averaged surface density of  $^{13}\text{CO}$  clumps versus Galactocentric radius; it peaks at  $2.5 M_\odot \text{ pc}^{-2}$  at 4.5 kpc, declining to  $< 0.5 M_\odot \text{ pc}^{-2}$  beyond 6.5 kpc. The clouds do appear to be associated with spiral arms, so azimuthal averaging should be taken with caution. The cloud mass function of 246 clouds in the far outer galaxy has a power-law slope of  $\alpha_{\text{cloud}} = -1.88$ , similar to but slightly steeper than that found inside the solar circle (§2.5) and a maximum mass of about  $10^4 M_\odot$  (Snell et al. 2002). The lower value for the maximum mass of a cloud seems to result in a concomitant limit on the number of stars formed in a cluster, but no change is inferred for the intrinsic IMF (Casassus et al. 2000). A piece of a spiral arm at  $R_{\text{gal}} = 15 \text{ kpc}$  has been recently identified in H I and CO, containing a molecular cloud with  $M = 5 \times 10^4 M_\odot$  (Dame & Thaddeus 2011).

#### 5.1.4. Non-axisymmetric Structure

The molecular gas surface density shows a strong local maximum around  $R_{\text{gal}} = 4.5 \text{ kpc}$  in the northern surveys (Galactic quadrants I and II), while southern surveys (quadrants III and IV) show a relatively flat distribution of  $\Sigma_{\text{mol}}$  from about 2 to 7 kpc (Bronfman et al. 2000). This asymmetry is likely associated with spiral structure (Nakanishi & Sofue 2006) and a long (half-length of 4.4 kpc) bar (Benjamin et al. 2005). The star formation rate, measured from  $L_{\text{FIR}}$ , does not, however, reflect this asymmetry; in fact, it is larger in quadrant IV than in I, suggesting a star formation efficiency up to twice as high, despite the lower peak  $\Sigma_{\text{mol}}$  (Bronfman et al. 2000). Interestingly, the distribution of denser gas, traced by millimeter-wave dust continuum emission (Beuther et al. 2012), is also symmetric on kpc scales, but asymmetries appear within the CMZ region (Bally et al. 2010). Major concentrations of molecular clouds with very active star formation appear to be associated with regions of low shear (Luna et al. 2006), and with the junction of the bar and spiral arms (Nguyen Luong et al. 2011).

#### 5.2. Demographics of Star-Forming Galaxies Today

The recent influx of multi-wavelength data has expanded the richness of information available on global star formation properties of galaxies, and transformed the interpretive framework from one based on morphological types to a quantitative foundation based on galaxy luminosities, masses, and other physical properties.

The role of galaxy mass as a fundamental determinant of the star formation history of a galaxy has been long recognized (e.g., Gavazzi & Scodeggio 1996), but data from SDSS and subsequent surveys have reshaped our picture of the population of star-forming galaxies (e.g., Kauffmann et al. 2003; Baldry et al. 2004, 2006; Brinchmann et al. 2004). The integrated colors of galaxies, which are sensitive to their star formation histories, show a strongly bimodal dependence on stellar mass, with a relatively tight “red sequence” populated by galaxies with little or no current star formation, and a somewhat broader “blue sequence” or “blue cloud” of actively star-forming galaxies. The dominant population shifts from blue to red near a transition stellar mass of  $\sim 3 \times 10^{10} M_\odot$  (Kauffmann et al. 2003). The relative dearth of galaxies in the “green valley” between the red and blue sequences suggests a deeper underlying physical bimodality in the galaxy population and a rapid evolution of galaxies from blue to red sequences.

A similar bimodality characterizes the mass dependence of the SFR per unit galaxy mass (SSFR). The mass dependence of the SSFR has been explored by numerous investigators (e.g., Brinchmann et al. 2004; Salim et al. 2007; Schiminovich et al. 2007; Lee et al. 2007). Figure 8 shows an example from Schiminovich et al. (2007), based in this case on dust-corrected FUV measurements of SDSS galaxies.

A clear separation between the blue and red sequences is evident, and the dispersion of SSFRs within the blue sequence is surprisingly small, suggesting that some kind of self-regulation mechanism may be at work among the actively star-forming galaxies. The bimodality is not absolute; there is a clear tail of less active but significantly star forming galaxies between the two sequences. These

represent a combination of relatively inactive (usually early-type) disk galaxies and unusually active spheroid-dominated systems (§5.4). The sharp increase in the fraction of inactive galaxies above stellar masses of order a few times  $10^{10} M_{\odot}$  is also seen.

The blue sequence in Figure 8 is not horizontal; the SSFR clearly increases with decreasing galaxy mass. The slope ( $-0.36$  for the data in Figure 8) varies somewhat between different studies, possibly reflecting the effects of different sampling biases. The negative slope implies that lower-mass galaxies are forming a relatively higher fraction of their stellar mass today, and thus must have formed relatively fewer of their stars (compared to more massive galaxies) in the past. The most straightforward explanation is that the dominant star-forming galaxy population in the Universe has gradually migrated from more massive to less massive galaxies over cosmic time. Direct evidence for this “downsizing” is seen in observations of the SSFR vs mass relation in high-redshift galaxies (e.g., Noeske et al. 2007).

Another instructive way to examine the statistical properties of star-forming galaxies is to compare absolute SFRs and SFRs normalized by mass or area. Several interesting trends can be seen in Figure 9, which plots integrated measurements of the SFR per unit area as a function of the absolute SFRs. The first is the extraordinary range in SFRs, more than seven orders of magnitude, whether measured in absolute terms or normalized per unit area or (not shown) galaxy mass. Much of this range is contributed by non-equilibrium systems (starbursts). Normal galaxies occupy a relatively tight range of SFRs per unit area, reminiscent of the tightness of the blue sequence when expressed in terms of SSFRs. The total SFRs of the quiescent star-forming galaxies are also tightly bounded below a value of  $\sim 20 M_{\odot} \text{ yr}^{-1}$ . Starburst galaxies, and infrared-luminous and ultraluminous systems in particular, comprise most of the galaxies in the upper 2–3 decades of absolute SFRs and  $\Sigma(\text{SFR})$ .

The distribution of SFRs along the X-axis of Figure 9 (after correcting for volume completeness biases) is simply the SFR distribution function (e.g., Gallego et al. 1995; Martin et al. 2005b). Figure 10 shows a recent determination of this distribution from Bothwell et al. (2011), based on flux-limited UV and TIR samples of galaxies and SFRs derived using the methods of Hao et al. (2011), and corrections for AGN contamination following Wu et al. (2010b, 2011). The SFR function is well fitted by a Schechter (1976) exponentially truncated power-law, with a faint-end slope  $\alpha = -1.5$  and characteristic SFR,  $\text{SFR}^* = 9 M_{\odot}$ . Although SFRs as high as  $\sim 1000 M_{\odot} \text{ yr}^{-1}$  are found in present-day ULIRGs, the contribution of LIRGs and ULIRGs to the aggregate star formation today is small ( $< 10\%$  also see Goto et al. 2011). Steady-state star formation in galaxies dominates today. The value of  $\text{SFR}^*$  increases rapidly with  $z$ , and galaxies with  $L_{\text{bol}} > 10^{11} L_{\odot}$  (i.e., LIRGs) become dominant by redshifts  $z > 1$  (e.g., Le Floc'h et al. 2005). This change partly reflects an increase in merger-driven star formation at higher redshift, but at early epochs even the steady-state star formation in massive galaxies attained levels of order tens to hundreds of solar masses per year, thus placing those galaxies in the LIRG and ULIRG regime. This suggests that most of the decrease in the cosmic SFR in recent epochs has been driven by downsiz-

ing in the level of steady-state star formation (e.g., Bell et al. 2005; Jogee et al. 2009).

### 5.3. The High-Density Regime: Starbursts

As highlighted in §1.2, the starburst phenomenon encompasses a wide range of physical scales and host galaxy properties, and no precise physical definition of a starburst has been placed into wide use. Part of the explanation can be seen in Fig. 9; although the most extreme starburst galaxies have properties that are well separated from those of normal star-forming galaxies, there is no clear physical break in properties; starbursts instead define the upper tails of the overall distributions in SFRs within the general galaxy population.

Much of the attention in this area continues to focus on the infrared-luminous and ultraluminous systems, because they probe star formation in the most extreme high-density circumnuclear environments seen in the local Universe. A major breakthrough in recent years has been the use of mid-infrared spectroscopy to distinguish dust heated by massive stars from that heated by a buried AGN (e.g., Genzel et al. 1998; Laurent et al. 2000; Dale et al. 2006; Armus et al. 2007). Regions heated by AGNs are distinguished by the appearance of highly ionized atomic species, as well as suppressed mid-infrared PAH emission relative to stellar-heated dust. Application of these diagnostics has made it possible to construct clean samples of LIRGs and ULIRGs that are dominated by star formation.

With the Spitzer and Herschel observatories, it has been possible to extend imaging and spectroscopy of the most luminous infrared-emitting galaxies to intermediate redshifts (e.g., Elbaz et al. 2005; Yan et al. 2007). As mentioned earlier the fraction of star formation in LIRGs and ULIRGs increases sharply with redshift, but imaging and spectroscopy of these objects reveals a marked shift in the physical characteristics of the population. Whereas at low redshift, ULIRGs (and many LIRGs) are dominated by very compact circumnuclear starbursts triggered by mergers, at higher redshifts the LIRG/ULIRG population becomes increasingly dominated by large disk galaxies with extended star formation. As a consequence of cosmic downsizing (i.e., “upsizing” with increasing redshift), by redshifts  $z \sim 1$  the populations of LIRGs and ULIRGs become increasingly dominated by the progenitors of present-day normal galaxies, rather than by the transient merger-driven starbursts which dominate the present-day populations of ULIRGs, though examples of the latter are still found, especially in the population of submillimeter-luminous galaxies (SMGs) (e.g., Chapman et al. 2005).

Visible-wavelength observations of these high-redshift galaxies with IFU instruments, both with and without adaptive optics correction, have revealed many insights into the physical nature of this population of starburst galaxies (e.g., Genzel et al. 2008, 2011; Förster Schreiber et al. 2009 and references therein). The  $\text{H}\alpha$  kinematics show a wide range of properties, from normal, differentially rotating disks to disturbed disks, and a subset with signatures of ongoing or recent mergers. The disks tend to be characterized by unusually high velocity dispersions, which have been interpreted as reflecting a combination of dynamical instability and possibly energy injection into the ISM from young stars. Further discus-

sion of high-redshift galaxies is beyond the scope of this article, but we shall return to the cold ISM properties and SFRs of these galaxies in §6.

#### 5.4. The Low SFR and Low Density Regimes

One of the most important discoveries from the GALEX mission was the detection of low levels of star formation in environments which were often thought to have been devoid of star formation. These include early-type galaxies, dwarf galaxies, low surface brightness galaxies, and the extreme outer disks of many normal galaxies.

Although star formation had been detected occasionally in nearby elliptical and S0 galaxies (e.g., Pogge & Eskridge 1993), most of these galaxies have historically been regarded as being “red and dead” in terms of recent star formation. Deep GALEX imaging of E/S0 galaxies (e.g., Kaviraj et al. 2007), however, has revealed that approximately 30% of these early-type galaxies exhibit near-ultraviolet emission in excess of what could reasonably arise from an evolved stellar population (e.g., Kaviraj et al. 2007). Confirmation of the star formation has come from visible-wavelength IFU spectroscopy, as exploited for example by the SAURON survey (Shapiro et al. 2010). The SFRs in these galaxies tend to be very low, with at most 1–3% of the stellar mass formed over the past Gyr. High-resolution UV imaging with HST often reveals extended star-forming rings or spiral arms in these galaxies (Salim & Rich 2010). Follow-up CO observations of these galaxies reveals significant detections of molecular gas in a large fraction of the galaxies with detected star formation, with molecular gas masses of  $10^7 - 10^{10} M_\odot$  (Combes et al. 2007; Crocker et al. 2011), and with SFRs roughly consistent with the Schmidt law seen in normal galaxies.

The GALEX images also reveal that star formation in more gas-rich disk galaxies often extends much farther in radius than had previously been appreciated. In exceptional cases (e.g., NGC 5236=M83, NGC 4625) the star formation extends to 3–4 times the normal  $R_{25}$  optical radius, to the edge of the HI disk (Thilker et al. 2005; Gil de Paz et al. 2005). A systematic study by Thilker et al. (2007) reveals that extended “XUV disks” are found in ~20% of spiral galaxies, with less distinct outer UV structures seen in another ~10% of disk galaxies. Follow-up deep H $\alpha$  imaging and/or spectroscopy reveals extended disks of HII regions that trace the UV emission in most cases (e.g., Zaritsky & Christlein 2007; Christlein et al. 2010; Goddard et al. 2010), confirming the earlier detection of HII regions at large radii (e.g., Ferguson et al. 1998; Ryan-Weber et al. 2004). Individual examples of extended UV features without H $\alpha$  counterparts are sometimes found, however (Goddard et al. 2010). The GALEX images also have led to a breakthrough in measurements of star formation in low surface brightness spiral galaxies (LSBs). These provide a homogeneous body of deep measurements of the star formation and the nature of the star formation law at low surface densities (§6; Wyder et al. 2009). Comparison to the outer MW (§5.1) suggests that deep searches for molecular gas will find few clouds, which will nonetheless, be the sites of star formation.

The other low-density star formation regime can be found in dwarf irregular galaxies. Drawing general in-

ferences about the star formation properties of these galaxies requires large samples with well-defined (ideally volume-limited) selection criteria, and studies of this kind (based on UV, visible, and/or H $\alpha$  observations) have been carried out by several groups (e.g., Karachentsev et al. 2004; Blanton et al. 2005; Meurer et al. 2006; Kennicutt et al. 2008; Dalcanton et al. 2009; Hunter et al. 2010). One perhaps surprising result is the near ubiquity of star formation in the dwarf galaxies. Kennicutt et al. (2008) observed or compiled H $\alpha$  luminosities for galaxies within the local 11 Mpc, which included ~300 dwarf galaxies ( $M_B > -17$ ). Excluding a handful of dwarf spheroidal galaxies which have no cold gas, only 10 of these (~3%) were not detected in H $\alpha$ , meaning that star formation has taken place over the last 3–5 Myr in the other 97% of the systems. Moreover many of the handful of H $\alpha$  non-detections show knots of UV emission, demonstrating that even fewer of the galaxies have failed to form stars over the last ~100 Myr (Lee et al. 2011). Recent star formation is seen in all of the galaxies with  $M_B < -13$  and  $M(HI) > 5 \times 10^7 M_\odot$ . For less massive galaxies it is possible for star formation to cease for timescales that are longer than the ionization lifetime of an HII region (up to 5 Myr), but examples of galaxies with extended periods of no star formation are extremely rare.

These data also provide a fresh look at the temporal properties of the star formation in dwarf galaxies generally. The distribution of SSFRs shows a marked increase in dispersion for galaxies with  $M_B > -14.5$  or circular velocity of  $50 \text{ km s}^{-1}$  (Lee et al. 2007; Bothwell et al. 2009). The corresponding neutral gas fraction does not show a similar increase in dispersion (Bothwell et al. 2009), so this suggests an increased short-term fluctuation of integrated SFRs in low-mass galaxies. Lee et al. (2009b) analyzed the statistics of the SFRs in more depth and confirmed a larger fraction of stars formed in bursts in low-mass galaxies (~25%), but these still represent only a small fraction of the total stars formed— even in the dwarfs the majority of stars appear to form in extended events of duration longer than ~10 Myr. Recent modelling of the statistics of H $\alpha$  and UV emission by Weisz et al. (2012) and Fumagalli et al. (2011) as well as analysis of resolved stellar populations (e.g., Weisz et al. 2008) confirm the importance of fluctuations in the SFR.

## 6. STAR FORMATION RELATIONS

The immense dispersion in SFR properties seen in Figure 9 collapses to a remarkably tight scaling law when the SFR surface densities ( $\Sigma(\text{SFR})$ ) are plotted against mean gas surface densities ( $\Sigma_{\text{gas}}$ ) (Kennicutt 1998b). This emergent order reflects the fact that gas is the input driver for star formation. The concept of a power-law relation between SFR density and gas density dates to Schmidt (1959, 1963), and relations of this kind are commonly referred to as “Schmidt laws.” On physical grounds we might expect the most fundamental relation between the volume densities of star formation and gas, but since most observations of external galaxies can only measure surface densities integrated along the line of sight, the most commonly used relation, often called a Kennicutt-Schmidt (KS) law, is in terms of surface densities.



$$\Sigma_{SFR} = A \Sigma_{gas}^N \quad (13)$$

The precise form of this relation depends on assumptions about how  $\Sigma_{gas}$  is derived from the observations (§2.4), but a strong correlation is clearly present.

### 6.1. The Disk-Averaged Star Formation Law

K98 presented a review of observations of the Schmidt law up to the time, and nearly all of that work characterised the relation between the disk-averaged SFR and gas surface densities in galaxies. The upper panel of Figure 11 presents an updated version of the global Schmidt law in galaxies. Each point is an individual galaxy (color coded as explained in the caption), with the surface density defined as the total gas mass (molecular plus atomic) or SFR normalized to the radius of the main star-forming disk, as measured from H $\alpha$ , Pa $\alpha$ , or IR maps. For simplicity, a constant  $X(\text{CO})$  factor [ $2.3 \times 10^{20} \text{ cm}^{-2} (\text{K km s}^{-1})^{-1}$  with no correction for helium, see §2.4] has been applied to all of the galaxies; the consequences of a possible breakdown in this assumption are discussed later. The sample of galaxies has been enlarged from that studied in Kennicutt (1998b), and all of the H $\alpha$ -based SFR measurements have been improved by incorporating individual (IR-based) corrections for dust attenuation and [N II] contamination.

The form of this integrated Schmidt law appears to be surprisingly insensitive to SFR environment and parameters such as the atomic versus molecular fraction, but some metal-poor galaxies (defined as  $Z < 0.3Z_{\odot}$ ) deviate systematically from the main relation, as shown by the blue open circles in Figure 11 (upper panel). These deviations could arise from a physical change in the star formation law itself, but are more likely to reflect a breakdown in the application of a constant  $X(\text{CO})$  factor (§2.4; Leroy et al. 2011, and references therein). Adopting higher values of  $X(\text{CO})$  for metal-poor galaxies brings the galaxies much more into accord with the main relation in Figure 11.

Recent observations of LSBs by Wyder et al. (2009) extend the measurements of the integrated star formation law to even lower mean surface densities, as shown by the purple crosses in the upper panel of Figure 11. A clear turnover is present, which is consistent with breaks seen in spatially-resolved observations of the star formation law (§6.2).

The slope of the integrated Schmidt law is non-linear, with  $N \simeq 1.4\text{--}1.5$  (Kennicutt 1998b), when a constant  $X(\text{CO})$  factor is applied. This uncertainty range does not include all possible systematic errors, arising for example from changes in  $X(\text{CO})$  or the IMF with increasing surface density or SFR. Major systematic changes in either of these could easily change the derived value of  $N$  by as much as 0.2–0.3. For example, if  $X(\text{CO})$  were five times lower in the dense starburst galaxies (§2.4), the slope of the overall Schmidt law would increase from 1.4–1.5 to 1.7–1.9 (Narayanan et al. 2012).

Usually the Schmidt law is parametrized in terms of the total (atomic plus molecular) gas surface density, but one can also explore the dependences of the disk-averaged SFR densities on the mean atomic and molecular surface densities individually. Among normal galaxies with relatively low mean surface densities, the SFR den-

sity is not particularly well correlated with either component, though variations in  $X(\text{CO})$  could partly explain the poor correlation between SFR and derived H $_2$  densities (e.g., Kennicutt 1998b). In starburst galaxies with high gas surface densities, however, the gas is overwhelmingly molecular, and a strong non-linear Schmidt law is observed (upper panel of Figure 11).

A similar non-linear dependence is observed for total SFR (as opposed to SFR surface density) versus total molecular gas mass (e.g., Solomon & Sage 1988; Gao & Solomon 2004), and presumably is another manifestation of the same underlying physical correlation. The dependence of the SFR on *dense* molecular gas mass is markedly different, however. The lower panel of Figure 11, taken from Gao & Solomon (2004), shows the relation between the integrated SFRs and the dense molecular gas masses, as derived from HCN  $J = 1 \rightarrow 0$  measurements (§2.4) for a sample of normal and starburst galaxies. In contrast to the correlation with total molecular mass from CO  $J = 1 \rightarrow 0$ , this relation is linear, implying a strong coupling between the masses of dense molecular clumps and stars formed, which is largely independent of the galactic star-forming environment. Wu et al. (2005b) have subsequently shown that this linear relation extends down to the scales of individual star-forming molecular clouds and dense clumps in the Galaxy. Combined with the MW studies (§4), these dense gas relations for galaxies suggest that dense clumps are plausible fundamental star-forming units. If so, the mass fraction of the ISM (and fraction of the total molecular gas) residing in dense clumps must itself increase systematically with the SFR.

Because  $L_{\text{HCN}}$  in the  $J = 1 \rightarrow 0$  line is only an approximate tracer for dense gas (§2.4.3) and because the definition of a dense clump is by no means precise (§2.5), one should be careful not to overinterpret these trends. Similar comparisons of the SFR with the emission from other molecular tracers suggest that the slope of the SFR versus gas mass relation changes continuously as one proceeds from lower-density tracers such as CO  $J = 1 \rightarrow 0$  to higher-excitation (and higher-density) CO transitions, and further to high-density tracers such as HCN and HCO $^+$  and to higher transitions of those molecules (e.g., Juneau et al. 2009). Multi-transition studies, along with realistic modeling will help to refine the interpretation of line luminosities of dense gas tracers (e.g., Graciá-Carpio et al. 2008; Juneau et al. 2009).

The data shown in Figure 11 all come from observations of nearby galaxies ( $z < 0.03$ ), but recently a number of studies have addressed the form of the molecular gas Schmidt law for starburst galaxies extending to redshifts  $z \geq 2$  (e.g., Bouché et al. 2007; Daddi et al. 2010; Genzel et al. 2010). The interpretation of these results is strongly dependent on the assumptions made about  $X(\text{CO})$  in these systems. When a Galactic  $X(\text{CO})$  conversion is applied, the high-redshift galaxies tend to fall roughly on the upper parts of the Schmidt law seen locally (e.g., Figure 11). However if a lower  $X(\text{CO})$  factor is applied to the most compact starburst and submillimeter galaxies (SMGs), as suggested by many independent analyses of  $X(\text{CO})$  (§2.4), the Schmidt relations shift leftwards by the same factor, forming a parallel relation (Daddi et al. 2010; Genzel et al. 2010).

Taken at face value, these results suggest the presence of two distinct modes of star formation with differ-

ent global efficiencies, which separate the extended star-forming disks of normal galaxies from those in the densest circumnuclear starbursts; this distinction is likely to be present both in the present-day Universe and at early cosmic epochs. This inferred bimodality, however, is a direct consequence of the assumption of two discrete values for  $X(\text{CO})$  in the two modes. A change in the interpretation of CO emission is certainly plausible when the derived molecular surface density is similar to that of an individual cloud ( $\Sigma_{\text{mol}} > 100 \text{ M}_{\odot} \text{ pc}^{-2}$ ), but the behavior of  $X(\text{CO})$  may be complex (§2.4). Variation of  $X(\text{CO})$  over a continuous range would indicate a steeper Schmidt law, rather than a bimodal law (Narayanan et al. 2012).

Daddi et al. (2010) also note that the higher concentration of gas in the ULIRGs/SMGs is consistent with an enhanced fraction of dense gas and the dense gas relations of Gao & Solomon (2004). However, the star formation rate also appears to be larger for a given mass of dense gas in extreme starbursts (García-Burillo et al. 2012 and references therein), especially when a lower value of  $\alpha_{\text{HCN}}$  is used. As with CO, one can interpret these as bimodal relations or as steeper than linear dependences on the gas tracer lines. These results, together with evidence for lower SFR per mass of dense gas in the CMZ of the MW (§5.1) warn against an overly simplistic picture of dense clumps as the linear building blocks for massive star formation, with no other variables in the picture.

The correlations between SFR and gas surface densities (and masses) are not the only scaling laws that are observed. Kennicutt (1998b) pointed out that the SFR surface densities also correlate tightly with the ratio of the gas surface density to the local dynamical time, defined in that case to be the average orbit time. This prescription is especially useful for numerical simulations and semi-analytical models of galaxy evolution. Interestingly, Daddi et al. (2010) and Genzel et al. (2010) found that the bifurcation of Schmidt laws between normal galaxies and ULIRGs/SMGs described above does not arise in the dynamical form of this relation.

Blitz & Rosolowsky (2006) have discovered another strong scaling relation between the ratio of molecular to atomic hydrogen in disks and the local hydrostatic pressure. The relation extends over nearly three orders of magnitude in pressure and  $\text{H}_2/\text{H I}$  ratio and is nearly linear (slope = 0.92). Technically speaking this scaling relation only applies to the phase balance of cold gas rather than the SFR, but it can be recast into a predicted star formation law if assumptions are made about the scaling between the SFR and the molecular gas components (e.g., Blitz & Rosolowsky 2006; Leroy et al. 2008). Recent work by Ostriker et al. (2010) and Ostriker & Shetty (2011) provides a theoretical explanation for these relations.

Finally, a number of workers have explored the scaling between SFR surface density and a combination of gas and stellar surface densities. For example Dopita (1985) and Dopita & Ryder (1994) proposed a scaling between the SFR density and the product of gaseous and stellar surface densities; the latter scales with the disk hydrostatic pressure and hence bears some relation to the picture of Blitz & Rosolowsky (2006). More recently Shi et al. (2011) show that the scatter in the star formation law is minimized with a relation of the form  $\Sigma_{\text{SFR}} \propto \Sigma_{\text{gas}} \Sigma_{*}^{0.5}$ .

Determining which of these different formulations of the star formation law is physical and which are mere consequences of a more fundamental relation is difficult to determine from observations alone. Some of the degeneracies between these various relations can be understood if most gas disks lie near the limit of gravitational stability ( $Q \sim 1$ ; Kennicutt 1989), and the critical column densities for the formation of cold gas phase, molecule formation, and gravitational instability lie close to each other (e.g., Elmegreen & Parravano 1994; Schaye 2004). In such conditions it can be especially difficult to identify which physical process is most important from observations. We return to this topic later.

We conclude this section by mentioning that there are other SFR scaling laws that can be understood as arising from an underlying Schmidt law. The best known of these is a strong correlation between characteristic dust attenuation in a star-forming galaxy and the SFR itself, with the consequence that galaxies with the highest absolute SFRs are nearly all dusty infrared-luminous and ultraluminous galaxies (e.g., Wang & Heckman 1996; Martin et al. 2005b; Bothwell et al. 2011). This opacity versus SFR relation is partly a manifestation of the Schmidt law, because we now know that the most intense star formation in galaxies takes place in regions with abnormally high gas surface densities, and thus also in regions with abnormally high dust surface densities. The other factor underlying the SFR versus opacity correlation is the prevalence of highly concentrated circumnuclear star formation in the most intense starbursts observed in the present-day universe (§5.3); this may not necessarily be the case for starburst galaxies at early cosmic epochs.

## 6.2. Radial Distributions of Star Formation and Gas

Over the past few years major progress has been made in characterizing the spatially-resolved star formation law within individual galaxies. This work has been enabled by large multi-wavelength surveys of nearby galaxies such as the Spitzer Infrared Nearby Galaxies Survey (SINGS) (Kennicutt et al. 2003), the GALEX Nearby Galaxies Survey (Gil de Paz et al. 2007), the Spitzer/GALEX Local Volume Legacy survey (LVL; Dale et al. 2009; Lee et al. 2011), and the Herschel KINGFISH Survey (Kennicutt et al. 2011). The resulting datasets provide the means to measure spatially-resolved and dust-corrected SFRs across a wide range of galaxy properties (§3). These surveys in turn have led to large spinoff surveys in H I (e.g., THINGS, Walter et al. 2008; FIGGS, Begum et al. 2008; Local Volume H I Survey; Koribalski 2010; LITTLE THINGS, Hunter et al. 2007) and in CO (e.g., BIMA-SONG, Helfer et al. 2003; IRAM HERACLES, Leroy et al. 2009; JCMT NGLS, Wilson et al. 2009; CARMA/NRO Survey, Koda & Nearby Galaxies CO Survey Group 2009; CARMA STING, Rahman et al. 2011, 2012).

The capabilities of these new datasets are illustrated in Figure 6, which shows Spitzer  $24 \mu\text{m}$ ,  $\text{H}\alpha$ , VLA H I, and CO (in this case from HERACLES) maps of NGC 6946 (see Figure 7 for the corresponding radial distributions of gas and star formation).

The first step in exploiting the spatial resolution of the new observations is to analyze the azimuthally-averaged radial profiles of the SFR and gas components (as illustrated for example in Figure 7) and the resulting SFR

versus gas surface density correlations. This approach has the advantage of spatially averaging over large physical areas, which helps to avoid the systematic effects that are introduced on smaller spatial scales (§3.9). Radial profiles also have limitations arising from the fact that a single radial point represents an average over sub-regions with often wildly varying local gas and SFR densities, and changes in other radially varying physical parameters may be embedded in the derived SFR versus gas density relations.

Large-scale analyses of the star formation law derived in this way have been carried out by numerous authors (e.g., Kennicutt 1989; Martin & Kennicutt 2001; Wong & Blitz 2002; Boissier et al. 2003; Heyer et al. 2004; Komugi et al. 2005; Schuster et al. 2007; Leroy et al. 2008; Schruba et al. 2011; Gratier et al. 2010). A strong correlation between SFR and gas surface density is seen in nearly all cases, with a non-linear slope when plotted in terms of total (atomic+molecular) density. The best fitting indices  $N$  vary widely, however, ranging from 1.4–3.1 for the dependence on total gas density and 1.0–1.4 for the dependence on molecular gas surface density alone (for constant  $X(\text{CO})$ ). The measurements of the MW range from  $N = 1.2 \pm 0.2$ , when only molecular gas is used (Luna et al. 2006), to  $2.18 \pm 0.20$  when total (atomic and molecular) gas is used (Misiriotis et al. 2006).

Some of the differences between these results can be attributed to different schemes for treating dust attenuation, different CO line tracers, different metallicities (which may influence the choice of  $X(\text{CO})$ ), and different fitting methods. The influence of a metallicity-dependent  $X(\text{CO})$  factor is investigated explicitly by Boissier et al. (2003). Since any variation in  $X(\text{CO})$  is likely to flatten the radial molecular density profiles, a variable conversion factor tends to steepen the slope of the derived Schmidt law; for the prescription they use, the best fitting slope can increase to as high as  $N = 2.1 - 3.6$ , underscoring once again the critical role that assumptions about  $X(\text{CO})$  play in the empirical determination of the star formation law. Despite these differences in methodology, real physical variation in the SFR versus gas density relation on these scales cannot be ruled out.

This body of work also confirms the presence of a turnover or threshold in the star formation relation at low surface densities in many galaxies. Early work on this problem (e.g., Kennicutt 1989; Martin & Kennicutt 2001; Boissier et al. 2003) was based on radial profiles in  $\text{H}\alpha$ , and some questions have been raised about whether these thresholds resulted from breakdowns in the SFR versus  $\text{H}\alpha$  calibration in low surface brightness regimes, as opposed to real thresholds in the SFR. Subsequent comparisons of UV and  $\text{H}\alpha$  profiles appear to confirm the presence of radial turnovers in the SFR in most disks, however, even in cases where lower levels of star formation persist to much larger radii (e.g., Thilker et al. 2007; Christlein et al. 2010; Goddard et al. 2010). This extended star formation can be seen in Figure 7 ( $R > 7 - 8$  kpc). Recent studies of nearby galaxies with unusually extended XUV disks also show that the UV-based SFR falls off much more rapidly than the cold gas surface density, with global star formation efficiencies ( $\epsilon'$ ) an order of magnitude or more lower than those in the inner disks (Bigiel et al. 2010). Taken together, these recent results and studies of the outer MW (§5.1) confirm the presence

of a pronounced turnover in the Schmidt law for total gas at surface densities of order a few  $\text{M}_\odot \text{pc}^{-2}$  (Figure 12).

### 6.3. The Star Formation Law on Sub-Kiloparsec Scales

The same multi-wavelength data can be used in principle to extend this approach to point-by-point studies of the star formation law. The angular resolution of the currently available datasets (optical/UV, mid-far IR, H I, CO) allows for extending this analysis down to angular scales of  $\sim 10''$ , which corresponds to linear scales of 30–50 pc in the Local group and 200–1000 pc for the galaxies in the local supercluster targeted by SINGS, THINGS, KINGFISH, and similar surveys. Recent analyses have become available (Kennicutt et al. 2007; Bigiel et al. 2008, 2010, 2011; Leroy et al. 2008; Blanc et al. 2009; Eales et al. 2010; Verley et al. 2010; Liu et al. 2011; Rahman et al. 2011, 2012; Schruba et al. 2011), and several other major studies are ongoing.

The most comprehensive attack on this problem to date is based on a combination of SINGS, THINGS, and HERACLES observations (papers above by Bigiel, Leroy, and Schruba), and Figure 12, taken from Bigiel et al. (2008), nicely encapsulates the main results from this series of studies. The colored regions are the loci of individual sub-kiloparsec measurements of SFR surface densities (measured from a combination of FUV and  $24 \mu\text{m}$  infrared fluxes) and total gas densities (H I plus  $\text{H}_2$  from CO(2–1) with a constant  $X(\text{CO})$  factor), for 18 galaxies in the SINGS/THINGS sample. Other data (including Kennicutt 1998b) are overplotted as described in the figure legend and caption. The measurements show at least two distinct regimes, a low-density sub-threshold regime where the dependence of the SFR density on gas density is very steep (or uncorrelated with gas density), and a higher density regime where the SFR is strongly correlated with the gas density. The general character of this relation, with a high-density power law and a low-density threshold confirms most of the results presented earlier.

One can also examine separately the dependence of the SFR density on the atomic and molecular surface densities and the two relations are entirely different. The local SFR density is virtually uncorrelated with H I density, in part because the range of H I column densities is truncated above  $\Sigma_{\text{HI}} \sim 10 \text{M}_\odot \text{pc}^{-2}$  or  $N(\text{H I}) \sim 10^{21} \text{cm}^{-2}$ . This upper limit to the local H I densities corresponds to the column density where the H I efficiently converts to molecular form. This phase transition also roughly coincides with the turnover in the SFRs in Figure 12, which hints that the SFR threshold itself may be driven in part, if not entirely, by an atomic–molecular phase transition (see §7).

In contrast to the H I, the SFR surface density is tightly correlated with the  $\text{H}_2$  surface density, as inferred from CO. A recent stacking analysis of the HERACLES CO maps made it possible to statistically extend this comparison to low  $\text{H}_2$  column densities, and it shows a tight correlation between SFR and CO surface brightness that extends into the H I-dominated (sub-threshold) regime (Schruba et al. 2011), reminiscent of studies in the outer MW (Fig. 7, §5.1).

The strong local correlation between  $\Sigma(\text{SFR})$  and  $\Sigma_{\text{mol}}$  is seen in all of the recent studies which probe linear scales of  $\sim 200$  pc and larger. This is hardly surpris-

ing, given the strong coupling of star formation to dense molecular gas in local clouds (§4, §6.4). However, on smaller linear scales the measurements show increased scatter for reasons discussed in §3.9. On these scales we expect the scaling laws to break down, as the stars and gas may arise from separate regions; this effect has been directly observed in high-resolution observations of M33 (Onodera et al. 2010).

The main results described above – the presence of a power-law SFR relation with a low-density threshold, the lack of correlation of the local SFR with H I column density, the strong correlation with H<sub>2</sub> column density, and the rapidly increasing scatter in the Schmidt law on linear scales below 100–200 pc – are seen consistently across most, if not all, recent spatially-resolved studies. Most of the recent studies also derive a mildly non-linear slope to the SFR density versus total gas density Schmidt law in the high-density regime, with indices  $N$  falling in the range 1.2–1.6. Less clear from the recent work is the linearity and slope of the Schmidt law on small scales, especially the dependence of SFR surface density on molecular gas surface density. The results from the HERACLES/THINGS studies have consistently shown a roughly linear  $\Sigma_{SFR}$  versus  $\Sigma_{mol}$  relation ( $N = 1.0$ – $1.1$ ), and similar results have been reported by Blanc et al. (2009), Eales et al. (2010), and Rahman et al. (2012). Other authors however have reported steeper dependences ( $N = 1.2$ – $1.7$ ), closer to those seen in integrated measurements (e.g., Kennicutt et al. 2007; Verley et al. 2010; Rahman et al. 2011; Liu et al. 2011; Momose 2012). The discrepancies between these results are much larger than the estimated fitting errors, and probably arise in part from systematic differences in the observations and in the way the data are analyzed (see discussion in e.g., Blanc et al. 2009). One effect which appears to be quite important is the way in which background diffuse emission is treated in measuring the local SFRs (§3.9). Liu et al. (2011) show that they can produce either a linear or non-linear local molecular SFR law depending on whether or not the diffuse emission is removed. Another CARMA-based study by Rahman et al. (2011), however, suggests that the effects of diffuse emission may not be sufficient to account for all of the differences between different analyses. Another important factor may be the excitation of the CO tracer used (e.g., Juneau et al. 2009).

It is important to bear in mind that nearly all of our empirical knowledge of the form of the local star formation law is based on observations of massive gas-rich spiral galaxies with near-solar gas-phase metal abundances. Most studies of the star formation relations in metal-poor dwarf galaxies have been limited to H I data or marginal detections in CO at best (e.g., Bigiel et al. 2008). A recent study of the SMC ( $\sim 1/5 Z_{\odot}$ ) by Bolatto et al. (2011) offers clues to how these results may change in low-metallicity environments. They find that the atomic-dominated threshold regime extends up to surface densities that are an order of magnitude higher than in spirals.

#### 6.4. Local Measurements of Star Formation Relations

With the ongoing large-scale surveys of the Galaxy and the Magellanic Clouds in recent years it is becoming possible to investigate star formation rate indicators, the scaling laws, and other star formation relations for local samples. These can provide valuable external checks on

the methods applied on larger scales to external galaxies and probe the star formation relations on physical scales that are not yet accessible for other galaxies. Local studies of the conversion of CO observations into column density or mass were discussed in §2.4.

Comparison of various star formation rate indicators for the MW (§5.1), as would be used by observers in another galaxy, against more direct measures, such as young star counts, suggests that star formation rates based on the usual prescriptions (mid-infrared and radio continuum) may be underestimating absolute  $\dot{M}_{*}$  by factors of 2–3 (Chomiuk & Povich 2011). The authors suggest that changes to the intermediate mass IMF, timescale issues, models for O stars, and stochastic sampling of the upper IMF can contribute to the discrepancy. As discussed earlier, measures of star formation rate that use ionizing photons (H $\alpha$  or radio continuum) require regions with a fully populated IMF to be reliable, and they systematically underestimate the SFR in small star-forming clouds (§3.9). For example, star formation in clouds near the Sun would be totally invisible to these measures and the star formation rate would be badly underestimated in the Orion cluster (§3.9). Tests of other star formation rate tracers, such as 24  $\mu$ m emission, within the Milky Way would be useful. Changes in the IMF as large as those proposed by Chomiuk & Povich (2011) should also be readily observable in more evolved Galactic star clusters, if not in the field star IMF itself.

Using a YSO-counting method for five GMCs in the N159 and N44 regions in the LMC, Chen et al. (2010) were able to reach stellar masses of about 8  $M_{\odot}$ , below which they needed to extrapolate. The resulting ratios of  $\dot{M}_{*}(\text{YSOs})$  to  $\dot{M}_{*}(\text{H}\alpha + 24\mu\text{m})$  ranged from 0.37 to 11.6, with a mean of 3.5.

Recent studies have begun to probe the form of the star formation relations on scales of clouds and clumps. Using the YSO star counting method to get  $\dot{M}_{*}$  and extinction maps to get mean mass surface density of individual, nearby clouds, Evans et al. (2009) found that the local clouds all lay well above the K98 relation. Taken in aggregate, using the mean  $\Sigma_{gas}$ , they lay a factor of 20 above the Kennicutt et al. (1998b) relation and even farther above the relation of Bigiel et al. (2008).

Subsequent studies show evidence for both a surface density threshold for star-forming clumps and a  $\Sigma(\text{SFR})$ - $\Sigma_{mol}$  relation in this high-density sub-cloud regime. Lada et al. (2010) found a threshold surface density for efficient star formation in nearby clouds; the star formation rate per cloud mass scatters widely (Fig. 13), but is linearly proportional to the cloud mass above a surface density contour of  $116 \pm 28 M_{\odot} \text{ pc}^{-2}$  (Fig. 14), and the coefficient agrees well with the dense gas relations of Gao & Solomon (2004). Heiderman et al. (2010) studied the behavior of  $\Sigma(\text{SFR})$  on smaller scales using contours of extinction. They limited the YSOs to Class I and Flat SED objects to ensure that they were still closely related to their surrounding gas and found a steep increase in  $\Sigma(\text{SFR})$  with increasing  $\Sigma_{gas}$  up to about  $130 M_{\odot} \text{ pc}^{-2}$ , above which a turnover was suggested. By adding the dense clumps data from Wu et al. (2010a), they identified a turnover at  $129 \pm 14 M_{\odot} \text{ pc}^{-2}$ , where the  $\Sigma(\text{SFR})$  began to match the dense gas relation, but was far above

the K98 relation for total gas (Figure 15). The agreement between these two independent approaches is encouraging, suggesting that a contour of about  $125 \text{ M}_\odot \text{ pc}^{-2}$  is a reasonable defining level for a star-forming clump (§2.2). Other studies have found similar thresholds for efficient star formation or the presence of dense cores (Onishi et al. 1998; Enoch et al. 2007; Johnstone et al. 2004; André et al. 2010; Li et al. 1997; Lada 1992). Theoretical explanations for such thresholds can be found by considering magnetic support (Mouschovias & Spitzer 1976) or regulation by photo-ionization (McKee 1989). Alternatively, this threshold may simply correspond to the part of the cloud that is gravitationally bound (cf. §4.3).

The star formation rate density is even higher *within* clumps. Gutermuth et al. (2011) find a continuation of the steep increase in  $\Sigma(\text{SFR})$  to higher  $\Sigma_{\text{gas}}$  in a study including embedded clusters. They find that  $\Sigma(\text{SFR}) \propto \Sigma_{\text{gas}}^2$  up to several  $100 \text{ M}_\odot \text{ pc}^{-2}$ , with no evidence of a threshold. Near the centers of some centrally condensed clumps,  $\Sigma_{\text{gas}}$  reaches  $1 \text{ gm cm}^{-2}$ , or about  $4800 \text{ M}_\odot \text{ pc}^{-2}$  (Wu et al. 2010a), a threshold for the formation of massive stars suggested by theoretical analysis (Krumholz & McKee 2008).

Other studies have identified possible scaling relations in which SFR surface densities are not simply proportional to surface densities of dense gas. One analysis found that clouds forming stars with masses over  $10 \text{ M}_\odot$  satisfied the following relation:  $m(r) \geq 870 \text{ M}_\odot (r/\text{pc})^{1.33}$  (Kauffmann et al. 2010; Kauffmann & Pillai 2010), where  $m(r)$  is the enclosed mass as a function of radius. This is essentially a criterion they call “compactness”; it can be thought of as requiring a central condensation, with  $\rho(r) \propto r^p$ , with  $p \geq 1.67$ .

Dunham et al. (2011b) have compared a subset of clumps in the BGPS catalog (Aguirre et al. 2011; Rosolowsky et al. 2010) with kinematic distances to the Heiderman-Lada (HL) criterion for efficient star formation and to the Kauffman-Pillai (KP) criterion for massive star formation. About half the clumps satisfy both criteria. Interestingly, Dunham et al. (2011a) found that about half the BGPS sample contained at least one mid-infrared source from the GLIMPSE survey. For the clumps most securely identified with star formation, 70% to 80% satisfy the HL or KP criteria.

All these studies consistently show that  $\Sigma(\text{SFR})$ , especially for massive stars, is strongly localized to dense gas, and is much higher (for  $\Sigma_{\text{gas}} > 100 \text{ M}_\odot \text{ pc}^{-2}$ ) than in the extragalactic Schmidt relations (Kennicutt 1998b; Bigiel et al. 2008). This offset between the extragalactic and dense clump “Schmidt laws” can be straightforwardly understood as reflecting the mass fraction (or surface filling factor) of dense clumps in the star-forming ISM. If most or all star formation takes place in dense clumps, but the clumps contain only a small fraction of the total molecular gas, we would expect the characteristic star formation  $t_{\text{dep}}$  measured for clumps to be proportionally shorter than  $t_{\text{dep}}$  of the total cloud mass and the efficiency ( $\epsilon$ ) to be higher. Using a threshold of  $\text{C}^{18}\text{O}$  emission to define clumps, Higuchi et al. (2009) found that the star formation efficiency ( $\epsilon$ ) in clumps varies widely but averages 10%, about 4 times that in clouds as a whole (§4.1). If this interpretation is correct, we

would also expect the relations between SFR and dense gas mass for galaxies (Gao-Solomon relation) to be similar for galaxies and the clumps, and they indeed appear to be roughly consistent (Wu et al. 2005b).

This conclusion is subject to some caveats, however. Various authors (Krumholz & Thompson 2007; Narayanan et al. 2008; Juneau et al. 2009) have pointed out that lines like those of  $\text{HCN } J = 1 \rightarrow 0$  are not thermalized at lower densities, so can result in a linear relation even if the underlying star formation relation is a local version of a non-linear KS law that extends to much lower densities. The SFR vs dense gas relation is based on a correlation between total FIR and HCN luminosities, and  $L_{\text{FIR}}$  is likely to underestimate the SFR in young clusters (Urban et al. 2010; Gutermuth et al. 2011; Krumholz & Thompson 2007), perhaps by up to factors of 3–30. However, Lada et al. (2012) find a similar continuity between the Gao-Solomon starbursts and SFRs measured by counting YSOs in gas above a threshold surface density.

## 7. TOWARD A SYNTHESIS

### 7.1. Summary: Clues from Observations

Before we embark on an interpretation of the observed star formation law, it is useful to collect the main conclusions which can be drawn from the observations of star formation both outside and inside the Galaxy.

Beginning on the galactic scale ( $> 1 \text{ kpc}$ ), we can identify at least two and probably three distinct star formation regimes (Table 3). Whole galaxies may lie in one of these regimes, but a single galaxy may include two or three regimes.

#### 7.1.1. The Low-density Regime

The lowest-density regime (sometimes referred to as the sub-threshold regime), is most readily observed in the outer disks of spiral galaxies, but it also can be found in the interarm regions of some spiral galaxies and throughout the disks of some gas-poor galaxies. The solar neighborhood lies near the upper end of this low-density regime and the outer disk of the MW is clearly in this regime (§5.1).

The cold gas in these regions is predominantly atomic, though local concentrations of molecular gas are often found. Star formation is highly dispersed, with young clusters and H II regions only observed in regions of unusually high cold gas densities. The global “efficiency” of star formation,  $\epsilon'$  (defined in §1.2), or  $\Sigma(\text{SFR})/\Sigma_{\text{gas}}$ , is very low, and it is uncorrelated with  $\Sigma_{\text{gas}}$ . The steep, nearly vertical “Schmidt” relation seen in this regime (e.g., Fig. 12) mainly reflects lack of correlation over a region where the SFR has a much larger dynamic range than the local gas density; any apparent correlation is not physical. Recent stacking analysis of CO maps and studies of the outer MW suggest, however, that there may be a strong correlation with molecular surface density (§6, Schruba et al. 2011).

#### 7.1.2. The Intermediate-density Regime

The next, intermediate-density regime is roughly characterized by average gas surface densities of  $\Sigma_{\text{gas}} > 10 \text{ M}_\odot \text{ pc}^{-2}$ , corresponding roughly to  $N(\text{H}) \sim 10^{21} \text{ cm}^{-2}$ , or  $A_V \sim 1 \text{ mag}$ , for solar metallicity. The upper limit

to this regime is about  $\Sigma_{gas} \sim 100 - 300 \text{ M}_{\odot} \text{ pc}^{-2}$ , as discussed in the next section. The intermediate regime applies within the main optical radii ( $R_{25}$ ) of most gas-rich, late-type spiral and irregular galaxies. The “Galactic Ring” region of the Milky Way lies at the low end of this regime, while the CMZ may lie near the high end (§5.1).

The transition from the low-density regime roughly corresponds to the transition between H I-dominated and H<sub>2</sub>-dominated ISMs. Above  $\Sigma_{gas} = 10 \text{ M}_{\odot} \text{ pc}^{-2}$ , both the phase balance of the ISM and the form of the star formation law begin to change. The intermediate range features an increasing filling factor of molecular clouds, and star formation becomes more pervasive. The SFR surface density is strongly and tightly correlated with the cold gas surface density, whether expressed in terms of the total (atomic plus molecular) or only the molecular surface density. In most massive spiral galaxies, the cold gas in this regime is molecular-dominated. In low-mass and irregular galaxies, atomic gas can dominate, though this is somewhat dependent on the value of  $X(\text{CO})$  that is assumed. The characteristic depletion time ( $t_{dep}$  §1.2) for the interstellar gas is 1–2 Gyr (e.g., Bigiel et al. 2011).

When expressed in terms of  $\epsilon'$  (§1.2), the star formation rate per unit total gas mass, nearly all studies suggest that  $\epsilon'$  increases with gas surface density, with an exponent of 0.2–0.5, (the Schmidt law exponent,  $N - 1$ ). When measured against molecular mass (or surface density), some studies suggest  $\epsilon'$  is constant, but others suggest  $\epsilon'$  increasing systematically with surface density.

### 7.1.3. The High-density Regime

The two regimes discussed above were able to reproduce all of the early observations of the large-scale star formation law by Kennicutt (1989, 1998b) and Martin & Kennicutt (2001). However a number of recent observations suggest the presence of a third regime (and second transition) around  $\Sigma_{gas} > 100 - 300 \text{ M}_{\odot} \text{ pc}^{-2}$ , into what one might call the high-density, or starburst, regime. Around this value of  $\Sigma_{gas}$ , the interpretation of  $I(\text{CO})$  is likely to change (§2.4), and studies of local MW clouds indicate that a similar  $\Sigma_{gas}$  value may correspond to the theoretical notion of a cluster-forming clump, in which the SFR is much higher than in the rest of the cloud (§6.4). In the most extreme starburst galaxy environments, if standard values of  $X(\text{CO})$  are used, the average surface densities of gas (virtually all molecular) reach  $1000$  to  $10^4 \text{ M}_{\odot} \text{ pc}^{-2}$ , and the *volume* filling factor of clumps could reach unity (Wu et al. 2009). While the interpretation of molecular emission in these conditions warrants skepticism (§2.4, García-Burillo et al. 2012), the highest inferred surface density also corresponds to the densest parts of cluster forming clumps and the theoretical threshold of  $1 \text{ gm cm}^{-2}$  for efficient formation of massive stars (§4.3).

Some recent observations strongly hint at the existence of such a transition. As discussed in §6, luminous and ultraluminous starburst galaxies (and high-redshift SMGs) have characteristic ratios of  $L_{IR}/L(\text{CO})$  that are as much as 1–2 orders of magnitude higher than in normal galaxies, implying that at some point the SFR per molecular mass must increase dramatically. This could be explained by a break in the slope of the Schmidt law at

high densities, a continuous non-linear Schmidt law slope extending from the intermediate to high-density regimes, or a second mode of star formation in extreme starbursts with much higher “efficiency” ( $\epsilon'$ ). As discussed in §6.3, the constancy of the molecular  $\epsilon'$  at intermediate surface densities is uncertain. Observations of CO in high-redshift galaxies have been interpreted in terms of just such a bimodal Schmidt law (Daddi et al. 2010; Genzel et al. 2010). This interpretation rests on the assumption of a bimodality in  $X(\text{CO})$  (§6.1), and a change in  $\epsilon'$  that follows these changes in  $X(\text{CO})$ ; this is not entirely implausible, because the same physical changes in the ISM environment in the densest starbursts could affect both the CO conversion factor and  $\epsilon'$  if an increasing fraction of the gas is in dense clumps.

Both a Galactic value of  $X(\text{CO})$  in the starbursts and a much lower value have their disconcerting aspects. Applying a Galactic conversion factor produces total molecular masses which often exceed dynamical mass limits for the regions, whereas adopting values of  $X(\text{CO})$  which are factors of several lower produces gas consumption times as short as 10 Myr (Daddi et al. 2010; Genzel et al. 2010), with implications for the triggering and duty cycles of these massive starbursts.

The relations between SFR and ISM properties summarized above strictly refer to the correlations with the total cold gas surface density or in some cases the total H I and total H<sub>2</sub> densities; these are the relations of most interest for applications to galaxy modelling and cosmology. However the observational picture is quite different when we correlate the SFR with the supply of dense gas, as traced by HCN  $J = 1 \rightarrow 0$  and other dense clump tracers. Here there seems to be a single linear relation which extends across all of the SFR regimes described above, and which even extends to star-forming clouds in the Milky Way (Gao & Solomon 2004; Wu et al. 2005b; Gao et al. 2007; Lada et al. 2012). However, there is still some evidence of bimodality even if tracers of dense gas are used (García-Burillo et al. 2012), and physically based models, rather than simple conversion factors, are needed.

### 7.1.4. Clues from Studies of Molecular Clouds

The biggest hurdle one confronts when attempting to interpret these observations of galaxies is the severe influences of spatial averaging, both across the sky and along the line of sight. The star formation law relates surface densities of young stars and interstellar gas—already smoothed along the line of sight—averaged over linear dimensions ranging from order 100 pc to 50 kpc. These are 2–4 orders of magnitude larger than the sizes of the dense clump regions in which most stars form, and 4–8 orders of magnitude larger in terms of the surface areas being measured. This difference in scales means that the “surface densities” measured in extragalactic studies are really characterizing the filling factors of gas clumps and star-forming regions, rather than any measure of physical densities. Understanding how this “active component” of the star-forming ISM works is essential to even an empirical understanding of large-scale star formation, much less understanding its underlying physics. Detailed studies within the MW provide a way to “zoom in” further than is possible for other galaxies.

A common observed feature across all of the density

regimes observed in galaxies is that star formation takes place in molecular clouds. In the lowest-density regimes, clouds are rare and widely separated, but within individual molecular clouds in the MW, which can be probed in detail, the star formation seems to be indistinguishable from that in regions of somewhat higher average surface density (§5.1).

These observations also reveal that nearly all star formation within molecular clouds is highly localized, taking place in clumps, roughly defined by  $\Sigma_{mol} > 125 \text{ M}_{\odot} \text{ pc}^{-2}$ , or  $n > 10^4 \text{ cm}^{-3}$  (§6.4). The clumps host young stars, YSOs, and pre-stellar cores, the sites of individual star formation. This scale is as close to a deterministic environment for star formation as can be found. Once a pre-stellar core reaches substantial central condensation, about one-third of its mass will subsequently turn into young stars within a few Myr (Alves et al. 2007; Enoch et al. 2008). The relatively low global efficiencies (both  $\epsilon$  and  $\epsilon'$ ) within GMCs are largely a reflection of the low mass fraction in clumps and cores (§4.1). The star formation rate surface density in the clumps is 20-40 times that predicted for the mass surface density from the extragalactic Schmidt relation (§6.4), and this likewise can be largely understood as reflecting the low mass fraction of molecular gas in clumps and cores.

One might be tempted to identify the dense clumps within molecular clouds as a possible fourth density regime, in addition to the three regimes already discussed from observations of galaxies. However this would be very misleading, because so far as is currently known the formation of most stars in dense clumps is a common feature of star formation across all of the ISM environments in galaxies, extending from low-density sub-threshold disks to the most intense starbursts. The dense clump may well be the fundamental unit of massive, clustered star formation (Wu et al. 2005b). If this picture is correct, then the three regimes identified in galaxies and the order-of-magnitude increases in gas-to-star formation conversion rate across them must reflect changes in the fraction of the ISM that is converted to dense clumps, approaching 100% in the densest and most intense starbursts.

## 7.2. Some Speculations

The observations summarized in this review have stimulated a rich literature of theoretical ideas, models, and simulations aimed at explaining the observed star formation relations and constructing a coherent picture of galactic-scale star formation. Unfortunately we have neither the space nor the expertise to review that large body of theoretical work here. A review of many of the theoretical ideas can be found in McKee & Ostriker (2007), and an informative summary of the main models in the literature up to 2008 can be found in Leroy et al. (2008). Here we offer some speculations aimed toward explaining the observations and connecting the extragalactic and MW studies, and identifying directions for future work. Many of these speculations reflect ideas being discussed in the literature, and we make no claims for originality in the underlying concepts.

As mentioned in the introduction, the formation of stars represents the endpoint of a chain of physical processes that begins with cooling and infall of gas from the intergalactic medium onto disks, followed by the for-

mation of a cool atomic phase, contraction to gravitationally bound clouds, the formation of molecules and molecular clouds, the formation of dense clumps within those molecular clouds, and ultimately the formation of pre-stellar cores, stars, and star clusters. Although the beginning and end points of this process are relatively clear, the sequence of intermediate steps, in particular the respective roles of forming cool atomic gas, molecular gas, and bound clouds is unclear, and it is possible that different processes dominate in different galactic environments. By the same token, a variety of astrophysical time scales may be relevant: e.g., the free-fall time of the gas within clouds, the crossing time for a cloud, the free-fall time of the gas layer, or the dynamical time scales for the disc and spiral arm passages. Any of these timescales may be invoked for setting the time scale for star formation and the form of the star formation law. However one can construct two scenarios to explain the observations outlined in §7.1, which illustrate the boundaries of fully locally-driven versus globally-driven approaches. In some sense, these approaches are complementary, but they need to be brought together.

The first approach, which might be called a bottom-up picture, assumes that star formation is controlled locally within molecular clouds, (e.g., Krumholz & McKee 2005), building on what we observe in well-studied local regions of star formation. In this picture, one can identify three distinct regimes (§7.1), and associate the transitions between them to the crossing of two physically significant thresholds, the threshold for conversion of atomic to molecular gas, and the threshold for efficient star formation in a molecular cloud, identified with the theoretical notion of a clump (§2.2). In the purest form of this picture the SFR is driven completely by the amount and structure of the molecular gas. Current evidence from studies of nearby clouds indicates that the star formation rate scales linearly with the amount of dense gas in clumps (Lada et al. 2010), and this relation extends to starburst galaxies if the HCN emission is used as a proxy for the dense gas (Wu et al. 2005b; Lada et al. 2012). In this picture, the non-linear slope ( $N \sim 1.5$ ) of the global Schmidt relation would arise from either a decrease in the characteristic timescale (Krumholz et al. 2012) or by an increase in the fraction of gas above the clump threshold ( $f_{dense}$ ), from its typical value in local clouds [ $f_{dense} \sim 0.1$  (Lada et al. 2012)] with  $f_{dense} \propto \Sigma_{gas}^{0.5}$ .

The second approach, which we could call a top-down picture, assumes that star formation is largely controlled by global dynamical phenomena, such as disk instabilities (e.g., Silk 1997), and the dynamical timescales in the parent galaxy. In this picture the transition between the low-density and higher-density SFR regimes is mainly driven by gravitational instabilities in the disk rather than by cooling or molecular formation thresholds, and the non-linear increase in the SFR relative to gas density above this threshold reflects shorter self-gravitational timescales at higher density or the shorter dynamical timescales. In this picture there is no particular physical distinction between the intermediate-density and high-density regimes; in principle the same dynamical processes can regulate the SFR continuously across this wide surface density regime. Likewise it is the total surface density of gas, whether it be atomic or molecular,

that drives the SFR. The asymptotic form of this picture is a self-regulated star formation model: the disk adjusts to an equilibrium in which feedback from massive star formation acts to balance the hydrostatic pressure of the disk or to produce an equilibrium porosity of the ISM (e.g., Cox 1981; Dopita 1985; Silk 1997; Ostriker et al. 2010).

When comparing these pictures to the observations, each has its particular set of attractions and challenges. The bottom-up picture has the attraction of simplicity, associating nearly all of the relevant SFR physics with the formation of molecular gas and molecular cloud clumps. It naturally fits with a wide range of observations including the tight correlation of the SFR and molecular gas surface densities (e.g., Schruba et al. 2011 and references therein), the concentration of star formation within clouds in regions of dense gas (§4), and the observation of a linear relation between the dense gas traced by HCN emission and the total SFR in galaxies (§6). If the resolved star formation relation at intermediate surface densities is linear (§6, Bigiel et al. 2008),  $f_{dense}$  would be constant in that regime, while increasing monotonically with  $\Sigma_{gas}$  in the higher-density starburst regime with the transition occurring where  $\Sigma_{gas}$  derived from CO is similar to the threshold for dense gas. This picture does not explain why a particular galaxy or part of a galaxy lies in one of these regimes, a question perhaps best answered by the top-down picture.

Aspects of the top-down picture date back to early dynamical models of the ISM and the first observations of star formation thresholds in disks (e.g., Quirk & Tinsley 1973; Larson 1987; Zasov & Stmakov 1988; Kennicutt 1989; Elmegreen 1991; Silk 1997). There is some observational evidence for associating the observed low-density thresholds in disks with gravitational instabilities in the disk (e.g.,  $Q$  instabilities), rather than with atomic or molecular phase transitions (e.g., Kennicutt 1989; Martin & Kennicutt 2001), but recent observations and theoretical analyses have raised questions about this interpretation (e.g., Schaye 2004; Leroy et al. 2008). At higher surface densities the global relation between  $\Sigma(\text{SFR})$  and the ratio of gas density to local dynamical time ( $\Sigma_{gas}/\tau_{dyn}$ ) shows a correlation that is nearly as tight as the conventional Schmidt law (Kennicutt 1998b), and it also removes the double sequence of disks and starbursts that results if  $X(\text{CO})$  is systematically lower in the starbursts (§6, Daddi et al. 2010; Genzel et al. 2010). In this picture, the higher star formation rate for a given gas surface density in mergers is caused by the compaction of the gas and the resulting shorter rotation period. However, the efficiency per orbital period is not clearly explained in this picture. Theories of feedback-regulated star formation show promise in explaining the low efficiency per orbit in normal galaxies (Kim et al. 2011), and they may also explain the less effective role of negative feedback in merger-driven starbursts (e.g., Ostriker & Shetty 2011). This model does not extend to cloud-level star formation. If feedback from massive stars is fundamental, the similarity between the efficiency in local clouds forming only low mass stars and regions with strong feedback from massive stars (cf. Evans et al. 2009 and Murray 2011) remains a mystery.

Both of these scenarios can claim some successes, but neither provides a complete explanation that extends

over all scales and environments. As but one example, the large changes in the present-day SFRs and past star formation histories of galaxies as functions of galaxy mass and type may well be dictated mainly by external influences such as the accretion history of cold gas from the cosmic web and intergalactic medium. Neither the bottom-up or top-down pictures as articulated above incorporate these important physical processes. On smaller scales a complete model for star formation may combine features of both scenarios. The dynamical picture is quite attractive on the scales of galaxies, and it would be interesting to extend it to smaller scales. In doing so, the question of what to use for  $\tau_{dyn}$  arises. The galaxy rotation period cannot control star formation in individual clouds, so a more local dynamical time is needed. One option is the cloud or clump crossing time (essentially the size over the velocity dispersion) (Elmegreen 2000), which may be particularly relevant in regions of triggered star formation. Since clumps are the star forming units, their crossing times may be the more relevant quantities.

A popular option is the free-fall time (e.g., Krumholz & McKee 2005). Since  $t_{ff} \propto \rho^{-0.5}$ , a volumetric star formation law,  $\rho_{\text{SFR}} \propto \rho/t_{ff} \propto \rho^{1.5}$ , where  $\rho$  is the gas density, is a tempting rule. With this rule, the roughly 1.5 power of the KS relation appears to be explained if we ignore the difference between volume and surface density. Indeed, Krumholz et al. (2012) argue that such a volumetric law reproduces observations from the scale of nearby clouds to starburst galaxies. However, the definition of  $t_{ff}$  changes for compact starbursts (see eq. 9 in their paper), essentially at the boundary between the intermediate-density and high-density regimes discussed in §7.1. Including the atomic-molecular threshold, as treated in Krumholz et al. (2009b), clarifies that this “scale-free” picture implicitly recognizes the same three regimes discussed in §7.1.

Theories that rely on  $t_{ff}$  face two problems. First, no evidence has been found in well-studied molecular clouds for collapse at  $t_{ff}$  (§4.3, e.g., Zuckerman & Evans 1974). To match observations, an “efficiency” of about 0.01 must be inserted. Why the star formation density should remain proportional to  $t_{ff}$ , while being slowed by a factor of 100, is a challenging theoretical question. Studies of the role of turbulence show some promise in explaining this paradox (Krumholz & McKee 2005; Hennebelle & Chabrier 2011), and magnetic fields may yet play a role.

The second problem is how to calculate a relevant  $t_{ff}$  in a cloud, much less a galaxy, with variations in  $\rho$  by many orders of magnitude, and much of the gas unlikely to be gravitationally bound. For example, Krumholz et al. (2012) calculate  $t_{ff}$  from the mean density of the whole cloud ( $t_{ff} \propto 1/\langle\rho\rangle$ ). A computation of  $\langle t_{ff} \rangle$  from  $\langle 1/\rho \rangle$  would emphasize the densest gas, where star formation is observed to occur. In a model that accounts for this, Hennebelle & Chabrier (2011) reproduce at some level the observations of surface density thresholds for efficient star formation observed in nearby clouds (Lada et al. 2010; Heiderman et al. 2010). An alternative view to the models involving  $t_{ff}$  and emphasizing instead the critical role of the dense gas threshold can be found in Lada et al. (2012). Because both models claim to apply to cloud-level star formation, observations of MW clouds



should be able to test them.

### 7.3. Future Prospects

We hope that this review has conveyed the tremendous progress over the last decade in understanding the systematic behavior of star formation, both in the MW and in other galaxies. As often happens when major observational advances are made, observational pictures that once seemed simple and certain have proven to be more complex and uncertain. We have attempted to inject a dose of skepticism about some well-accepted truisms and to highlight important questions where even the observations do not present a completely consistent picture.

As we return to the key questions outstanding in this subject (§1.3), a few clear themes emerge, many of which lie at the cusp between MW and extragalactic observations, and between theory and simulation on the sub-cloud scale on the one hand, and the galactic and cosmological scales on the other. The recent observations within the MW of a near-universal association of stars with dense molecular clumps (§6.4) offers the potential key of a fundamental sub-unit of high-efficiency star formation in all galactic environments, from the low-density and quiescent environments of outer disks and dwarf galaxies to the most intense starbursts. However this hypothesis needs to be validated observationally in a wider range of environments. Restated from another perspective, we need much better information on the structure (physical structure, substructure) and dynamics of star-forming clouds across the full range of star-forming environments found in galaxies today.

Fortunately we are on the brink of major progress on multiple fronts. One approach is to assemble more complete and “zoomed-out” views of the MW, while preserving the unparalleled spatial resolution and sensitivity of MW observations to fully characterise the statistical trends in cloud structure, kinematics, mass spectra, and associated star formation for complete, unbiased, and physically diverse samples. In the near-term, *Herschel* surveys will deliver images of nearby clouds, the plane of the MW, and many galaxies in bands from 60 to 500  $\mu\text{m}$ . When the MW plane data are combined with higher resolution surveys of the MW at 0.87 to 1.1 mm from ground-based telescopes, spectroscopic follow-up, and improved distances from ongoing VLBA studies, we will have a much improved and nuanced picture of the gas in the MW, which can then provide a more useful template for understanding similar galaxies. Recent surveys have doubled the number of known H II regions in the MW (Anderson et al. 2011), allowing study of a wider range of star formation outcomes. Tests of the limitations on star formation rate tracers used in extragalactic work will be possible, as will comparisons to KS relations on a variety of spatial scales. The Magellanic Clouds also offer great potential for extending this approach to two sets of environments with different metallicities, ISM environments, and star formation properties (exploiting for example the 30 Doradus region).

This expanded information from MW surveys will then need to be combined with more sensitive and “zoomed-in” observations of other galaxies. For such studies the weakest link currently is the knowledge of the molecular gas. We can trace H I and SFRs to much lower levels than we can detect CO, even with stacking of the

CO maps. When fully commissioned, *ALMA* will have a best resolution of about 13 mas at 300 GHz (0.5 pc at the distance of M51), and about 8 times the total collecting area of any existing millimeter facility, allowing us to trace molecular emission to deeper levels and/or to obtain resolution at least 10 times better than the best current studies. It may be possible to study dense structures within molecular clouds in other galaxies for comparison to dense clumps in the MW clouds. To be most effective, these programs will need to expand beyond the typical surveys in one or two CO rotational transitions to include the high-density molecular tracers and ideally a ladder of tracers with increasing excitation and/or critical density. Continuum observations will gain even more because of large bandwidths and atmospheric stability. Maps of mm-wave dust emission may become the preferred method to trace the gas in other galaxies, as they are becoming already in the MW, bypassing the issues of  $X(\text{CO})$ . Observations of radio recombination lines may also provide alternative tracers of star formation rate in highly obscured regions. It is difficult to exaggerate the potential transformational power of *ALMA* for this subject.

For molecular line observations of nearby galaxies, large single dishes (the Nobeyama 45-m, the IRAM 30-m, and the future CCAT), along with the smaller millimeter arrays, IRAM PdB and CARMA, will provide complementary characterization of the molecular and dense gas on larger scales than can be efficiently surveyed with *ALMA*. A substantial expansion of the IRAM interferometer (NOEMA) will provide complementary advances in sensitivity in the northern hemisphere. This subject will also advance with a substantial expansion of H I mapping (by e.g., the EVLA) to expand the range of environments probed and ideally to attain spatial resolutions comparable to the rapidly improving molecular line observations. Although it is likely that star formation on the local scale concentrates in molecular-dominated regions, the formation of this molecular gas from atomic gas remains a critical (and possibly controlling) step in the entire chain that leads from gas to stars.

Future opportunities also await for improving our measurements of SFRs in galaxies, though the truly transformational phase of that subject may already be passing with the end of the ISO, Spitzer, GALEX, and *Herschel* eras. *HST* continues to break new ground, especially in direct mapping of young stars and their ages via resolved color-magnitude diagrams. *Herschel* surveys of nearby galaxies will provide far-infrared data, complementary to the other wavelength regions that trace star formation (§3), and multiband imaging with the EVLA will allow better separation of non-thermal from the free-free continuum emission, which directly traces the ionization rate and massive SFR. *SOFIA* offers the opportunity for mapping the brightest regions of star formation with higher spatial and spectral resolution than Spitzer. Further into the future, major potential lies with *JWST*, which will vastly improve our capabilities for tracing star formation via infrared radiation, both on smaller scales in nearby galaxies and in very distant galaxies. *SPICA* may provide complementary capability at longer wavelengths. As highlighted in §1.3, key unknowns in this subject include robust constraints on the ages and lifetimes of star-forming clouds; observations of resolved star

clusters, both in the MW and nearby galaxies, offer potential for considerable inroads in this problem.

A number of the questions we have listed also can be attacked with groundbased OIR observations. As discussed in §3.9, despite the availability now of spatially-resolved multi-wavelength observations of nearby galaxies, we still do not have an absolutely reliable way to measure dust-corrected SFRs, especially from short-lived tracers that are critical for exploring the local Schmidt law. For observations of normal galaxies where local attenuations are modest, integral-field mapping of galaxies offers the means to produce high-quality  $H\alpha$  maps corrected for dust using the Balmer decrement (e.g., Blanc et al. 2009, 2010; Sánchez et al. 2012). A “gold standard” for such measurements also is available in the hydrogen recombination lines of the Paschen and Brackett series in the near-infrared. The emissivities of these lines are directly related to ionizing luminosities in the same way as are the more widely applied Balmer lines (albeit with somewhat stronger density and temperature dependences), and these lines suffer much lower dust attenuation (readily calibrated by comparing to  $H\alpha$  or other shorter wavelength lines). These lines are much fainter, however, and are subject to strong interference from telluric OH emission (and thermal emission at longer wavelengths). Continuing advances in near-infrared detectors have now brought many of these lines into the accessible range, and soon we should begin to see large-scale surveys that will provide high-resolution emission maps and robust “SFR maps”, at least on spatial scales larger than individual H II regions. These maps in turn can be used to test and hopefully recalibrate other dust-free tracers such as combinations of infrared dust emission with UV and optical emission-line maps. Looking further ahead, spectral imaging in the near-infrared (and with  $H\alpha$  in the visible) with massively parallel integral-field spectrometers will provide more precise and full views of star formation.

The current, pioneering studies of star formation at  $z \sim 1 - 3$  will become much easier with new instrumentation. Advances in submillimeter array technology (e.g., SCUBA-2 on the JCMT) and larger dishes at very high altitude, such as CCAT, will allow deep and wide searches for dust continuum emission from distant galaxies. Many of the biases in current samples can be alleviated and a more complete picture of star formation through cosmic time can be constructed. Huge surveys of Ly $\alpha$  emitting galaxies will be undertaken to constrain dark energy, providing as a by-product, nearly a million star-forming galaxies at  $1.9 < z < 3.5$  and a large number of [OII] emitting galaxies for  $z < 0.5$  (e.g., Hill et al. 2008).

Since the theoretical side of the subject lies outside the scope of this review, we comment only briefly on this area. Numerical simulations are poised to make major contributions to the subject over the next several years. Simulations with higher resolution and more sophisticated treatments of the heating, cooling, phase balance, and feedback are providing deeper insights into

the physical nature of the star formation scaling laws and thresholds and the life cycles of molecular clouds (e.g., Robertson & Kravtsov 2008; Dobbs 2008; Dobbs & Pringle 2010; Tasker & Tan 2009; Tasker 2011; Brooks et al. 2011). Inclusion of realistic stellar feedback may obviate the need for artificial constraints on efficiency (e.g., Hopkins et al. 2011).

Analytical models which incorporate the wide range of relevant physical processes on the scales of both molecular clouds and galactic disks are also leading to deeper insights into the triggering and regulation of star formation on the galactic scale (e.g., Ostriker et al. 2010, and papers cited in §7.2). Exploring different prescriptions for cloud-scale star formation in galaxy evolution models will illuminate the effects of the cloud-scale prescription on galaxy-scale evolution. At the “micro-scale” of molecular clouds, inclusion of radiative and mechanical feedback from star formation is producing more realistic models, and perhaps the relative importance of feeding from the local core and from the greater clump may be quantified (e.g., references in §4.3).

We conclude with a hope and a prediction. From the start, this review was designed to exchange ideas between those studying star formation in the Milky Way and those studying star formation in other galaxies. The authors have benefited immensely from this exchange, and we hope for more of this cross-talk between our two communities: people studying star formation within the Milky Way can put their results in a larger context; those studying other galaxies can appreciate that our home galaxy offers unique advantages for understanding galaxies. A common theme across both arenas has been the rapid pace of advance, both in observations and theory. When the next review of this subject is written, we predict that it will focus on observational tests of detailed physical theories and simulations rather than on empirical star formation laws. We conclude with heartfelt thanks to all of those who are working toward this common goal.

We would like to acknowledge the many people who have supplied information and preprints in advance of publication. In addition, we thank Alberto Bolatto, Leonardo Bronfman, Peter Kaberla, Jin Koda, Adam Leroy, Yancy Shirley, and Linda Tacconi for useful and stimulating discussions. Henrik Beuther, Guillermo Blanc, Daniela Calzetti, Barbara Catinella, Reinhard Genzel, Rob Gutermuth, Mark Krumholz, Charles Lada, Fred Lo, Steve Longmore, Eve Ostriker, and Jim Pringle provided valuable comments on an early draft. We both would like to express special thanks to our current and former students and postdocs, with whom we have shared countless valuable discussions. NJE thanks the Institute of Astronomy, Cambridge, and the European Southern Observatory, Santiago, for hospitality during extended visits, during which much of his work on the review was done. NJE also acknowledges support from NSF Grant AST-1109116 to the University of Texas at Austin.

#### REFERENCES

- Abdo, A. A., Ackermann, M., Ajello, M., et al. 2010, *ApJ*, 710, 133
- Aguirre, J. E., Ginsburg, A. G., Dunham, M. K., et al. 2011, *ApJS*, 192, 4

- Allen, L., Megeath, S. T., Gutermuth, R., et al. 2007, *Protostars and Planets V*, 361
- Allers, K. N., Kessler-Silacci, J. E., Cieza, L. A., & Jaffe, D. T. 2006, *ApJ*, 644, 364
- Alonso-Herrero, A., Rieke, G. H., Rieke, M. J., et al. 2006, *ApJ*, 650, 835
- Altenhoff, W. J., Downes, D., Goad, L., Maxwell, A., & Rinehart, R. 1970, *A&AS*, 1, 319
- Alves, J., Lombardi, M., & Lada, C. J. 2007, *A&A*, 462, L17
- Anderson, L. D., Bania, T. M., Balser, D. S., & Rood, R. T. 2011, *ApJS*, 194, 32
- André, P., Men'shchikov, A., Bontemps, S., et al. 2010, *A&A*, 518, L102
- André, P., Ward-Thompson, D., & Barsony, M. 1993, *ApJ*, 406, 122
- Arce, H. G., Shepherd, D., Gueth, F., et al. 2007, *Protostars and Planets V*, 245
- Armus, L., Charmandaris, V., Bernard-Salas, J., et al. 2007, *ApJ*, 656, 148
- Atek, H., Kunth, D., Schaerer, D., et al. 2009, *A&A*, 506, L1
- Bacmann, A., André, P., Puget, J.-L., et al. 2000, *A&A*, 361, 555
- Baldry, I. K., Balogh, M. L., Bower, R. G., et al. 2006, *MNRAS*, 373, 469
- Baldry, I. K., Glazebrook, K., Brinkmann, J., et al. 2004, *ApJ*, 600, 681
- Bally, J., Aguirre, J., Battersby, C., et al. 2010, *ApJ*, 721, 137
- Baraffe, I. & Chabrier, G. 2010, *A&A*, 521, A44
- Baraffe, I., Chabrier, G., & Gallardo, J. 2009, *ApJ*, 702, L27
- Barnard, E. E. 1908, *Astronomische Nachrichten*, 177, 231
- Bastian, N., Covey, K. R., & Meyer, M. R. 2010, *ARA&A*, 48, 339
- Bate, M. R. 2009, *MNRAS*, 397, 232
- Bate, M. R., Bonnell, I. A., & Bromm, V. 2003, *MNRAS*, 339, 577
- Bauer, F. E., Alexander, D. M., Brandt, W. N., et al. 2002, *AJ*, 124, 2351
- Begum, A., Chengalur, J. N., Karachentsev, I. D., Sharina, M. E., & Kaisin, S. S. 2008, *MNRAS*, 386, 1667
- Bell, E. F. 2003, *ApJ*, 586, 794
- Bell, E. F. & Kennicutt, Jr., R. C. 2001, *ApJ*, 548, 681
- Bell, E. F., Papovich, C., Wolf, C., et al. 2005, *ApJ*, 625, 23
- Beltrán, M. T., Brand, J., Cesaroni, R., et al. 2006, *A&A*, 447, 221
- Bendo, G. J., Draine, B. T., Engelbracht, C. W., et al. 2008, *MNRAS*, 389, 629
- Benjamin, R. A., Churchwell, E., Babler, B. L., et al. 2005, *ApJ*, 630, L149
- Bergin, E. A. & Tafalla, M. 2007, *ARA&A*, 45, 339
- Beuther, H., Churchwell, E. B., McKee, C. F., & Tan, J. C. 2007a, *Protostars and Planets V*, 165
- Beuther, H., Leurini, S., Schilke, P., et al. 2007b, *A&A*, 466, 1065
- Beuther, H., Schilke, P., Menten, K. M., et al. 2002, *ApJ*, 566, 945
- Beuther, H., Tackenberg, J., Linz, H., et al. 2012, *ApJ*, 747, 43
- Bigiel, F., Leroy, A., Walter, F., et al. 2010, *AJ*, 140, 1194
- Bigiel, F., Leroy, A., Walter, F., et al. 2008, *AJ*, 136, 2846
- Bigiel, F., Leroy, A. K., Walter, F., et al. 2011, *ApJ*, 730, L13
- Blanc, G. A. 2010, in *From Stars to Galaxies: Connecting our Understanding of Star and Galaxy Formation*, University of Florida, Gainesville, Florida, USA, 7-10 April 2010. Online at <http://conference.astro.ufl.edu/STARSTOGALAXIES>, id.153
- Blanc, G. A., Adams, J. J., Gebhardt, K., et al. 2011, *ApJ*, 736, 31
- Blanc, G. A., Gebhardt, K., Heiderman, A., et al. 2010, in *Astronomical Society of the Pacific Conference Series*, Vol. 432, *New Horizons in Astronomy: Frank N. Bash Symposium 2009*, ed. L. M. Stanford, J. D. Green, L. Hao, & Y. Mao, 180
- Blanc, G. A., Heiderman, A., Gebhardt, K., Evans, II, N. J., & Adams, J. 2009, *ApJ*, 704, 842
- Blanton, M. R., Lupton, R. H., Schlegel, D. J., et al. 2005, *ApJ*, 631, 208
- Blitz, L., Fukui, Y., Kawamura, A., et al. 2007, *Protostars and Planets V*, 81
- Blitz, L. & Rosolowsky, E. 2006, *ApJ*, 650, 933
- Bloemen, H. 1989, *ARA&A*, 27, 469
- Bohlin, R. C., Savage, B. D., & Drake, J. F. 1978, *ApJ*, 224, 132
- Boissier, S., Prantzos, N., Boselli, A., & Gavazzi, G. 2003, *MNRAS*, 346, 1215
- Bok, B. J. & Reilly, E. F. 1947, *ApJ*, 105, 255
- Bolatto, A. D., Leroy, A. K., Jameson, K., et al. 2011, *ApJ*, 741, 12
- Bonnell, I. A., Bate, M. R., & Vine, S. G. 2003, *MNRAS*, 343, 413
- Bonnell, I. A., Larson, R. B., & Zinnecker, H. 2007, *Protostars and Planets V*, 149
- Boquien, M., Buat, V., Boselli, A., et al. 2012, *A&A*, 539, A145
- Boquien, M., Calzetti, D., Combes, F., et al. 2011, *AJ*, 142, 111
- Boselli, A., Gavazzi, G., Lequeux, J., & Pierini, D. 2002, *A&A*, 385, 454
- Boss, A. P. & Yorke, H. W. 1995, *ApJ*, 439, L55
- Bothwell, M. S., Kenicutt, R. C., Johnson, B. D., et al. 2011, *MNRAS*, 415, 1815
- Bothwell, M. S., Kennicutt, R. C., & Lee, J. C. 2009, *MNRAS*, 400, 154
- Bouché, N., Cresci, G., Davies, R., et al. 2007, *ApJ*, 671, 303
- Bressert, E., Bastian, N., Gutermuth, R., et al. 2010, *MNRAS*, 409, L54
- Brinchmann, J., Charlot, S., White, S. D. M., et al. 2004, *MNRAS*, 351, 1151
- Brogan, C. L., Hunter, T. R., Cyganowski, C. J., et al. 2009, *ApJ*, 707, 1
- Bronfman, L., Casassus, S., May, J., & Nyman, L.-Å. 2000, *A&A*, 358, 521
- Bronfman, L., Cohen, R. S., Alvarez, H., May, J., & Thaddeus, P. 1988, *ApJ*, 324, 248
- Bronfman, L., Nyman, L.-Å., & May, J. 1996, *A&AS*, 115, 81
- Brooks, A. M., Solomon, A. R., Governato, F., et al. 2011, *ApJ*, 728, 51
- Brunthaler, A., Reid, M. J., Menten, K. M., et al. 2011, *Astronomische Nachrichten*, 332, 461
- Buat, V., Donas, J., Milliard, B., & Xu, C. 1999, *A&A*, 352, 371
- Buat, V., Iglesias-Páramo, J., Seibert, M., et al. 2005, *ApJ*, 619, L51
- Burgarella, D., Buat, V., & Iglesias-Páramo, J. 2005, *MNRAS*, 360, 1413
- Burton, W. B. 1988, *The structure of our Galaxy derived from observations of neutral hydrogen*, ed. K. I. Kellermann & G. L. Verschuur, 295-358
- Calzetti, D., Chandar, R., Lee, J. C., et al. 2010a, *ApJ*, 719, L158
- Calzetti, D., Kennicutt, R. C., Engelbracht, C. W., et al. 2007, *ApJ*, 666, 870
- Calzetti, D., Kinney, A. L., & Storchi-Bergmann, T. 1994, *ApJ*, 429, 582
- Calzetti, D., Wu, S.-Y., Hong, S., et al. 2010b, *ApJ*, 714, 1256
- Carey, S. J., Noriega-Crespo, A., Mizuno, D. R., et al. 2009, *PASP*, 121, 76
- Casassus, S., Bronfman, L., May, J., & Nyman, L.-Å. 2000, *A&A*, 358, 514
- Catinella, B., Schiminovich, D., Kauffmann, G., et al. 2010, *MNRAS*, 403, 683
- Cervino, M., Luridiana, V., Pérez, E., Vilchez, J. M., & Valls-Gabaud, D. 2003, *A&A*, 407, 177
- Cesaroni, R., Palagi, F., Felli, M., et al. 1988, *A&AS*, 76, 445
- Chabrier, G. 2003, *PASP*, 115, 763
- Chabrier, G. & Baraffe, I. 2000, *ARA&A*, 38, 337
- Chandar, R., Whitmore, B. C., Calzetti, D., et al. 2011, *ApJ*, 727, 88
- Chapman, N. L., Mundy, L. G., Lai, S.-P., & Evans, II, N. J. 2009, *ApJ*, 690, 496
- Chapman, S. C., Blain, A. W., Smail, I., & Ivison, R. J. 2005, *ApJ*, 622, 772
- Charlot, S. & Fall, S. M. 2000, *ApJ*, 539, 718
- Chen, C.-H. R., Indebetouw, R., Chu, Y.-H., et al. 2010, *ApJ*, 721, 1206
- Chomiuk, L. & Povich, M. S. 2011, *AJ*, 142, 197
- Christlein, D., Zaritsky, D., & Bland-Hawthorn, J. 2010, *MNRAS*, 405, 2549
- Churchwell, E., Babler, B. L., Meade, M. R., et al. 2009, *PASP*, 121, 213
- Clark, P. C., Klessen, R. S., & Bonnell, I. A. 2007, *MNRAS*, 379, 57
- Clemens, D. P. & Barvainis, R. 1988, *ApJS*, 68, 257
- Clemens, D. P., Sanders, D. B., & Scoville, N. Z. 1988, *ApJ*, 327, 139
- Colbert, E. J. M., Heckman, T. M., Ptak, A. F., Strickland, D. K., & Weaver, K. A. 2004, *ApJ*, 602, 231
- Combes, F., Young, L. M., & Bureau, M. 2007, *MNRAS*, 377, 1795
- Condon, J. J. 1992, *ARA&A*, 30, 575
- Cortese, L., Boselli, A., Franzetti, P., et al. 2008, *MNRAS*, 386, 1157
- Cox, D. P. 1981, *ApJ*, 245, 534
- Cox, D. P. 2005, *ARA&A*, 43, 337
- Crapci, A., van Dishoeck, E. F., Hogerheijde, M. R., Pontoppidan, K. M., & Dullemond, C. P. 2008, *A&A*, 486, 245
- Crocker, A. F., Bureau, M., Young, L. M., & Combes, F. 2011, *MNRAS*, 410, 1197
- Crothwaite, L. P. & Turner, J. L. 2007, *AJ*, 134, 1827
- Crowther, P. A., Schnurr, O., Hirschi, R., et al. 2010, *MNRAS*, 408, 731
- Crutcher, R. M., Wandelt, B., Heiles, C., Falgarone, E., & Tröland, T. H. 2010, *ApJ*, 725, 466
- Da Rio, N., Robberto, M., Hillenbrand, L. A., Henning, T., & Stassun, K. G. 2012, *ApJ*, 748, 14
- Daddi, E., Elbaz, D., Walter, F., et al. 2010, *ApJ*, 714, L118
- Dalcanton, J. J., Williams, B. F., Seth, A. C., et al. 2009, *ApJS*, 183, 67

- Dale, D. A., Bendo, G. J., Engelbracht, C. W., et al. 2005, *ApJ*, 633, 857
- Dale, D. A., Cohen, S. A., Johnson, L. C., et al. 2009, *ApJ*, 703, 517
- Dale, D. A., Gil de Paz, A., Gordon, K. D., et al. 2007, *ApJ*, 655, 863
- Dale, D. A. & Helou, G. 2002, *ApJ*, 576, 159
- Dale, D. A., Smith, J. D. T., Armus, L., et al. 2006, *ApJ*, 646, 161
- Dame, T. M., Hartmann, D., & Thaddeus, P. 2001, *ApJ*, 547, 792
- Dame, T. M. & Thaddeus, P. 2011, *ApJ*, 734, L24
- Davies, B., Bastian, N., Gieles, M., et al. 2011, *MNRAS*, 411, 1386
- de Wit, W. J., Testi, L., Palla, F., & Zinnecker, H. 2005, *A&A*, 437, 247
- Dekel, A. & Birnboim, Y. 2006, *MNRAS*, 368, 2
- di Francesco, J., Evans, II, N. J., Caselli, P., et al. 2007, *Protostars and Planets V*, 17
- Dickey, J. M., McClure-Griffiths, N. M., Gaensler, B. M., & Green, A. J. 2003, *ApJ*, 585, 801
- Dickman, R. L. 1978, *ApJS*, 37, 407
- Dickman, R. L., Snell, R. L., & Schloerb, F. P. 1986, *ApJ*, 309, 326
- Dobbs, C. L. 2008, *MNRAS*, 391, 844
- Dobbs, C. L., Burkert, A., & Pringle, J. E. 2011, *MNRAS*, 413, 2935
- Dobbs, C. L. & Pringle, J. E. 2010, *MNRAS*, 409, 396
- Dohm-Palmer, R. C., Skillman, E. D., Mateo, M., et al. 2002, *AJ*, 123, 813
- Dolphins, A. E. 2002, *MNRAS*, 332, 91
- Dopita, M. A. 1985, *ApJ*, 295, L5
- Dopita, M. A., Pereira, M., Kewley, L. J., & Capaccioli, M. 2002, *ApJS*, 143, 47
- Dopita, M. A. & Ryder, S. D. 1994, *ApJ*, 430, 163
- Downes, D. & Solomon, P. M. 1998, *ApJ*, 507, 615
- Downes, D., Solomon, P. M., & Radford, S. J. E. 1993, *ApJ*, 414, L13
- Draine, B. T. 2003, *ARA&A*, 41, 241
- Draine, B. T. 2011, *Physics of the Interstellar and Intergalactic Medium*
- Dunham, M. K., Robitaille, T. P., Evans, II, N. J., et al. 2011a, *ApJ*, 731, 90
- Dunham, M. K., Rosolowsky, E., Evans, II, N. J., Cyganowski, C., & Urquhart, J. S. 2011b, *ApJ*, 741, 110
- Dunham, M. M., Evans, II, N. J., Terebey, S., Dullemond, C. P., & Young, C. H. 2010, *ApJ*, 710, 470
- Eales, S. A., Smith, M. W. L., Wilson, C. D., et al. 2010, *A&A*, 518, L62
- Egan, M. P., Shipman, R. F., Price, S. D., et al. 1998, *ApJ*, 494, L199
- Elbaz, D., Le Floc'h, E., Dole, H., & Marcellac, D. 2005, *A&A*, 434, L1
- Elmegreen, B. G. 1991, *ApJ*, 378, 139
- Elmegreen, B. G. 2000, *ApJ*, 530, 277
- Elmegreen, B. G. & Efremov, Y. N. 1997, *ApJ*, 480, 235
- Elmegreen, B. G. & Parravano, A. 1994, *ApJ*, 435, L121
- Engargiola, G., Plambeck, R. L., Rosolowsky, E., & Blitz, L. 2003, *ApJS*, 149, 343
- Engelbracht, C. W., Gordon, K. D., Rieke, G. H., et al. 2005, *ApJ*, 628, L29
- Enoch, M. L., Evans, II, N. J., Sargent, A. I., & Glenn, J. 2009, *ApJ*, 692, 973
- Enoch, M. L., Evans, II, N. J., Sargent, A. I., et al. 2008, *ApJ*, 684, 1240
- Enoch, M. L., Glenn, J., Evans, II, N. J., et al. 2007, *ApJ*, 666, 982
- Evans, II, N. J. 1999, *ARA&A*, 37, 311
- Evans, II, N. J., Dunham, M. M., Jørgensen, J. K., et al. 2009, *ApJS*, 181, 321
- Evans, II, N. J., Rawlings, J. M. C., Shirley, Y. L., & Mundy, L. G. 2001, *ApJ*, 557, 193
- Falgarone, E., Phillips, T. G., & Walker, C. K. 1991, *ApJ*, 378, 186
- Farrah, D., Bernard-Salas, J., Spoon, H. W. W., et al. 2007, *ApJ*, 667, 149
- Faúndez, S., Bronfman, L., Garay, G., et al. 2004, *A&A*, 426, 97
- Feldmann, R., Gnedin, N. Y., & Kravtsov, A. V. 2012, *ApJ*, 747, 124
- Ferguson, A. M. N., Wyse, R. F. G., Gallagher, J. S., & Hunter, D. A. 1998, *ApJ*, 506, L19
- Field, G. B., Goldsmith, D. W., & Habing, H. J. 1969, *ApJ*, 155, L149
- Flaherty, K. M., Pipher, J. L., Megeath, S. T., et al. 2007, *ApJ*, 663, 1069
- Förster Schreiber, N. M., Genzel, R., Bouché, N., et al. 2009, *ApJ*, 706, 1364
- Förster Schreiber, N. M., Roussel, H., Sauvage, M., & Charmandaris, V. 2004, *A&A*, 419, 501
- Foster, J. B., Jackson, J. M., Barnes, P. J., et al. 2011, *ApJS*, 197, 25
- Frerking, M. A., Langer, W. D., & Wilson, R. W. 1982, *ApJ*, 262, 590
- Fukui, Y. & Kawamura, A. 2010, *ARA&A*, 48, 547
- Fukui, Y., Mizuno, N., Yamaguchi, R., Mizuno, A., & Onishi, T. 2001, *PASJ*, 53, L41
- Fuller, G. A., Williams, S. J., & Sridharan, T. K. 2005, *A&A*, 442, 949
- Fumagalli, M., da Silva, R. L., & Krumholz, M. R. 2011, *ApJ*, 741, L26
- Gallego, J., Zamorano, J., Aragon-Salamanca, A., & Rego, M. 1995, *ApJ*, 455, L1
- Gao, Y., Carilli, C. L., Solomon, P. M., & Vanden Bout, P. A. 2007, *ApJ*, 660, L93
- Gao, Y. & Solomon, P. M. 2004, *ApJ*, 606, 271
- García-Burillo, S., Usero, A., Alonso-Herrero, A., et al. 2012, *A&A*, 539, A8
- Gavazzi, G., Boselli, A., Donati, A., Franzetti, P., & Scodreggio, M. 2003, *A&A*, 400, 451
- Gavazzi, G. & Scodreggio, M. 1996, *A&A*, 312, L29
- Genzel, R., Burkert, A., Bouché, N., et al. 2008, *ApJ*, 687, 59
- Genzel, R., Lutz, D., Sturm, E., et al. 1998, *ApJ*, 498, 579
- Genzel, R., Newman, S., Jones, T., et al. 2011, *ApJ*, 733, 101
- Genzel, R., Tacconi, L. J., Gracia-Carpio, J., et al. 2010, *MNRAS*, 407, 2091
- Gieles, M., Larsen, S. S., Bastian, N., & Stein, I. T. 2006, *A&A*, 450, 129
- Gies, D. R. 1987, *ApJS*, 64, 545
- Gil de Paz, A., Boissier, S., Madore, B. F., et al. 2007, *ApJS*, 173, 185
- Gil de Paz, A., Madore, B. F., Boissier, S., et al. 2005, *ApJ*, 627, L29
- Giovannelli, R., Haynes, M. P., Kent, B. R., et al. 2005, *AJ*, 130, 2598
- Glover, S. C. O., Federrath, C., Mac Low, M.-M., & Klessen, R. S. 2010, *MNRAS*, 404, 2
- Goddard, Q. E., Kennicutt, R. C., & Ryan-Weber, E. V. 2010, *MNRAS*, 405, 2791
- Goldreich, P. & Kwan, J. 1974, *ApJ*, 189, 441
- Goldsmith, P. F., Heyer, M., Narayanan, G., et al. 2008, *ApJ*, 680, 428
- Gordon, K. D., Clayton, G. C., Witt, A. N., & Misselt, K. A. 2000, *ApJ*, 533, 236
- Gordon, K. D., Misselt, K. A., Witt, A. N., & Clayton, G. C. 2001, *ApJ*, 551, 269
- Goto, T., Arnouts, S., Inami, H., et al. 2011, *MNRAS*, 410, 573
- Graciá-Carpio, J., García-Burillo, S., Planesas, P., Fuente, A., & Usero, A. 2008, *A&A*, 479, 703
- Gratier, P., Braine, J., Rodríguez-Fernández, N. J., et al. 2010, *A&A*, 522, A3
- Green, J. A., Caswell, J. L., Fuller, G. A., et al. 2009, *MNRAS*, 392, 783
- Greene, T. P., Wilking, B. A., Andre, P., Young, E. T., & Lada, C. J. 1994, *ApJ*, 434, 614
- Griffin, M. J., Abergel, A., Abreu, A., et al. 2010, *A&A*, 518, L3
- Guesten, R. & Mezger, P. G. 1982, *Vistas in Astronomy*, 26, 159
- Gutermuth, R. A., Megeath, S. T., Myers, P. C., et al. 2009, *ApJS*, 184, 18
- Gutermuth, R. A., Megeath, S. T., Pipher, J. L., et al. 2005, *ApJ*, 632, 397
- Gutermuth, R. A., Pipher, J. L., Megeath, S. T., et al. 2011, *ApJ*, 739, 84
- Hameed, S. & Devereux, N. 2005, *AJ*, 129, 2597
- Hao, C.-N., Kennicutt, R. C., Johnson, B. D., et al. 2011, *ApJ*, 741, 124
- Hatchell, J. & Fuller, G. A. 2008, *A&A*, 482, 855
- Hayes, M., Schaerer, D., Östlin, G., et al. 2011, *ApJ*, 730, 8
- Heiderman, A., Evans, II, N. J., Allen, L. E., Huard, T., & Heyer, M. 2010, *ApJ*, 723, 1019
- Heiles, C. & Troland, T. H. 2003, *ApJ*, 586, 1067
- Helfer, T. T., Thornley, M. D., Regan, M. W., et al. 2003, *ApJS*, 145, 259
- Helou, G., Roussel, H., Appleton, P., et al. 2004, *ApJS*, 154, 253
- Helou, G., Soifer, B. T., & Rowan-Robinson, M. 1985, *ApJ*, 298, L7
- Hennebelle, P. & Chabrier, G. 2011, *ApJ*, 743, L29
- Heyer, M., Krawczyk, C., Duval, J., & Jackson, J. M. 2009, *ApJ*, 699, 1092
- Heyer, M. H., Brunt, C., Snell, R. L., et al. 1998, *ApJS*, 115, 241
- Heyer, M. H., Carpenter, J. M., & Snell, R. L. 2001, *ApJ*, 551, 852
- Heyer, M. H., Corbelli, E., Schneider, S. E., & Young, J. S. 2004, *ApJ*, 602, 723
- Higuchi, A. E., Kurono, Y., Saito, M., & Kawabe, R. 2009, *ApJ*, 705, 468

- Hill, G. J., Gebhardt, K., Komatsu, E., et al. 2008, in *Astronomical Society of the Pacific Conference Series*, Vol. 399, *Panoramic Views of Galaxy Formation and Evolution*, ed. T. Kodama, T. Yamada, & K. Aoki, 115
- Hillenbrand, L. A. 1997, *AJ*, 113, 1733
- Hirashita, H., Buat, V., & Inoue, A. K. 2003, *A&A*, 410, 83
- Hirashita, H., Inoue, A. K., Kamaya, H., & Shibai, H. 2001, *A&A*, 366, 83
- Hirota, T., Bushimata, T., Choi, Y. K., et al. 2007, *PASJ*, 59, 897
- Ho, L. C. & Keto, E. 2007, *ApJ*, 658, 314
- Hollenbach, D. J. & Tielens, A. G. G. M. 1997, *ARA&A*, 35, 179
- Homeier, N. L. & Alves, J. 2005, *A&A*, 430, 481
- Hopkins, P. F., Quataert, E., & Murray, N. 2011, *MNRAS*, 417, 950
- Hosokawa, T., Offner, S. S. R., & Krumholz, M. R. 2011, *ApJ*, 738, 140
- Hosokawa, T. & Omukai, K. 2009, *ApJ*, 691, 823
- Hunter, D. A., Brinks, E., Elmegreen, B., et al. 2007, in *Bulletin of the American Astronomical Society*, Vol. 38, *American Astronomical Society Meeting Abstracts*, 895
- Hunter, D. A., Elmegreen, B. G., & Ludka, B. C. 2010, *AJ*, 139, 447
- Immer, K., Schuller, F., Omont, A., & Menten, K. M. 2012, *A&A*, 537, A121
- Israel, F. P. & van der Hulst, J. M. 1983, *AJ*, 88, 1736
- Jackson, J. M., Rathborne, J. M., Shah, R. Y., et al. 2006, *ApJS*, 163, 145
- James, P. A., Shane, N. S., Beckman, J. E., et al. 2004, *A&A*, 414, 23
- Jansen, R. A., Franx, M., & Fabricant, D. 2001, *ApJ*, 551, 825
- Jogee, S., Miller, S. H., Penner, K., et al. 2009, *ApJ*, 697, 1971
- Johnson, B. D., Schiminovich, D., Seibert, M., et al. 2007, *ApJS*, 173, 392
- Johnstone, D., Di Francesco, J., & Kirk, H. 2004, *ApJ*, 611, L45
- Juneau, S., Narayanan, D. T., Moustakas, J., et al. 2009, *ApJ*, 707, 1217
- Kainulainen, J., Beuther, H., Banerjee, R., Federrath, C., & Henning, T. 2011, *A&A*, 530, A64
- Kainulainen, J., Beuther, H., Henning, T., & Plume, R. 2009, *A&A*, 508, L35
- Kalberla, P. M. W. & Dedes, L. 2008, *A&A*, 487, 951
- Kalberla, P. M. W., Dedes, L., Kerp, J., & Haud, U. 2007, *A&A*, 469, 511
- Kalberla, P. M. W. & Kerp, J. 2009, *ARA&A*, 47, 27
- Karachentsev, I. D., Karachentseva, V. E., Huchtmeier, W. K., & Makarov, D. I. 2004, *AJ*, 127, 2031
- Kauffmann, G., Heckman, T. M., White, S. D. M., et al. 2003, *MNRAS*, 341, 54
- Kauffmann, J., Bertoldi, F., Bourke, T. L., Evans, II, N. J., & Lee, C. W. 2008, *A&A*, 487, 993
- Kauffmann, J. & Pillai, T. 2010, *ApJ*, 723, L7
- Kauffmann, J., Pillai, T., Shetty, R., Myers, P. C., & Goodman, A. A. 2010, *ApJ*, 716, 433
- Kaviraj, S., Schawinski, K., Devriendt, J. E. G., et al. 2007, *ApJS*, 173, 619
- Kennicutt, R. C., Calzetti, D., Aniano, G., et al. 2011, *PASP*, 123, 1347
- Kennicutt, Jr., R. C. 1989, *ApJ*, 344, 685
- Kennicutt, Jr., R. C. 1998a, *ARA&A*, 36, 189
- Kennicutt, Jr., R. C. 1998b, *ApJ*, 498, 541
- Kennicutt, Jr., R. C., Armus, L., Bendo, G., et al. 2003, *PASP*, 115, 928
- Kennicutt, Jr., R. C., Calzetti, D., Walter, F., et al. 2007, *ApJ*, 671, 333
- Kennicutt, Jr., R. C., Hao, C.-N., Calzetti, D., et al. 2009, *ApJ*, 703, 1672
- Kennicutt, Jr., R. C., Lee, J. C., Funes, José G., S. J., Sakai, S., & Akiyama, S. 2008, *ApJS*, 178, 247
- Kewley, L. J., Geller, M. J., & Jansen, R. A. 2004, *AJ*, 127, 2002
- Kewley, L. J., Geller, M. J., Jansen, R. A., & Dopita, M. A. 2002, *AJ*, 124, 3135
- Kim, C.-G., Kim, W.-T., & Ostriker, E. C. 2011, *ApJ*, 743, 25
- Kirk, J. M., Ward-Thompson, D., & André, P. 2005, *MNRAS*, 360, 1506
- Klessen, R. S., Burkert, A., & Bate, M. R. 1998, *ApJ*, 501, L205
- Knapen, J. H., Stedman, S., Bramich, D. M., Folkes, S. L., & Bradley, T. R. 2004, *A&A*, 426, 1135
- Koda, J. & Nearby Galaxies CO Survey Group. 2009, in *Bulletin of the American Astronomical Society*, Vol. 41, *American Astronomical Society Meeting Abstracts* #213, #485.04
- Koda, J., Scoville, N., Sawada, T., et al. 2009, *ApJ*, 700, L132
- Komugi, S., Sofue, Y., Nakanishi, H., Onodera, S., & Egusa, F. 2005, *PASJ*, 57, 733
- Kong, X., Charlot, S., Brinchmann, J., & Fall, S. M. 2004, *MNRAS*, 349, 769
- Koribalski, B. S. 2010, in *Astronomical Society of the Pacific Conference Series*, Vol. 421, *Galaxies in Isolation: Exploring Nature Versus Nurture*, ed. L. Verdes-Montenegro, A. Del Olmo, & J. Sulentic, 137
- Kormendy, J. & Kennicutt, Jr., R. C. 2004, *ARA&A*, 42, 603
- Kramer, C., Stutzki, J., Rohrig, R., & Corneliusen, U. 1998, *A&A*, 329, 249
- Kroupa, P., Tout, C. A., & Gilmore, G. 1993, *MNRAS*, 262, 545
- Kroupa, P. & Weidner, C. 2003, *ApJ*, 598, 1076
- Krumholz, M. R. 2011, *ApJ*, 743, 110
- Krumholz, M. R. & Bonnell, I. A. 2009, *Models for the formation of massive stars*, ed. G. Chabrier (Cambridge University Press), 288
- Krumholz, M. R., Cunningham, A. J., Klein, R. I., & McKee, C. F. 2010, *ApJ*, 713, 1120
- Krumholz, M. R., Dekel, A., & McKee, C. F. 2012, *ApJ*, 745, 69
- Krumholz, M. R., Klein, R. I., McKee, C. F., Offner, S. S. R., & Cunningham, A. J. 2009a, *Science*, 323, 754
- Krumholz, M. R. & McKee, C. F. 2005, *ApJ*, 630, 250
- Krumholz, M. R. & McKee, C. F. 2008, *Nature*, 451, 1082
- Krumholz, M. R., McKee, C. F., & Tumlinson, J. 2009b, *ApJ*, 699, 850
- Krumholz, M. R. & Thompson, T. A. 2007, *ApJ*, 669, 289
- Kuiper, R., Klahr, H., Beuther, H., & Henning, T. 2011, *ApJ*, 732, 20
- Kulkarni, S. R. & Heiles, C. 1988, *Neutral hydrogen and the diffuse interstellar medium*, ed. K. I. Kellermann & G. L. Verschuur, 95–153
- Lada, C. J., Forbrich, J., Lombardi, M., & Alves, J. F. 2012, *ApJ*, 745, 190
- Lada, C. J. & Lada, E. A. 2003, *ARA&A*, 41, 57
- Lada, C. J., Lombardi, M., & Alves, J. F. 2010, *ApJ*, 724, 687
- Lada, C. J., Muench, A. A., Rathborne, J., Alves, J. F., & Lombardi, M. 2008, *ApJ*, 672, 410
- Lada, C. J. & Wilking, B. A. 1984, *ApJ*, 287, 610
- Lada, E. A. 1992, *ApJ*, 393, L25
- Larson, R. B. 1969, *MNRAS*, 145, 271
- Larson, R. B. 1982, *MNRAS*, 200, 159
- Larson, R. B. 1987, in *Starbursts and Galaxy Evolution*, ed. T. X. Thuan, T. Montmerle, & J. Tran Thanh van, 467–482
- Laurent, O., Mirabel, I. F., Charmandaris, V., et al. 2000, *A&A*, 359, 887
- Le Floch, E., Papovich, C., Dole, H., et al. 2005, *ApJ*, 632, 169
- Lee, J. C., Gil de Paz, A., Kennicutt, Jr., R. C., et al. 2011, *ApJS*, 192, 6
- Lee, J. C., Gil de Paz, A., Tremonti, C., et al. 2009a, *ApJ*, 706, 599
- Lee, J. C., Kennicutt, R. C., Funes, José G., S. J., Sakai, S., & Akiyama, S. 2007, *ApJ*, 671, L113
- Lee, J. C., Kennicutt, Jr., R. C., Funes, S. J. J. G., Sakai, S., & Akiyama, S. 2009b, *ApJ*, 692, 1305
- Lee, J.-E., Evans, II, N. J., Shirley, Y. L., & Tatematsu, K. 2003, *ApJ*, 583, 789
- Lehmer, B. D., Alexander, D. M., Bauer, F. E., et al. 2010, *ApJ*, 724, 559
- Leitherer, C., Schaerer, D., Goldader, J. D., et al. 1999, *ApJS*, 123, 3
- Leroy, A. K., Bolatto, A., Gordon, K., et al. 2011, *ApJ*, 737, 12
- Leroy, A. K., Walter, F., Bigiel, F., et al. 2009, *AJ*, 137, 4670
- Leroy, A. K., Walter, F., Brinks, E., et al. 2008, *AJ*, 136, 2782
- Li, W., Evans, II, N. J., & Lada, E. A. 1997, *ApJ*, 488, 277
- Li, Z.-Y. & Nakamura, F. 2006, *ApJ*, 640, L187
- Liszt, H. S., Pety, J., & Lucas, R. 2010, *A&A*, 518, A45
- Liu, G., Koda, J., Calzetti, D., Fukuhara, M., & Momose, R. 2011, *ApJ*, 735, 63
- Lockman, F. J. 1989, *ApJS*, 71, 469
- Lombardi, M., Lada, C. J., & Alves, J. 2010, *A&A*, 512, A67
- Longmore, S. N., Pillai, T., Keto, E., Zhang, Q., & Qiu, K. 2011, *ApJ*, 726, 97
- Longmore, S. N., Rathborne, J., Bastian, N., et al. 2012, *ApJ*, 746, 117
- Luna, A., Bronfman, L., Carrasco, L., & May, J. 2006, *ApJ*, 641, 938
- Lynds, B. T. 1962, *ApJS*, 7, 1
- Madden, S. C. 2000, *New Astronomy Reviews*, 44, 249
- Malhotra, S., Helou, G., Stacey, G., et al. 1997, *ApJ*, 491, L27
- Maloney, P. & Black, J. H. 1988, *ApJ*, 325, 389
- Mamajek, E. E. 2009, in *American Institute of Physics Conference Series*, Vol. 1158, *American Institute of Physics Conference Series*, ed. T. Usuda, M. Tamura, & M. Ishii, 3–10
- Marcum, P. M., O’Connell, R. W., Fanelli, M. N., et al. 2001, *ApJS*, 132, 129
- Martel, H., Evans, II, N. J., & Shapiro, P. R. 2006, *ApJS*, 163, 122
- Martin, C. L. & Kennicutt, Jr., R. C. 2001, *ApJ*, 555, 301
- Martin, D. C., Fanson, J., Schiminovich, D., et al. 2005a, *ApJ*, 619, L1
- Martin, D. C., Seibert, M., Buat, V., et al. 2005b, *ApJ*, 619, L59

- Mason, K. O., Breeveld, A., Much, R., et al. 2001, *A&A*, 365, L36
- McClure-Griffiths, N. M., Dickey, J. M., Gaensler, B. M., et al. 2005, *ApJS*, 158, 178
- McKee, C. F. 1989, *ApJ*, 345, 782
- McKee, C. F. & Ostriker, E. C. 2007, *ARA&A*, 45, 565
- McKee, C. F. & Ostriker, J. P. 1977, *ApJ*, 218, 148
- McKee, C. F. & Williams, J. P. 1997, *ApJ*, 476, 144
- Meier, D. S. & Turner, J. L. 2004, *AJ*, 127, 2069
- Meier, D. S., Turner, J. L., & Hurt, R. L. 2008, *ApJ*, 675, 281
- Men'shchikov, A., André, P., Didelon, P., et al. 2010, *A&A*, 518, L103
- Menten, K. M., Reid, M. J., Forbrich, J., & Brunthaler, A. 2007, *A&A*, 474, 515
- Meurer, G. R., Hanish, D. J., Ferguson, H. C., et al. 2006, *ApJS*, 165, 307
- Meurer, G. R., Heckman, T. M., & Calzetti, D. 1999, *ApJ*, 521, 64
- Meurer, G. R., Wong, O. I., Kim, J. H., et al. 2009, *ApJ*, 695, 765
- Meyer, M. J., Zwaan, M. A., Webster, R. L., et al. 2004, *MNRAS*, 350, 1195
- Mezger, P. G. 1987, in *Starbursts and Galaxy Evolution*, ed. T. X. Thuan, T. Montmerle, & J. Tran Thanh van, 3–18
- Miller, G. E. & Scalo, J. M. 1979, *ApJS*, 41, 513
- Misiriotis, A., Xilouris, E. M., Papamastorakis, J., Boumis, P., & Goudis, C. D. 2006, *A&A*, 459, 113
- Molinari, S., Swinyard, B., Bally, J., et al. 2010, *A&A*, 518, L100
- Momose, R. 2012, Ph.D. Dissertation, University of Tokyo
- Motte, F., André, P., & Neri, R. 1998, *A&A*, 336, 150
- Mouschovias, T. C. 1991, in *NATO ASIC Proc. 342: The Physics of Star Formation and Early Stellar Evolution*, ed. C. J. Lada & N. D. Kylafis, 449
- Mouschovias, T. C. & Spitzer, Jr., L. 1976, *ApJ*, 210, 326
- Moustakas, J., Kennicutt, Jr., R. C., & Tremonti, C. A. 2006, *ApJ*, 642, 775
- Mueller, K. E., Shirley, Y. L., Evans, II, N. J., & Jacobson, H. R. 2002, *ApJS*, 143, 469
- Murakami, H., Baba, H., Barthel, P., et al. 2007, *PASJ*, 59, 369
- Murphy, E. J., Condon, J. J., Schinnerer, E., et al. 2011, *ApJ*, 737, 67
- Murray, N. 2011, *ApJ*, 729, 133
- Murray, N. & Rahman, M. 2010, *ApJ*, 709, 424
- Myers, P. C. 2009, *ApJ*, 706, 1341
- Myers, P. C. 2011, *ApJ*, 743, 98
- Nakanishi, H. & Sofue, Y. 2006, *PASJ*, 58, 847
- Narayanan, D., Cox, T. J., Shirley, Y., et al. 2008, *ApJ*, 684, 996
- Narayanan, D., Krumholz, M. R., Ostriker, E. C., & Hernquist, L. 2012, *MNRAS*, 421, 3127
- Nguyen Luong, Q., Motte, F., Schuller, F., et al. 2011, *A&A*, 529, A41
- Niklas, S., Klein, U., & Wielebinski, R. 1997, *A&A*, 322, 19
- Noeske, K. G., Faber, S. M., Weiner, B. J., et al. 2007, *ApJ*, 660, L47
- Oey, M. S., Meurer, G. R., Yelda, S., et al. 2007, *ApJ*, 661, 801
- Oka, T., Hasegawa, T., Hayashi, M., Handa, T., & Sakamoto, S. 1998, *ApJ*, 493, 730
- Omukai, K. 2007, *PASJ*, 59, 589
- Onishi, T., Mizuno, A., Kawamura, A., Ogawa, H., & Fukui, Y. 1998, *ApJ*, 502, 296
- Onodera, S., Kuno, N., Tosaki, T., et al. 2010, *ApJ*, 722, L127
- Ostriker, E. C., McKee, C. F., & Leroy, A. K. 2010, *ApJ*, 721, 975
- Ostriker, E. C. & Shetty, R. 2011, *ApJ*, 731, 41
- Ouchi, M., Ono, Y., Egami, E., et al. 2009, *ApJ*, 696, 1164
- Ouchi, M., Shimasaku, K., Furusawa, H., et al. 2010, *ApJ*, 723, 869
- Overzier, R. A., Heckman, T. M., Wang, J., et al. 2011, *ApJ*, 726, L7
- Pak, S., Jaffe, D. T., van Dishoeck, E. F., Johansson, L. E. B., & Booth, R. S. 1998, *ApJ*, 498, 735
- Palla, F. & Stahler, S. W. 1992, *ApJ*, 392, 667
- Peeters, E., Spoon, H. W. W., & Tielens, A. G. G. M. 2004, *ApJ*, 613, 986
- Perauld, M., Omont, A., Simon, G., et al. 1996, *A&A*, 315, L165
- Peretto, N. & Fuller, G. A. 2009, *A&A*, 505, 405
- Pérez-González, P. G., Zamorano, J., Gallego, J., Aragón-Salamanca, A., & Gil de Paz, A. 2003, *ApJ*, 591, 827
- Persic, M., Rephaeli, Y., Braito, V., et al. 2004, *A&A*, 419, 849
- Pestalozzi, M. R., Minier, V., & Booth, R. S. 2005, *A&A*, 432, 737
- Peterson, D. E., Caratti o Garatti, A., Bourke, T. L., et al. 2011, *ApJS*, 194, 43
- Pflamm-Altenburg, J., Weidner, C., & Kroupa, P. 2007, *ApJ*, 671, 1550
- Pflamm-Altenburg, J., Weidner, C., & Kroupa, P. 2009, *MNRAS*, 395, 394
- Pierce-Price, D., Richer, J. S., Greaves, J. S., et al. 2000, *ApJ*, 545, L121
- Pilbratt, G. L., Riedinger, J. R., Passvogel, T., et al. 2010, *A&A*, 518, L1
- Pineda, J. E., Goodman, A. A., Arce, H. G., et al. 2010a, *ApJ*, 712, L116
- Pineda, J. L., Goldsmith, P. F., Chapman, N., et al. 2010b, *ApJ*, 721, 686
- Planck Collaboration, Ade, P. A. R., Aghanim, N., et al. 2011a, *A&A*, 536, A1
- Planck Collaboration, Ade, P. A. R., Aghanim, N., et al. 2011b, *A&A*, 536, A19
- Planck Collaboration, Ade, P. A. R., Aghanim, N., et al. 2011c, *A&A*, 536, A23
- Plume, R., Jaffe, D. T., & Evans, II, N. J. 1992, *ApJS*, 78, 505
- Plume, R., Jaffe, D. T., Evans, II, N. J., Martin-Pintado, J., & Gomez-Gonzalez, J. 1997, *ApJ*, 476, 730
- Pogge, R. W. & Eskridge, P. B. 1993, *AJ*, 106, 1405
- Poglitsch, A., Waelkens, C., Geis, N., et al. 2010, *A&A*, 518, L2
- Pontoppidan, K. M., Boogert, A. C. A., Fraser, H. J., et al. 2008, *ApJ*, 678, 1005
- Porrás, A., Christopher, M., Allen, L., et al. 2003, *AJ*, 126, 1916
- Portegies Zwart, S. F., McMillan, S. L. W., & Gieles, M. 2010, *ARA&A*, 48, 431
- Prescott, M. K. M., Kennicutt, Jr., R. C., Bendo, G. J., et al. 2007, *ApJ*, 668, 182
- Pudritz, R. E., Ouyed, R., Fendt, C., & Brandenburg, A. 2007, *Protostars and Planets V*, 277
- Purcell, C. R., Balasubramanyam, R., Burton, M. G., et al. 2006, *MNRAS*, 367, 553
- Quirk, W. J. & Tinsley, B. M. 1973, *ApJ*, 179, 69
- Rahman, N., Bolatto, A. D., Wong, T., et al. 2011, *ApJ*, 730, 72
- Rahman, N., Bolatto, A. D., Xue, R., et al. 2012, *ApJ*, 745, 183
- Raiter, A., Schaerer, D., & Fosbury, R. A. E. 2010, *A&A*, 523, A64
- Ranalli, P., Comastri, A., & Setti, G. 2003, *A&A*, 399, 39
- Rathborne, J. M., Johnson, A. M., Jackson, J. M., Shah, R. Y., & Simon, R. 2009, *ApJS*, 182, 131
- Rebull, L. M., Stapelfeldt, K. R., Evans, II, N. J., et al. 2007, *ApJS*, 171, 447
- Reddy, N., Dickinson, M., Elbaz, D., et al. 2012, *ApJ*, 744, 154
- Reid, M. A., Wadsley, J., Petitclerc, N., & Sills, A. 2010, *ApJ*, 719, 561
- Reid, M. A. & Wilson, C. D. 2005, *ApJ*, 625, 891
- Reid, M. J., Menten, K. M., Zheng, X. W., et al. 2009, *ApJ*, 700, 137
- Reiter, M., Shirley, Y. L., Wu, J., et al. 2011a, *ApJ*, 740, 40
- Reiter, M., Shirley, Y. L., Wu, J., et al. 2011b, *ApJS*, 195, 1
- Relaño, M., Lisenfeld, U., Pérez-González, P. G., Vílchez, J. M., & Battaner, E. 2007, *ApJ*, 667, L141
- Rieke, G. H., Alonso-Herrero, A., Weiner, B. J., et al. 2009, *ApJ*, 692, 556
- Roberts, M. S. 1975, *Radio Observations of Neutral Hydrogen in Galaxies*, ed. A. Sandage, M. Sandage, & J. Kristian (the University of Chicago Press), 309
- Robertson, B. E. & Kravtsov, A. V. 2008, *ApJ*, 680, 1083
- Robitaille, T. P. & Whitney, B. A. 2010, *ApJ*, 710, L11
- Robitaille, T. P., Whitney, B. A., Indebetouw, R., Wood, K., & Denzmore, P. 2006, *ApJS*, 167, 256
- Rochau, B., Brandner, W., Stolte, A., et al. 2010, *ApJ*, 716, L90
- Rodríguez-Fernández, N. J., Braine, J., Brouillet, N., & Combes, F. 2006, *A&A*, 453, 77
- Roman-Duval, J., Jackson, J. M., Heyer, M., Rathborne, J., & Simon, R. 2010, *ApJ*, 723, 492
- Roming, P. W. A., Kennedy, T. E., Mason, K. O., et al. 2005, *Space Sci. Rev.*, 120, 95
- Rosolowsky, E. 2005, *PASP*, 117, 1403
- Rosolowsky, E., Dunham, M. K., Ginsburg, A., et al. 2010, *ApJS*, 188, 123
- Rosolowsky, E., Pineda, J. E., & Gao, Y. 2011, *MNRAS*, 415, 1977
- Roussel, H., Helou, G., Hollenbach, D. J., et al. 2007, *ApJ*, 669, 959
- Roussel, H., Sauvage, M., Vigroux, L., & Bosma, A. 2001, *A&A*, 372, 427
- Ruphy, S., Robin, A. C., Epchtein, N., et al. 1996, *A&A*, 313, L21
- Russeil, D., Pestalozzi, M., Mottram, J. C., et al. 2011, *A&A*, 526, A151
- Ryan-Weber, E. V., Meurer, G. R., Freeman, K. C., et al. 2004, *AJ*, 127, 1431
- Sadavoy, S. I., Di Francesco, J., Bontemps, S., et al. 2010, *ApJ*, 710, 1247
- Salim, S. & Rich, R. M. 2010, *ApJ*, 714, L290
- Salim, S., Rich, R. M., Charlot, S., et al. 2007, *ApJS*, 173, 267
- Salpeter, E. E. 1955, *ApJ*, 121, 161
- Sana, H. & Evans, C. J. 2011, in *IAU Symposium, Vol. 272, IAU Symposium*, ed. C. Neiner, G. Wade, G. Meynet, & G. Peters, 474–485
- Sánchez, S. F., Kennicutt, R. C., Gil de Paz, A., et al. 2012, *A&A*, 538, A8
- Sauvage, M. & Thuan, T. X. 1992, *ApJ*, 396, L69

- Scalo, J. 1990, in *Astrophysics and Space Science Library*, Vol. 162, *Physical Processes in Fragmentation and Star Formation*, ed. R. Capuzzo-Dolcetta, C. Chiosi, & A. di Fazio, 151–176
- Scarlata, C., Colbert, J., Teplitz, H. I., et al. 2009, *ApJ*, 704, L98
- Schaye, J. 2004, *ApJ*, 609, 667
- Schechter, P. 1976, *ApJ*, 203, 297
- Schiminovich, D., Wyder, T. K., Martin, D. C., et al. 2007, *ApJS*, 173, 315
- Schlingman, W. M., Shirley, Y. L., Schenk, D. E., et al. 2011, *ApJS*, 195, 14
- Schmidt, M. 1959, *ApJ*, 129, 243
- Schmidt, M. 1963, *ApJ*, 137, 758
- Schnurr, O., Casoli, J., Chené, A.-N., Moffat, A. F. J., & St-Louis, N. 2008, *MNRAS*, 389, L38
- Schruba, A., Leroy, A. K., Walter, F., et al. 2011, *AJ*, 142, 37
- Schuller, F., Menten, K. M., Contreras, Y., et al. 2009, *A&A*, 504, 415
- Schuster, K. F., Kramer, C., Hitschfeld, M., Garcia-Burillo, S., & Mookerjee, B. 2007, *A&A*, 461, 143
- Scoville, N. Z., Evans, A. S., Thompson, R., et al. 2000, *AJ*, 119, 991
- Seibert, M., Martin, D. C., Heckman, T. M., et al. 2005, *ApJ*, 619, L55
- Shang, H., Li, Z.-Y., & Hirano, N. 2007, *Protostars and Planets V*, 261
- Shapiro, K. L., Falcón-Barroso, J., van de Ven, G., et al. 2010, *MNRAS*, 402, 2140
- Sheth, K., Vogel, S. N., Wilson, C. D., & Dame, T. M. 2008, *ApJ*, 675, 330
- Shetty, R., Glover, S. C., Dullemond, C. P., & Klessen, R. S. 2011a, *MNRAS*, 412, 1686
- Shetty, R., Glover, S. C., Dullemond, C. P., et al. 2011b, *MNRAS*, 415, 3253
- Shi, Y., Helou, G., Yan, L., et al. 2011, *ApJ*, 733, 87
- Shirley, Y. L., Evans, II, N. J., Young, K. E., Knez, C., & Jaffe, D. T. 2003, *ApJS*, 149, 375
- Shirley, Y. L., Huard, T. L., Pontoppidan, K. M., et al. 2011, *ApJ*, 728, 143
- Shu, F. H., Adams, F. C., & Lizano, S. 1987, *ARA&A*, 25, 23
- Silk, J. 1997, *ApJ*, 481, 703
- Skibba, R. A., Engelbracht, C. W., Dale, D., et al. 2011, *ApJ*, 738, 89
- Smith, J. D. T., Draine, B. T., Dale, D. A., et al. 2007, *ApJ*, 656, 770
- Smith, L. J., Norris, R. P. F., & Crowther, P. A. 2002, *MNRAS*, 337, 1309
- Snell, R. L., Carpenter, J. M., & Heyer, M. H. 2002, *ApJ*, 578, 229
- Sodroski, T. J., Odegard, N., Arendt, R. G., et al. 1997, *ApJ*, 480, 173
- Soifer, B. T., Helou, G., & Werner, M. 2008, *ARA&A*, 46, 201
- Solomon, P. M., Rivolo, A. R., Barrett, J., & Yahil, A. 1987, *ApJ*, 319, 730
- Solomon, P. M. & Sage, L. J. 1988, *ApJ*, 334, 613
- Solomon, P. M. & Vanden Bout, P. A. 2005, *ARA&A*, 43, 677
- Stahler, S. W. & Palla, F. 2005, *The Formation of Stars*
- Stecher, T. P., Cornett, R. H., Greason, M. R., et al. 1997, *PASP*, 109, 584
- Stil, J. M., Taylor, A. R., Dickey, J. M., et al. 2006, *AJ*, 132, 1158
- Stone, J. M., Ostriker, E. C., & Gammie, C. F. 1998, *ApJ*, 508, L99
- Stutz, A. M., Bieging, J. H., Rieke, G. H., et al. 2007, *ApJ*, 665, 466
- Stutzki, J., Bensch, F., Heithausen, A., Ossenkopf, V., & Zielinsky, M. 1998, *A&A*, 336, 697
- Sullivan, M., Treyer, M. A., Ellis, R. S., et al. 2000, *MNRAS*, 312, 442
- Swift, J. J. & Williams, J. P. 2008, *ApJ*, 679, 552
- Symeonidis, M., Georgakakis, A., Seymour, N., et al. 2011, *MNRAS*, 417, 2239
- Tacconi, L. J., Genzel, R., Smail, I., et al. 2008, *ApJ*, 680, 246
- Tasker, E. J. 2011, *ApJ*, 730, 11
- Tasker, E. J. & Tan, J. C. 2009, *ApJ*, 700, 358
- Taylor, A. R., Gibson, S. J., Peracaula, M., et al. 2003, *AJ*, 125, 3145
- Terebey, S., Shu, F. H., & Cassen, P. 1984, *ApJ*, 286, 529
- Thilker, D. A., Bianchi, L., Boissier, S., et al. 2005, *ApJ*, 619, L79
- Thilker, D. A., Bianchi, L., Meurer, G., et al. 2007, *ApJS*, 173, 538
- Treyer, M., Schiminovich, D., Johnson, B., et al. 2007, *ApJS*, 173, 256
- Treyer, M., Schiminovich, D., Johnson, B. D., et al. 2010, *ApJ*, 719, 1191
- Urban, A., Martel, H., & Evans, II, N. J. 2010, *ApJ*, 710, 1343
- van der Tak, F. F. S., van Dishoeck, E. F., Evans, II, N. J., & Blake, G. A. 2000, *ApJ*, 537, 283
- van Dishoeck, E. F. & Black, J. H. 1988, *ApJ*, 334, 771
- van Dokkum, P. G. & Conroy, C. 2011, *ApJ*, 735, L13
- Vázquez-Semadeni, E., Banerjee, R., Gómez, G. C., et al. 2011, *MNRAS*, 414, 2511
- Verley, S., Corbelli, E., Giovanardi, C., & Hunt, L. K. 2010, *A&A*, 510, A64
- Walsh, A. J., Breen, S. L., Britton, T., et al. 2011, *MNRAS*, 416, 1764
- Walsh, A. J., Myers, P. C., & Burton, M. G. 2004, *ApJ*, 614, 194
- Walter, F., Brinks, E., de Blok, W. J. G., et al. 2008, *AJ*, 136, 2563
- Walterbos, R. A. M. & Greenawalt, B. 1996, *ApJ*, 460, 696
- Wang, B. & Heckman, T. M. 1996, *ApJ*, 457, 645
- Ward-Thompson, D., André, P., Crutcher, R., et al. 2007a, *Protostars and Planets V*, 33
- Ward-Thompson, D., Di Francesco, J., Hatchell, J., et al. 2007b, *PASP*, 119, 855
- Ward-Thompson, D., Motte, F., & André, P. 1999, *MNRAS*, 305, 143
- Watson, C., Povich, M. S., Churchwell, E. B., et al. 2008, *ApJ*, 681, 1341
- Weedman, D. W., Feldman, F. R., Balzano, V. A., et al. 1981, *ApJ*, 248, 105
- Weidner, C. & Kroupa, P. 2006, *MNRAS*, 365, 1333
- Weingartner, J. C. & Draine, B. T. 2001, *ApJ*, 548, 296
- Weisz, D. R., Johnson, B. D., Johnson, L. C., et al. 2012, *ApJ*, 744, 44
- Weisz, D. R., Skillman, E. D., Cannon, J. M., et al. 2008, *ApJ*, 689, 160
- Werner, M. W., Roellig, T. L., Low, F. J., et al. 2004, *ApJS*, 154, 1
- Whittet, D. C. B., Shenoy, S. S., Bergin, E. A., et al. 2007, *ApJ*, 655, 332
- Williams, B. F., Dalcanton, J. J., Johnson, L. C., et al. 2011, *ApJ*, 734, L22
- Williams, J. P., Blitz, L., & McKee, C. F. 2000, *Protostars and Planets IV*, 97
- Williams, J. P. & McKee, C. F. 1997, *ApJ*, 476, 166
- Wilson, C. D., Warren, B. E., Israel, F. P., et al. 2009, *ApJ*, 693, 1736
- Wilson, T. L. & Rood, R. 1994, *ARA&A*, 32, 191
- Wolfire, M. G., Hollenbach, D., & McKee, C. F. 2010, *ApJ*, 716, 1191
- Wong, T. & Blitz, L. 2002, *ApJ*, 569, 157
- Wong, T., Hughes, A., Ott, J., et al. 2011, *ApJS*, 197, 16
- Wouterloot, J. G. A. & Brand, J. 1989, *A&AS*, 80, 149
- Wright, E. L., Eisenhardt, P. R. M., Mainzer, A. K., et al. 2010, *AJ*, 140, 1868
- Wu, H., Cao, C., Hao, C.-N., et al. 2005a, *ApJ*, 632, L79
- Wu, J. & Evans, II, N. J. 2003, *ApJ*, 592, L79
- Wu, J., Evans, II, N. J., Gao, Y., et al. 2005b, *ApJ*, 635, L173
- Wu, J., Evans, II, N. J., Shirley, Y. L., & Knez, C. 2010a, *ApJS*, 188, 313
- Wu, J., Vanden Bout, P. A., Evans, II, N. J., & Dunham, M. M. 2009, *ApJ*, 707, 988
- Wu, Y., Helou, G., Armus, L., et al. 2010b, *ApJ*, 723, 895
- Wu, Y., Shi, Y., Helou, G., et al. 2011, *ApJ*, 734, 40
- Wu, Y., Wei, Y., Zhao, M., et al. 2004, *A&A*, 426, 503
- Wuyts, S., Förster Schreiber, N. M., Lutz, D., et al. 2011, *ApJ*, 738, 106
- Wyder, T. K., Martin, D. C., Barlow, T. A., et al. 2009, *ApJ*, 696, 1834
- Yan, L., Sajina, A., Fadda, D., et al. 2007, *ApJ*, 658, 778
- Yorke, H. W. & Sonnhalter, C. 2002, *ApJ*, 569, 846
- Yun, M. S., Reddy, N. A., & Condon, J. J. 2001, *ApJ*, 554, 803
- Yusef-Zadeh, F., Hewitt, J. W., Arendt, R. G., et al. 2009, *ApJ*, 702, 178
- Zaritsky, D. & Christlein, D. 2007, *AJ*, 134, 135
- Zasov, A. V. & Stmakov, S. G. 1988, *Astrofizika*, 29, 190
- Zhang, Q. & Fall, S. M. 1999, *ApJ*, 527, L81
- Zhu, Y.-N., Wu, H., Cao, C., & Li, H.-N. 2008, *ApJ*, 686, 155
- Zinnecker, H. & Yorke, H. W. 2007, *ARA&A*, 45, 481
- Zuckerman, B. & Evans, II, N. J. 1974, *ApJ*, 192, L149
- Zuckerman, B. & Palmer, P. 1974, *ARA&A*, 12, 279

TABLE 1  
STAR FORMATION RATE CALIBRATIONS

Band	Age Range (Myr) <sup>a</sup>	$L_x$ Units	$\log C_x$	$\dot{M}_*/\dot{M}_*(\text{K98})$	References
FUV	0 – 10 – 100	$\text{ergs s}^{-1} (\nu L_\nu)$	43.35	0.63	1, 2
NUV	0 – 10 – 200	$\text{ergs s}^{-1} (\nu L_\nu)$	43.17	0.64	1, 2
H $\alpha$	0 – 3 – 10	$\text{ergs s}^{-1}$	41.27	0.68	1, 2
TIR	0 – 5 – 100 <sup>b</sup>	$\text{ergs s}^{-1} (3\text{--}1100 \mu\text{m})$	43.41	0.86	1, 2
24 $\mu\text{m}$	0 – 5 – 100 <sup>b</sup>	$\text{ergs s}^{-1} (\nu L_\nu)$	42.69		3
70 $\mu\text{m}$	0 – 5 – 100 <sup>b</sup>	$\text{ergs s}^{-1} (\nu L_\nu)$	43.23		4
1.4 GHz	0 – 100 :	$\text{ergs s}^{-1} \text{Hz}^{-1}$	28.20		1
2–10 keV	0 – 100 :	$\text{ergs s}^{-1}$	39.77	0.86	5

NOTE. — References: (1) Murphy et al. (2011); (2) Hao et al. (2011); (3) Rieke et al. (2009); (4) Calzetti et al. (2010a); (5) Ranalli et al. (2003)

<sup>a</sup>Second number gives mean age of stellar population contributing to emission, third number gives age below which 90% of emission is contributed.

<sup>b</sup>Numbers are sensitive to star formation history, those given are for continuous star formation over 0–100 Myr. For more quiescent regions (e.g., disks of normal galaxies) the maximum age will be considerably longer.

TABLE 2  
MULTI-WAVELENGTH DUST-CORRECTIONS

Composite Tracer	Reference
$L(FUV)_{corr} = L(FUV)_{obs} + 0.46L(TIR)$	1
$L(FUV)_{corr} = L(FUV)_{obs} + 3.89L(25\mu\text{m})$	1
$L(FUV)_{corr} = L(FUV)_{obs} + 7.2 \times 10^{14} L(1.4\text{GHz})^a$	1
$L(NUV)_{corr} = L(NUV)_{obs} + 0.27L(TIR)$	1
$L(NUV)_{corr} = L(NUV)_{obs} + 2.26L(25\mu\text{m})$	1
$L(NUV)_{corr} = L(NUV)_{obs} + 4.2 \times 10^{14} L(1.4\text{GHz})^a$	1
$L(H\alpha)_{corr} = L(H\alpha)_{obs} + 0.0024L(TIR)$	2
$L(H\alpha)_{corr} = L(H\alpha)_{obs} + 0.020L(25\mu\text{m})$	2
$L(H\alpha)_{corr} = L(H\alpha)_{obs} + 0.011L(8\mu\text{m})$	2
$L(H\alpha)_{corr} = L(H\alpha)_{obs} + 0.39 \times 10^{13} L(1.4\text{GHz})^a$	2

NOTE. — References: (1) Hao et al. (2011); (2) Kennicutt et al. (2009)

<sup>a</sup>Radio luminosity in units of  $\text{ergs s}^{-1} \text{Hz}^{-1}$

TABLE 3  
STAR FORMATION REGIMES

Name	$\Sigma_{gas}$ ( $\text{M}_\odot \text{pc}^{-2}$ )	Gas Properties	Star Formation	Examples
Low Density	$< 10$	Mostly atomic	low, sparse	outer disks early type galaxies LSB galaxies dwarf galaxies solar nbd in MW
Intermediate Density	$10 - \Sigma_{dense}$	atomic $\rightarrow$ molecular	moderate	normal disks inner MW molecular clouds
High Density	$> \Sigma_{dense}$	molecular $\rightarrow$ dense	high, concentrated	some nuclear regions starbursts mergers clumps and cores

NOTE. — The dividing line between Intermediate and High-density regimes ( $\Sigma_{dense}$ ) ranges from 100 to 300  $\text{M}_\odot \text{pc}^{-2}$ .



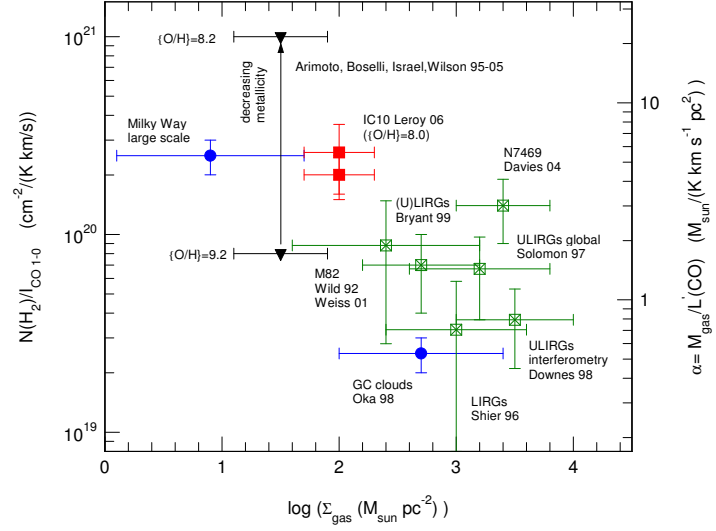


FIG. 1.— Compilation of the conversion factor ( $X(\text{CO})$ ) from the CO  $J = 1 \rightarrow 0$  integrated intensity [ $I_{\text{CO}}$  ( $\text{K km s}^{-1}$ )] or luminosity [ $L'_{\text{CO}}$  ( $\text{K km s}^{-1} \text{ pc}^2$ )] to  $\text{H}_2$  column density (left vertical scale) and total ( $\text{H}_2$  and He) gas mass (right vertical scale), derived in various Galactic and extragalactic targets. Blue circles denote measurements in the disk and center of the Milky Way, based on various virial, extinction, and isotopomeric analyses. Crossed green squares denote measurements in starbursts and (U)LIRGs, mainly based on dynamical constraints. Filled triangles denote conversion factors as a function of decreasing metallicity (vertical arrow) from (bottom) to 8.2 (top), derived mainly from global (large scale) dust mass measurements in nearby galaxies and dwarfs by several groups. In contrast, red filled squares mark X-factor measurements toward individual clouds, over the same range in metallicity. Taken from Tacconi et al. (2008); references to the original work are given there. Reproduced by permission of the AAS.

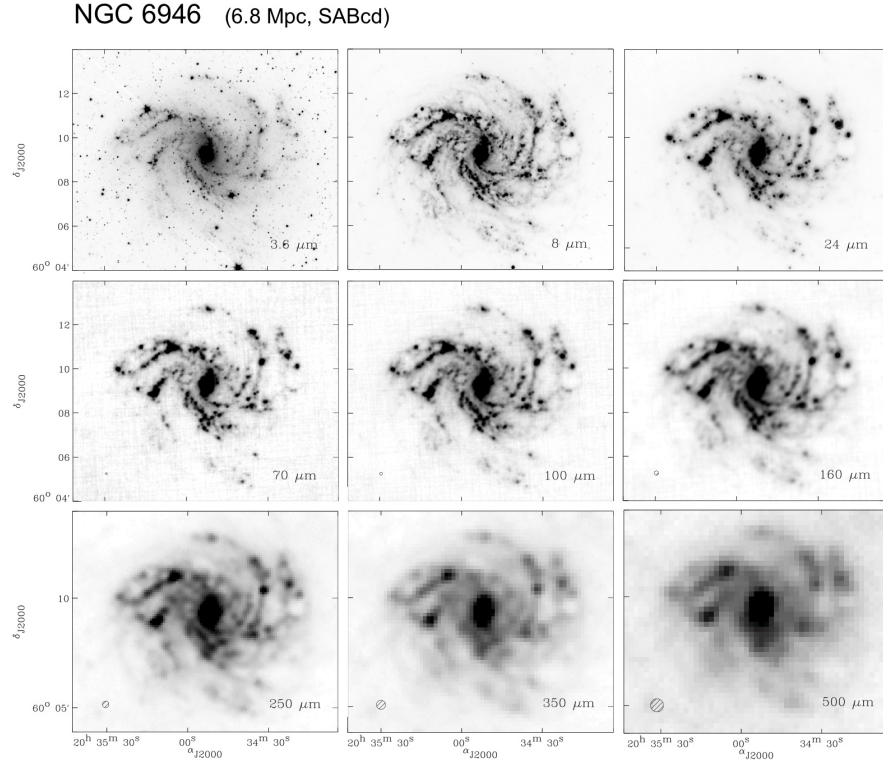


FIG. 2.— A montage of infrared images of NGC 6946 from *Spitzer* (SINGS) and *Herschel* (KINGFISH). *Top panels:* *Spitzer* IRAC images at  $3.6\ \mu\text{m}$  and  $8.0\ \mu\text{m}$ , and *MIPS* image at  $24\ \mu\text{m}$ . The emission at these wavelengths is dominated by stars, small PAH dust grains, and small dust grains heated by intense radiation fields, respectively. *Middle panels:* *Herschel* PACS images at  $70\ \mu\text{m}$ ,  $100\ \mu\text{m}$ , and  $160\ \mu\text{m}$ , processed with the Scanamorphos map making package. Note the excellent spatial resolution despite the longer wavelengths, and the progressive increase in contributions from diffuse dust emission (“cirrus”) with increasing wavelength. *Bottom panels:* *Herschel* SPIRE images at  $250\ \mu\text{m}$ ,  $350\ \mu\text{m}$ , and  $500\ \mu\text{m}$ . These bands trace increasingly cooler components of the main thermal dust emission, with possible additional contributions from “submillimeter excess” emission at the longest SPIRE wavelengths. FWHM beam sizes for the respective *Herschel* bands are shown in the lower left corner of each panel. This figure originally appeared in the Publications of the Astronomical Society of the Pacific (Kennicutt et al. 2011). Copyright 2011, Astronomical Society of the Pacific; reproduced with permission of the Editors.

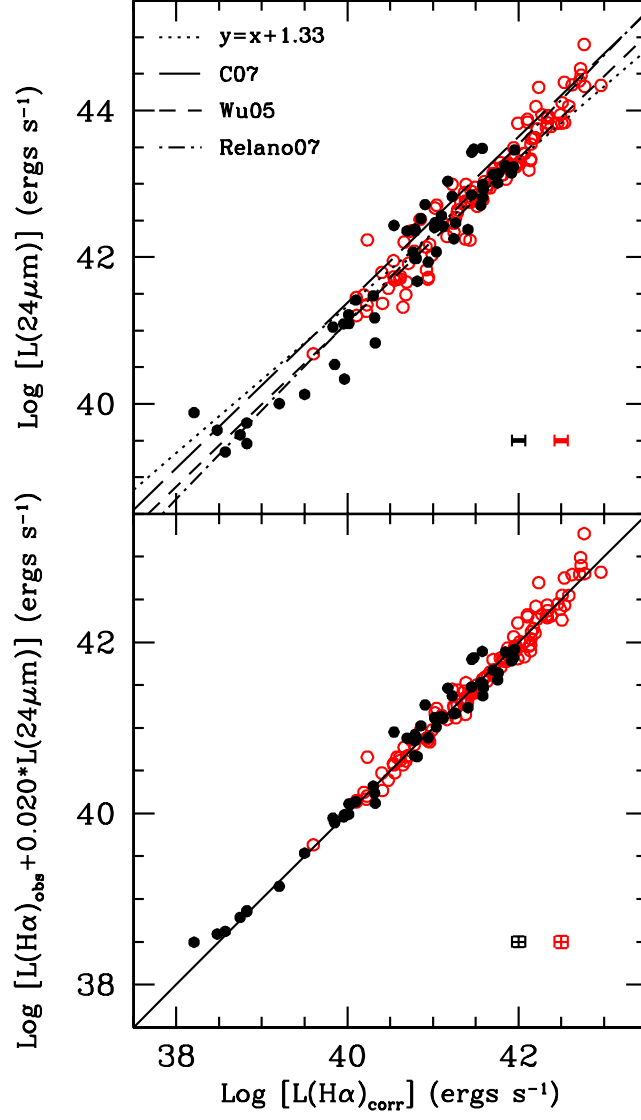


FIG. 3.— Top: relation between observed  $24\mu\text{m}$  IR luminosity and dust-corrected  $\text{H}\alpha$  luminosity for nearby galaxies. The dust corrections were derived from the absorption-corrected  $\text{H}\alpha/\text{H}\beta$  ratios in optical spectra. The dotted line shows a linear relation for comparison, while the other lines show published fits to other samples of galaxies. Bottom: linear combination of (uncorrected)  $\text{H}\alpha$  and  $24\mu\text{m}$  luminosities compared to the same Balmer-corrected  $\text{H}\alpha$  luminosities. Note the tightness and linearity of the relation over nearly the entire luminosity range. Taken from Kennicutt et al. (2009); reproduced by permission of the AAS.

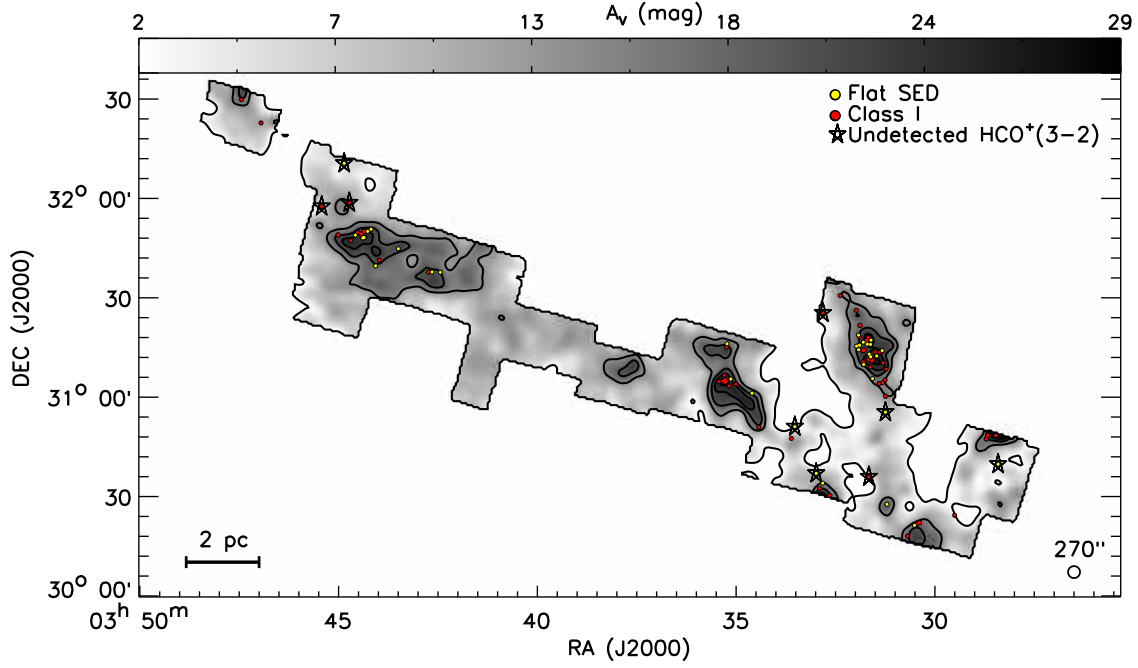


FIG. 4.— Example of the strong concentration of star formation in regions of high extinction, or mass surface density in the Perseus molecular cloud. The gray-scale with black contours is the extinction map ranging from 2 to 29 mag in intervals of 4.5 mag. The yellow filled circles are Flat SED sources and the red filled circles are Class I sources. Sources with an open star were not detected in HCO<sup>+</sup>  $J = 3 \rightarrow 2$  emission and are either older sources that may have moved from their birthplace or background galaxies. Essentially all truly young objects lie within contours of  $A_V \geq 8$  mag. Taken from Heiderman et al. (2010); reproduced by permission of the AAS.

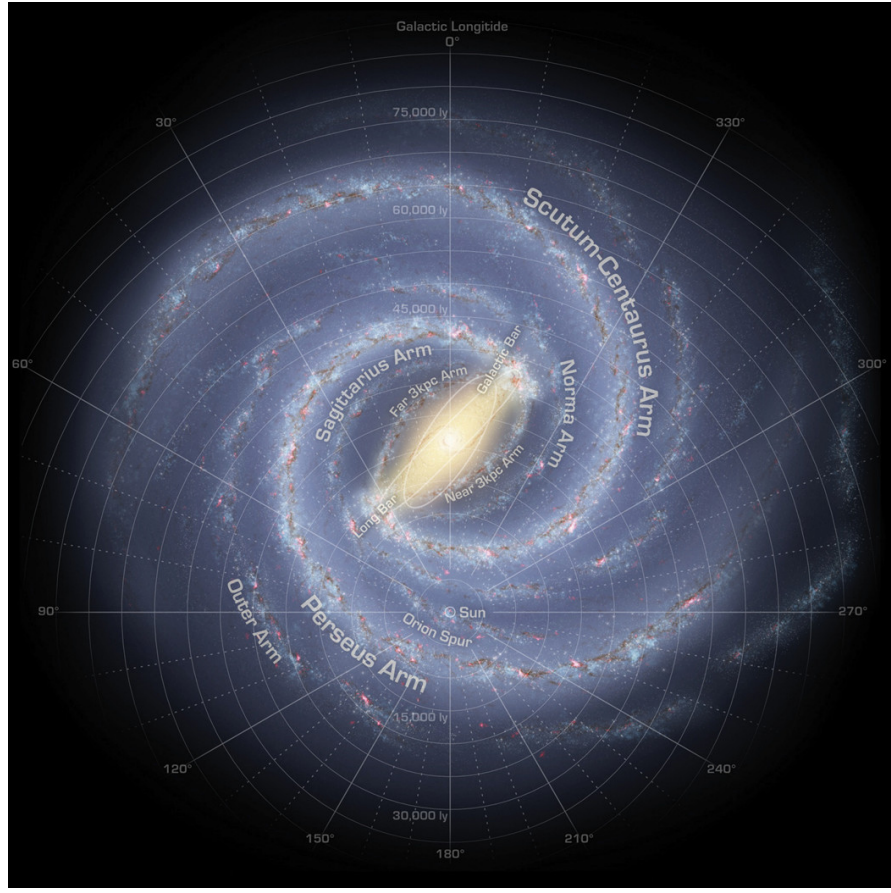


FIG. 5.— Sketch of approximately how the Galaxy is likely to appear viewed face-on, with Galactic coordinates overlaid and the locations of spiral arms and the Sun indicated. This sketch was originally made by Robert Hurt of the Spitzer Science Center in consultation with Robert Benjamin at the University of Wisconsin-Whitewater. The image is based on data obtained from the literature at radio, infrared, and visible wavelengths. As viewed from a great distance our Galaxy would appear to be a grand-design two-armed barred spiral with several secondary arms: the main arms being the Scutum-Centaurus and Perseus arms and the secondary arms being Sagittarius, the outer arm, and the 3 kpc expanding arm. Adapted from a figure in Churchwell et al. (2009) by R. Benjamin. The original figure appeared in the Publications of the Astronomical Society of the Pacific, Copyright 2009, Astronomical Society of the Pacific; reproduced with permission of the Editors.

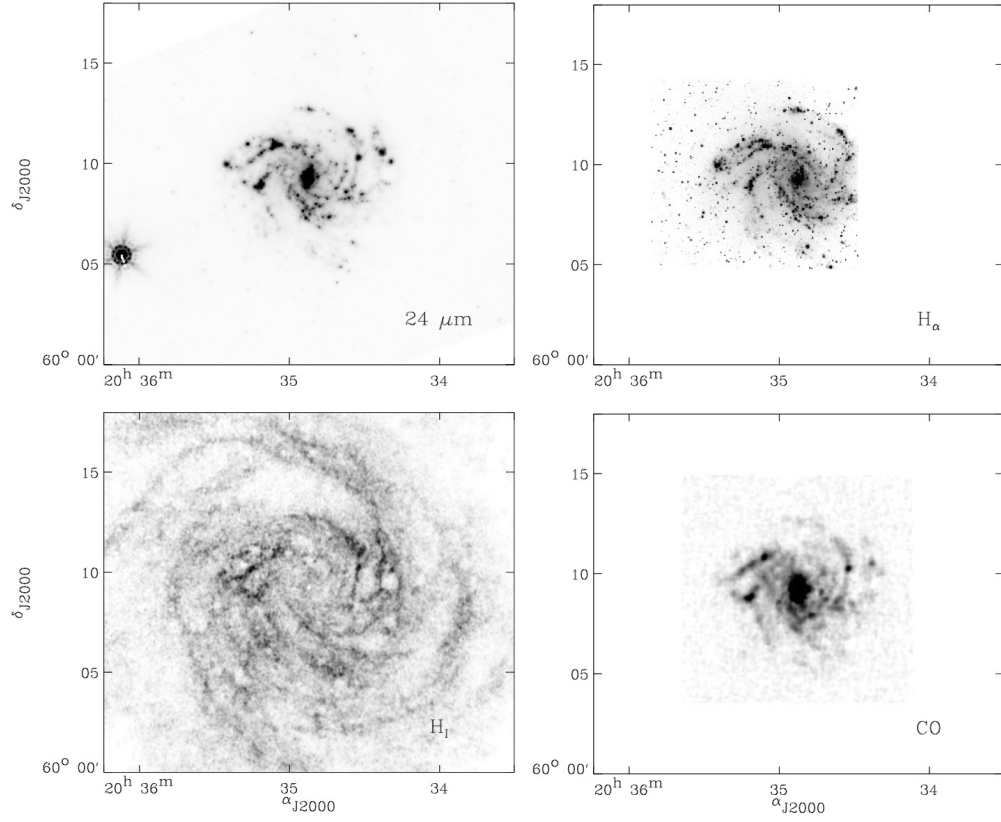


FIG. 6.— High-resolution maps of star formation tracers and cold gas components in NGC 6946. Top left: Spitzer 24  $\mu\text{m}$  dust emission from the SINGS/KINGFISH project (Kennicutt et al. 2011); Top right:  $\text{H}\alpha$  emission from Knapen et al. (2004); Bottom left:  $\text{H I}$  emission from the VLA THINGS survey (Walter et al. 2008); Bottom right:  $\text{CO } J=2 \rightarrow 1$  emission from the HERACLES survey (Leroy et al. 2009). Note that the  $\text{H I}$  map extends over a much wider area than the  $\text{CO}$ ,  $\text{H}\alpha$ , and 24  $\mu\text{m}$  observations.

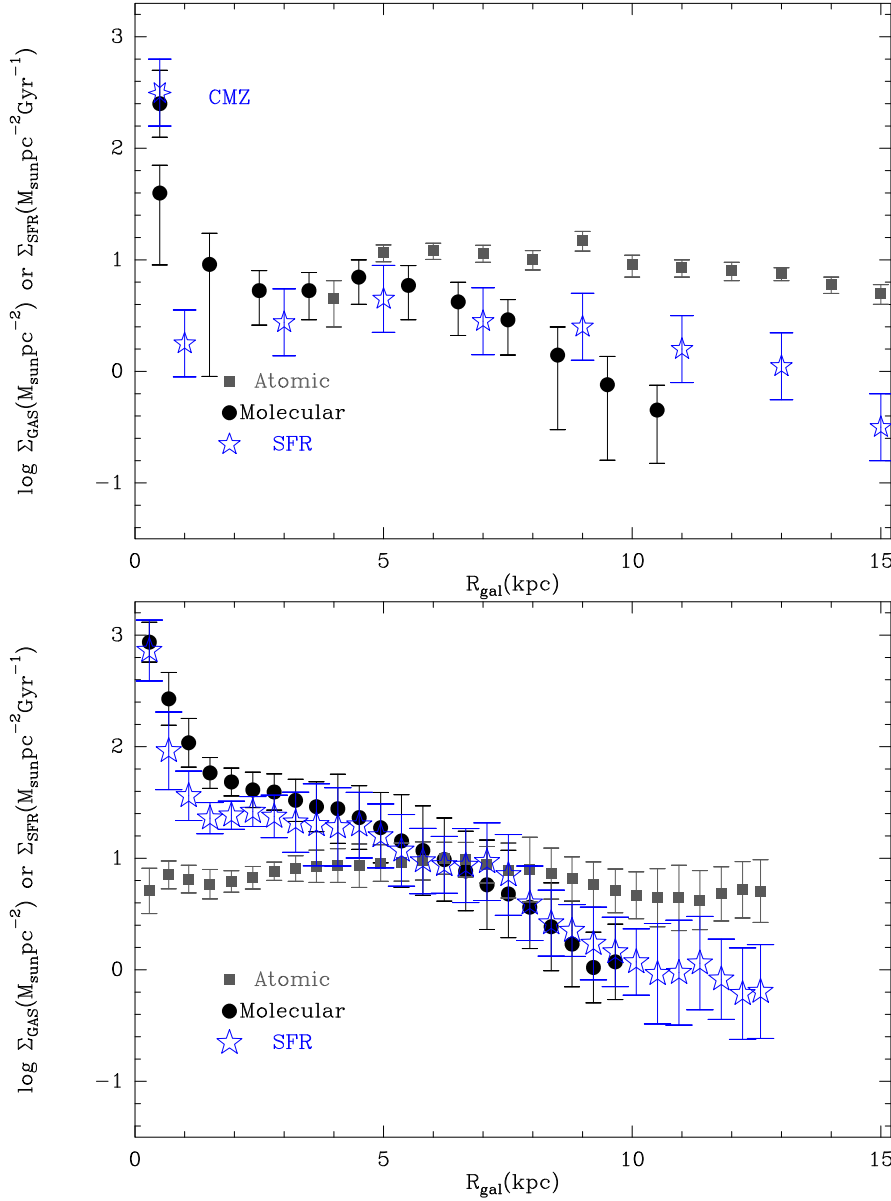


FIG. 7.— Top: The radial distribution of surface densities of atomic gas, molecular gas, and star formation rate for the MW. The atomic data were supplied by P. Kalberla, (Kalberla & Dedes 2008), but we corrected for helium. The discontinuity around 8.5 kpc reflects the inability to model H I near the solar circle. The molecular data are taken from Table 1 in Nakanishi & Sofue (2006), but scaled up to be consistent with the bottom panel, using  $X(\text{CO}) = 2.0 \times 10^{20}$  and multiplying by 1.36 to include helium. The molecular surface density in the innermost bin is highly uncertain and may be overestimated by using a constant value of  $X(\text{CO})$  (§2.4). The  $\Sigma(\text{SFR})$  is read from Figure 8 in Misiriotis et al. (2006), but it traces back, through a complex history, to Guesten & Mezger (1982), based on radio continuum emission from H II regions. That result was in turn scaled to the latest estimate of total star formation rate in the MW of  $1.9 \text{ M}_{\odot} \text{ yr}^{-1}$  (Chomiuk & Povich 2011). Separate points for  $\Sigma_{mol}$  and  $\Sigma(\text{SFR})$  are plotted for the CMZ ( $R_{gal} < 250 \text{ pc}$ ). An uncertainty of 0.3 was assigned arbitrarily to the values of  $\log \Sigma(\text{SFR})$ . Bottom: Same as the top panel, but for NGC 6946. It is based on a figure in Schruba et al. (2011) but modified by A. Schruba to show radius in kpc for ready comparison to the plot for the MW. Reproduced by permission of the AAS. All gas distributions for both galaxies include a correction for helium.

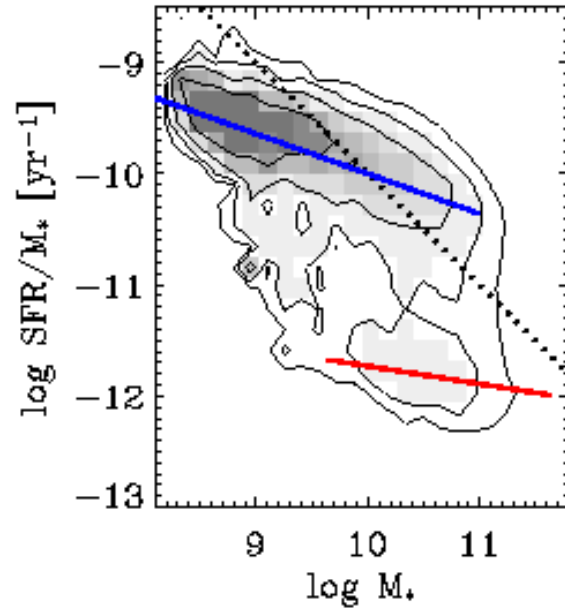


FIG. 8.— Relation between specific star formation rate ( $\dot{M}_*/M_*$ ) and galaxy mass for galaxies in the SDSS spectroscopic sample, and with SFRs measured from GALEX ultraviolet luminosities. Gray contours indicate the (1/Vmax-weighted) number distribution of galaxies in this bivariate plane. The blue solid line shows the fit to the star-forming sequence fit, and the red line shows approximate position of non-star-forming red sequence on this diagram. The dotted line shows the locus of constant  $\text{SFR} = 1 M_\odot \text{yr}^{-1}$ . Figure adapted from Schiminovich et al. (2007). Reproduced by permission of the AAS.



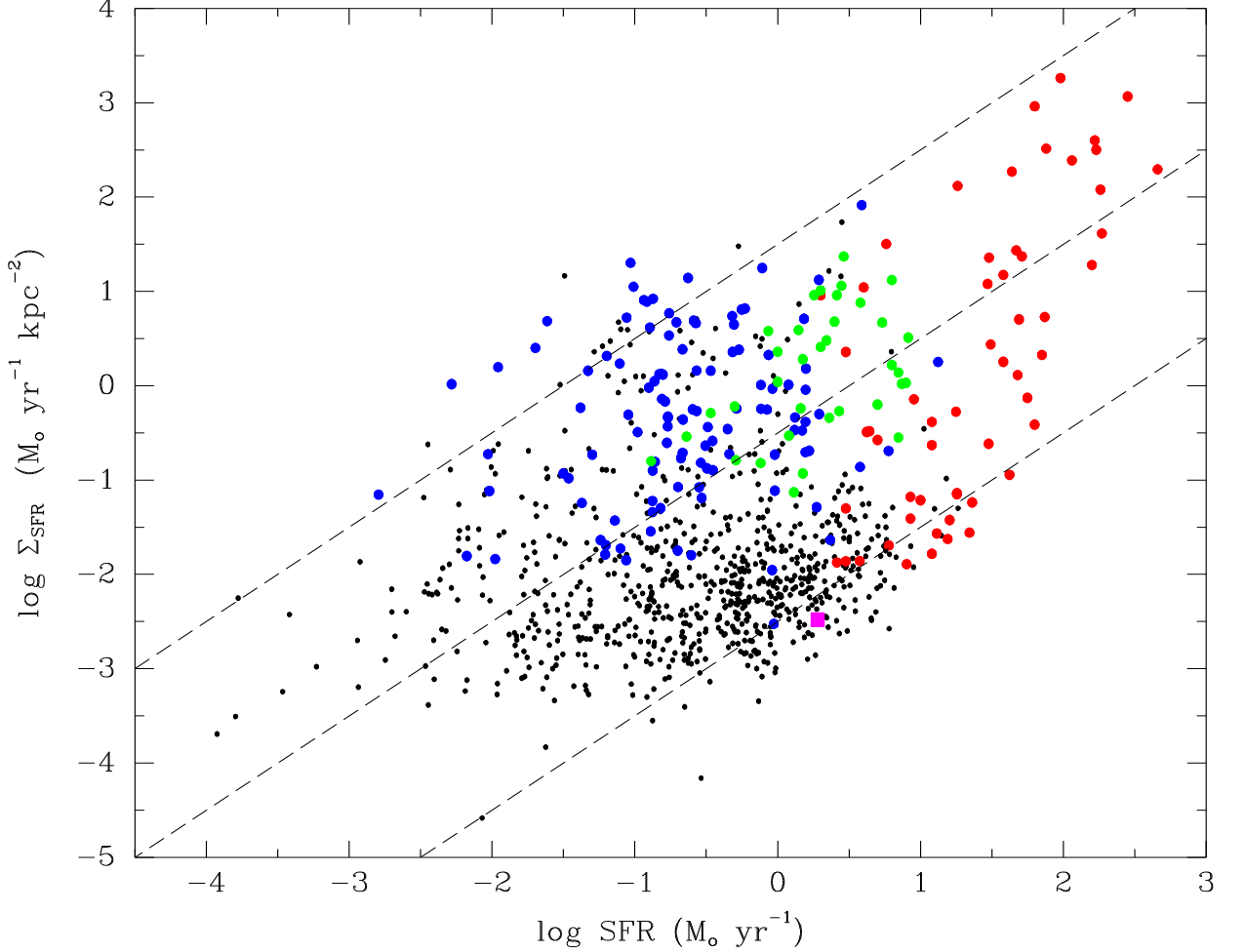


FIG. 9.— Distribution of integrated star formation properties of galaxies in the local Universe. Each point represents an individual galaxy or starburst region, with the average SFR per unit area (SFR intensity) plotted as a function of the absolute SFR. The SFR intensities are averaged over the area of the main star-forming region rather than the photometric area of the disk. Diagonal lines show loci of constant star-formation radii, from 0.1 kpc (top) to 10 kpc (bottom). Several sub-populations of galaxies are shown: normal disk and irregular galaxies measured in  $H\alpha$  and corrected for dust attenuation (solid black points) from the surveys of Gavazzi et al. (2003), James et al. (2004), Hameed & Devereux (2005), and Kennicutt et al. (2008); luminous star-formation dominated infrared galaxies (LIRGs) and ultraluminous infrared galaxies (ULIRGs), plotted as red points, from Dopita et al. (2002) and Scoville et al. (2000); blue compact starburst galaxies measured in  $H\alpha$  (blue points) from Pérez-González et al. (2003) and Gil de Paz et al. (2005); and circumnuclear star-forming rings in local barred galaxies measured in  $Pa\alpha$  (green points) as compiled by Kormendy & Kennicutt (2004). The MW (magenta square) lies near the high end of normal spirals in total star formation rate, but it is near the average in  $\Sigma(\text{SFR})$  (§5.1). The relative numbers of galaxies plotted does not reflect their relative space densities. In particular the brightest starburst galaxies are extremely rare.

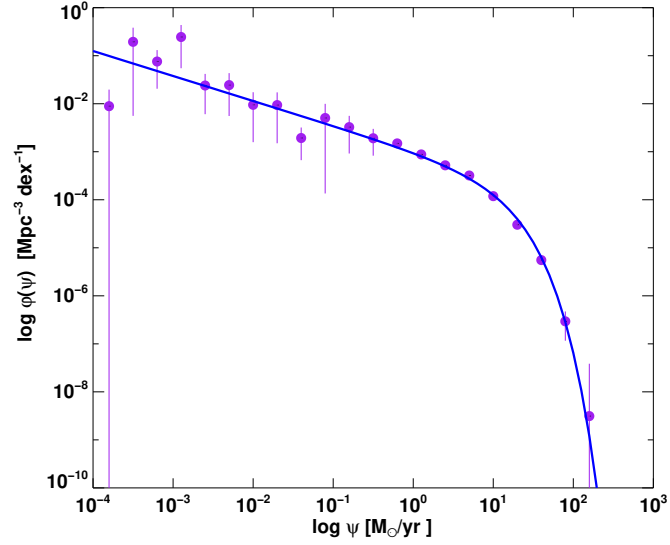


FIG. 10.— Volume-corrected SFR distribution function for disk and irregular galaxies in the local Universe, as derived from a combination of large flux-limited ultraviolet and infrared catalogs and a multi-wavelength survey of the local 11 Mpc volume. Vertical lines indicate uncertainties due to finite sampling; these are especially important for low SFRs, where the statistics are dominated by dwarf galaxies, which can only be observed over small volumes. Statistics on gas-poor (elliptical, dwarf spheroidal) galaxies are not included in this study. The blue line shows a maximum-likelihood Schechter function fit, as described in the text. Figure is original, but similar to one in Bothwell et al. (2011).

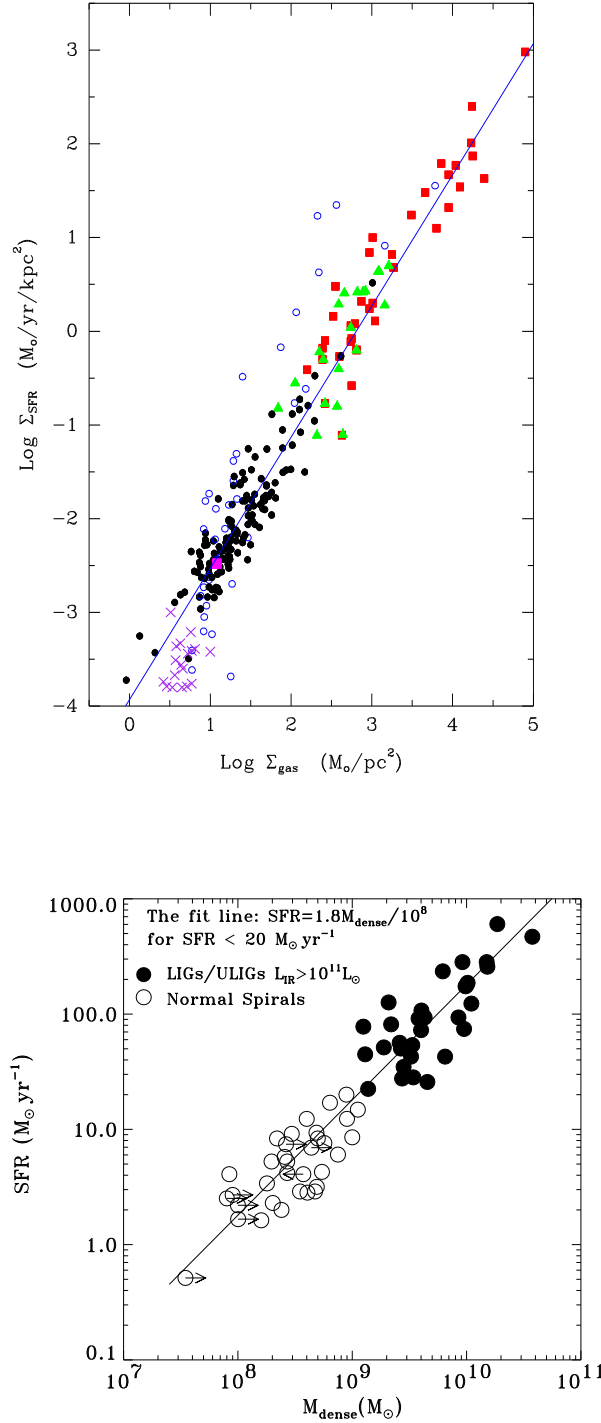


FIG. 11.— Upper: Relationship between the disk-averaged surface densities of star formation and gas (atomic and molecular) for different classes of star-forming galaxies. Each point represents an individual galaxy, with the SFRs and gas masses normalized to the radius of the main star-forming disk. The line shows the original  $N = 1.4$  fit from Kennicutt (1998b) superimposed on the data. Most of the galaxies form a tight relation (exceptions discussed below), and with the improved dataset, even the normal galaxies (shown with black points) follow a well-defined Schmidt law on their own. The dispersion of the normal galaxies overall from the average relation ( $\pm 0.30$  dex rms) is considerably higher than can be attributed to observational uncertainties, which suggests that much of the dispersion is physical. The Milky Way (magenta square) fits well on the main trend seen for other nearby normal galaxies. The purple crosses show data for low surface brightness galaxies. The sample of galaxies has been enlarged from that studied in Kennicutt (1998b), with many improved measurements as described in the text. Lower: Corresponding relation between the total (absolute) SFR and the mass of *dense* molecular gas as traced in HCN. The line is a linear fit, which contrasts with the non-linear fit in the upper panel. Figure adapted from Gao & Solomon (2004). Reproduced by permission of the AAS.

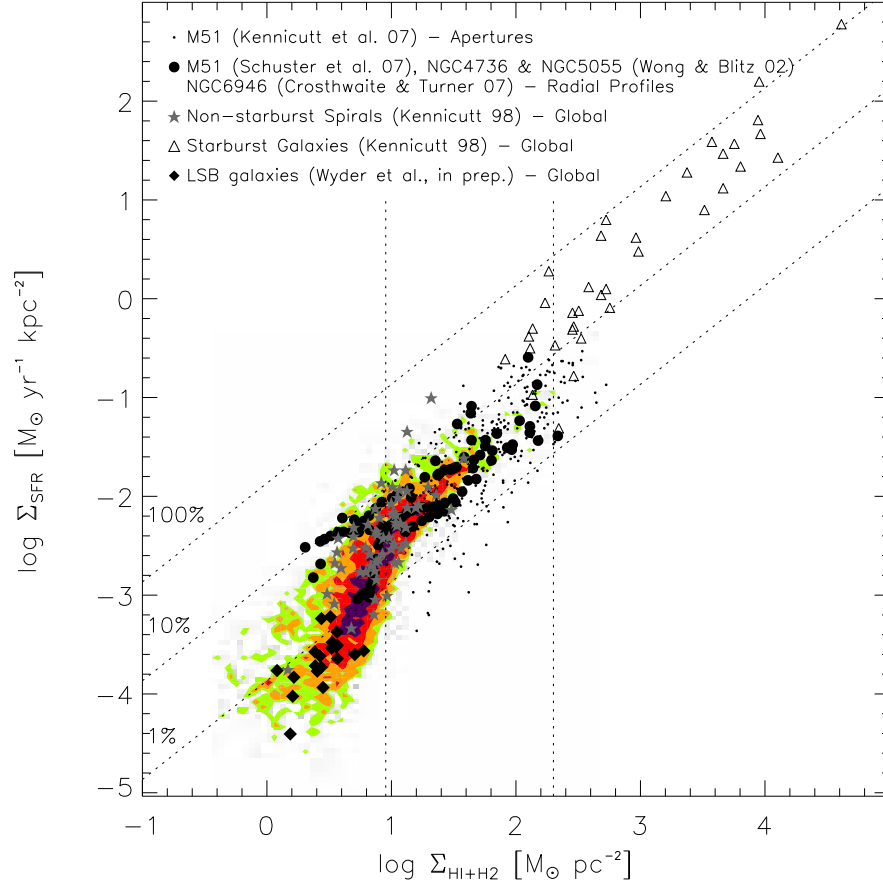


FIG. 12.— Relation between SFR surface densities and total (atomic and molecular) gas surface densities for various sets of measurements, from Bigiel et al. (2008). Colored contours show the distribution of values from measurements of sub-regions of SINGS galaxies. Overplotted as black dots are data from measurements in individual apertures in M51 (Kennicutt et al. 2007). Data from radial profiles from M51 (Schuster et al. 2007), NGC 4736, and NGC 5055 (Wong & Blitz 2002), and NGC 6946 (Crosthwaite & Turner 2007) are shown as black filled circles. The disk-averaged measurements from 61 normal spiral galaxies (filled gray stars) and 36 starburst galaxies (triangles) from Kennicutt (1998b) are also shown. The black filled diamonds show global measurements from 20 low surface brightness galaxies (Wyder et al. 2009). In all cases, calibrations of IMF,  $X(\text{CO})$ , etc. were placed on a common scale. The three lines extending from lower left to upper right show lines of constant global star formation efficiency. The two vertical lines denote regimes which correspond roughly to those discussed in §6 of this review. Figure taken from Bigiel et al. (2008). Reproduced by permission of the AAS.

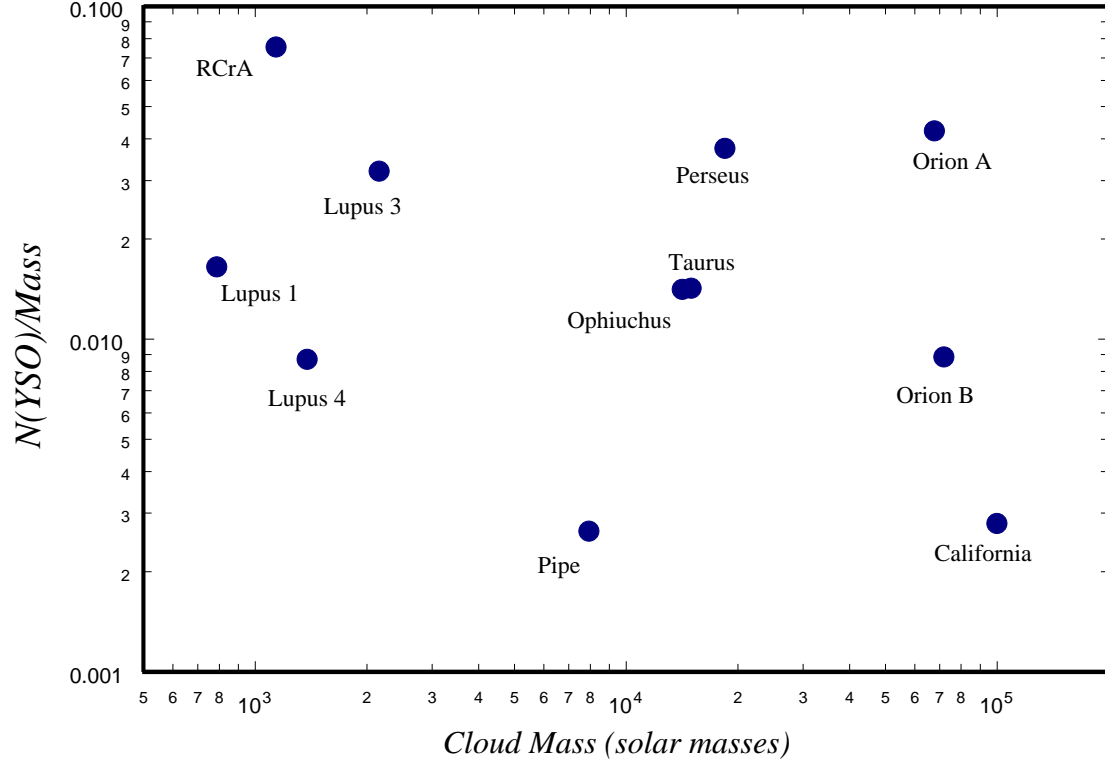


FIG. 13.— Plot of the ratio of the total YSO content of a cloud to the total cloud mass vs. total cloud mass. This is equivalent to a measure of the star formation efficiency as a function of cloud mass for the local sample. It is also equivalent to the measure of the SFR per unit cloud mass as a function of the cloud mass. The plot shows large variations in the efficiency and thus the SFR per unit mass for the local cloud sample. Taken from Lada et al. (2010). Reproduced by permission of the AAS.

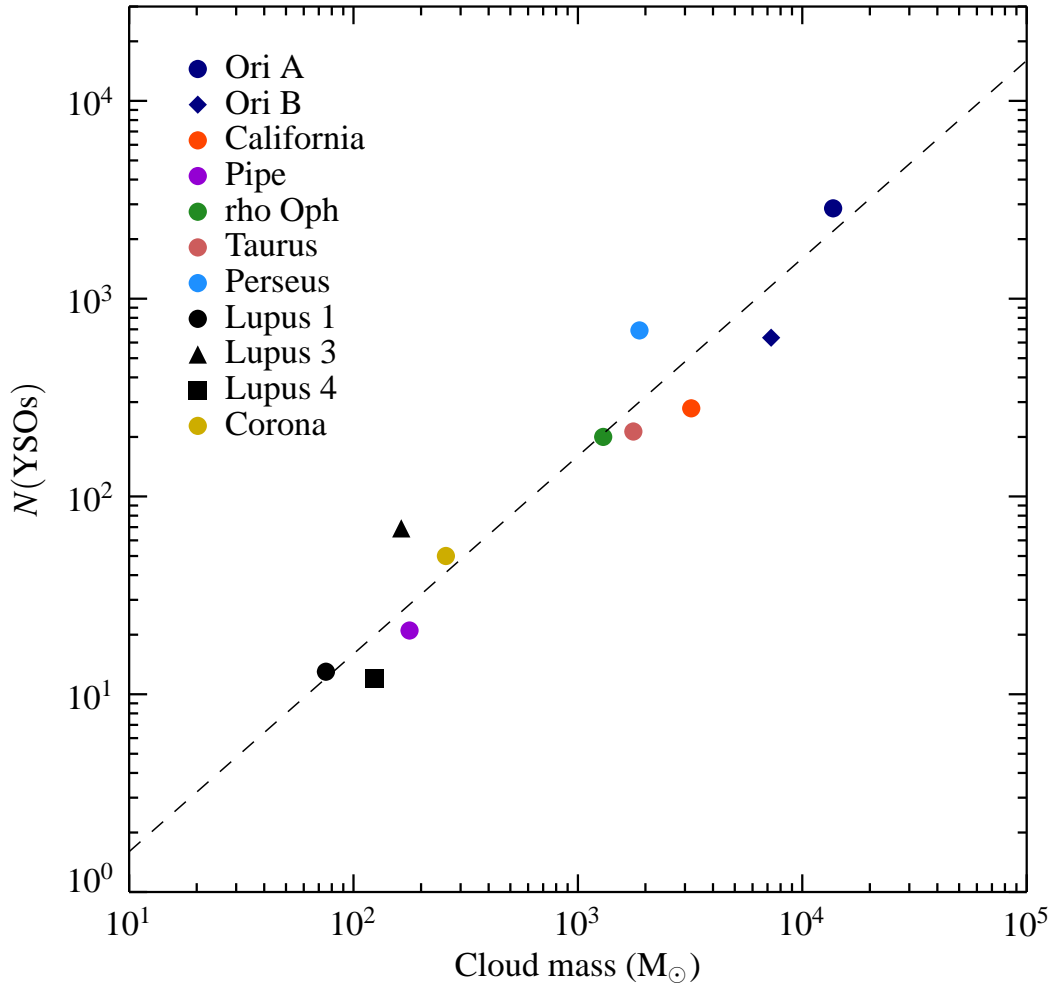


FIG. 14.— Taken from Lada et al. (2010). Relation between  $N(\text{YSOs})$ , the number of YSOs in a cloud, and  $M_{0.8}$ , the integrated cloud mass above the threshold extinction of  $A_{K0} = 0.8$  mag. For these clouds, the SFR is directly proportional to  $N(\text{YSOs})$ , and thus this graph also represents the relation between the SFR and the mass of highly extinguished and dense cloud material. A line representing the best-fit linear relation is also plotted for comparison. There appears to be a strong linear correlation between  $N(\text{YSOs})$  (or SFR) and  $M_{0.8}$ , the cloud mass at high extinction and density. Taken from Lada et al. (2010). Reproduced by permission of the AAS.

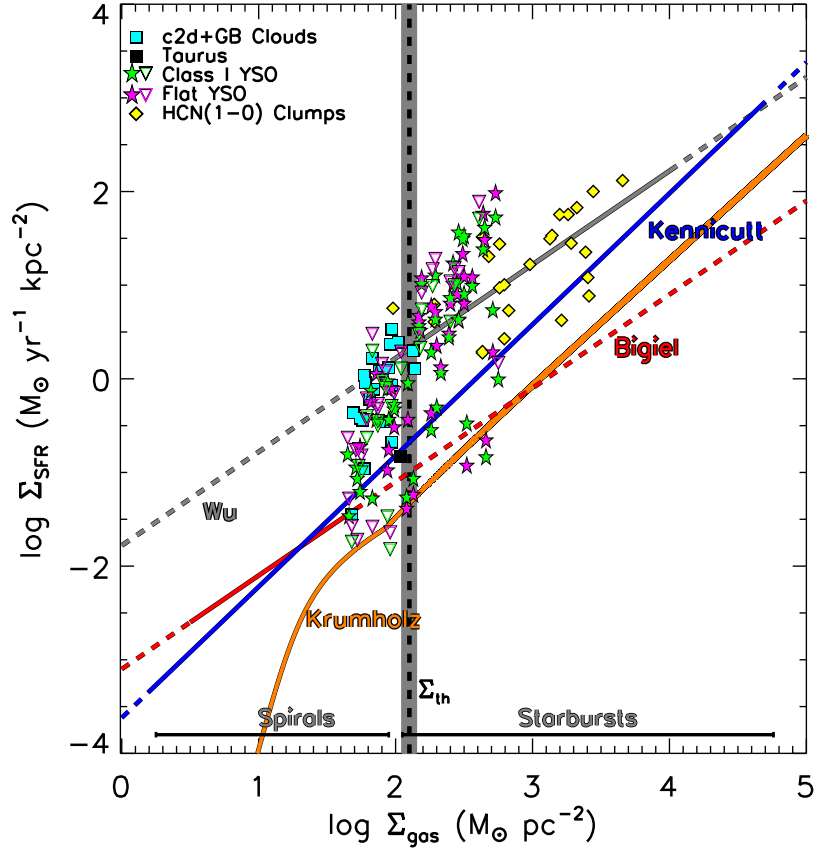


FIG. 15.— Comparison of Galactic total c2d and GB clouds, YSOs, and massive clumps to extragalactic relations. SFR and gas surface densities for the total c2d and GB clouds (cyan squares), c2d Class I and Flat SED YSOs (green and magenta stars), and  $L_{IR} > 10^{4.5} L_{\odot}$  massive clumps (yellow diamonds) are shown. The range of gas surface densities for the spirals and circumnuclear starburst galaxies in the Kennicutt (1998b) sample is denoted by the gray horizontal lines. The gray shaded region denotes the range for  $\Sigma_{th} = 129 \pm 14 M_{\odot} \text{ pc}^{-2}$ . Taken from Heiderman et al. (2010). Reproduced by permission of the AAS.